

**POSSIBLE IONOSPHERIC ELECTRIC CURRENTS  
FOR  
PI2 MICROPULSATIONS**

by

**SABINE CAPPELLE**

B.S., Humboldt State University (California), 1983

**A THESIS SUBMITTED IN PARTIAL FULFILLMENT OF  
THE REQUIREMENTS FOR THE DEGREE OF  
MASTER OF SCIENCE**

in

**THE FACULTY OF GRADUATE STUDIES**

Department of Geophysics and Astronomy

We accept this thesis as conforming  
to the required standard

**THE UNIVERSITY OF BRITISH COLUMBIA**

December 1986

©Sabine Cappelle, 1986

In presenting this thesis in partial fulfilment of the requirements for an advanced degree at the University of British Columbia, I agree that the Library shall make it freely available for reference and study. I further agree that permission for extensive copying of this thesis for scholarly purposes may be granted by the head of my department or by his or her representatives. It is understood that copying or publication of this thesis for financial gain shall not be allowed without my written permission.

Department of Geophysics and Astronomy

The University of British Columbia  
1956 Main Mall  
Vancouver, Canada  
V6T 1Y3

Date 29 January 1987

## Abstact

Two possible ionospheric electric currents for Pi2 micropulsations are investigated and tested against data collected from a meridian chain of stations in Saskatewan.

The electric coupling between the ionosphere and the magnetosphere under disturbed magnetospheric conditions is believed to be the cause of the Pi2 generation and propagation.

The LC circuit analogy is first used to model this interaction, the source of energy lying in the magnetospheric equatorial plane. Secondly, the possibility of an ionospheric electric impulse imparted to a field-aligned current under the conditions of brightening of aurora is considered.

It is found experimentally that the Pi2 originates possibly from these two source regions: the characteristics of a resonant LC oscillation expanding symmetrically to the west and to the east of the magnetospheric potential source are observed, as well a strong toroidal field existing and possibly originating in the ionosphere.

It is suggested that optical data in conjunction with auroral radar echo and satellite data be necessary to confirm a future mathematical development of these possible Pi2 generation and propagation models.

## Table of content

<b>Introduction . . . . .</b>	<b>1</b>
<b>Chapter 1 Basic Physical Principles . . . . .</b>	<b>5</b>
1.1 The ionospheric and field-aligned currents . . . . .	5
1.2 Screening of field-aligned currents by a uniform ionosphere . . . . .	10
1.3 Reflection of an Alfvén wave by a uniform ionosphere . . . . .	11
<b>Chapter 2 Methods of Analysis . . . . .</b>	<b>15</b>
2.1 Detection and recording techniques . . . . .	15
2.2 Selection of events . . . . .	16
2.3 Digital filters . . . . .	21
2.4 Spectral analysis . . . . .	28
2.5 Polarization analysis . . . . .	30
<b>Chapter 3 Possible Models . . . . .</b>	<b>37</b>
3.1 The lumped circuit elements model . . . . .	37
3.2 The hydromagnetic wave or, possibly, the ‘ field-aligned current shear mode’	51
<b>Chapter 4 Experimental Results . . . . .</b>	<b>61</b>
4.1 Pi2 and substorm . . . . .	61
4.2 Pi2 frequency shifts . . . . .	66
4.3 Pi2 polarization results . . . . .	70
<b>Conclusions and further experiments . . . . .</b>	<b>81</b>
<b>Bibliography . . . . .</b>	<b>85</b>
<b>Appendix A Instrumentation and Pre-processing . . . . .</b>	<b>89</b>
<b>Appendix B Digital Filters . . . . .</b>	<b>95</b>

<b>Appendix C</b> Current Loop Model . . . . .	<b>103</b>
<b>Appendix D</b> Summary of the principal Pi2 theories proposed in the litterature	<b>108</b>
<b>Appendix E</b> KP and AE Indices for August 08 1983 . . . . .	<b>109</b>

## **List of Tables**

Table 1. Geographic and geomagnetic coordinates of the stations . . . . .	15
Table 2. Polarization parameters of two-channel synthetic signals . . . . .	35
Table A1. Frequency band of analog instruments . . . . .	89
Table A2. Response characteristics of the analog instruments . . . . .	89

## List of Figures

- Fig. 1. Integrated induction magnetometer data from South End (panel a and b) and La Ronge (panel c and d). H Component. August 08, 1983. . . . . 4
- Fig. 2. Vector distribution ( $2 \text{ A m}^{-1}$  vector scale) of the ionospheric current in latitudes higher than  $50^\circ$  during a typical substorm. ( Kamide, Y. and Matsushita, S.: 1967<sub>b</sub> , *J.Geophys. Res.* **84**, 4099.) . . . . . 8
- Fig. 3. Two possible configurations of field-aligned currents as pointed out by Bostrom (1964).(Bostrom, R.: 1964, *J.Geophys. Res.* **69**, 4983.) . . . . . 8
- Fig. 4. Schematic illustration of the model current system for a typical magnetic substorm. The current distribution is shown only for the northern hemisphere, though it is symmetric with respect to the equator. (Fukushima, 1969.) . . . . . 9
- Fig. 5. Relation between the models of Birkeland-Alfven current-system (A) and Chapman-Vestine current-system (C). The difference between these two current-systems, denoted by (B), produces no magnetic effects on the ground. (Fukushima, 1969.) . . . . . 10
- Fig. 6. Reflection of an Alfven wave by a uniform ionosphere. . Bottom: closure configuration of the induced Hall current. . . . . 14
- Fig. 7. Panel a: Auroral echo of a 50 mHz CW bistatic Doppler radar (operated by I.S.A.S). The scattering area is located over South End. Panel b: Simultaneous induction magnetometer data (H component). Panel c: Pi2 waveform expanded from panel b. South End, August 08, 1983. . . . . 19
- Fig. 8. Panel a: Same as Figure 7<sub>a</sub>. Panel b: Simultaneous induction magnetometer data: Pi2 waveform (H component). South End, August 08 1983. . . . . 20
- Fig. 9. Pi2 events in their respective local time sector. . . . . 22
- Fig. 10. Maximum Entropy spectral density. La Ronge, H component, 7.30'-8.00 U.T, August 08, 1983. . . . . 23
- Fig. 11. Panel a: Weighting polarization filter. Panel b: Integrator (time integration constant of ten minutes). Panel c: 500-points smoothing Hanning window. La Ronge, H component, August 08, 1983. . . . . 26
- Fig. 12. Left: Particule motion of two-channel white noise. Right: 100 % polarized pair of sinusoids phase shifted by  $\pi/4$ . . . . . 27
- Fig. 13. Right: Trace of the spectral matrix. Left: Associated % polarization. La Ronge, H and D component, 7.15'-7.28' U.T, August 08, 1983. . . . . 27
- Fig. 14. Spectral estimates of the Pi2 event illustrated in Figure 1<sub>d</sub>. Panel a: Smoothed power spectra. Panel b:Maximum Entropy Method. Panel c: Raw power spectra (periodogram).La Ronge, H component, 7.20'-7.28' U.T, August 08, 1983. . . . . 29

Fig. 15. Elliptically polarized wave. The vibrational ellipse for the magnetic vector. . . . .	31
Fig. 16. Smoothed power spectra of the two-channel synthetic data. . . . .	35
Fig. 17. Two-channel synthetic data phase shifted by $\frac{3\pi}{4}$ (panel a), $\frac{5\pi}{4}$ (panel b), $\frac{7\pi}{4}$ (panel c). . . . .	36
Fig. 18. Top: snapshot representation of a symmetrically growing magnetospheric potential source lying in the equatorial plane. Bottom: equivalent single loop. . . . .	40
Fig. 19. The fac diverge in the ionosphere as Pedersen currents. The associated Hall current closes in the ionosphere. . . . .	43
Fig. 20. Longitudinal expansion of the induced AC Hall currents. . . . .	44
Fig. 21. Horizontal vector field generated by a current loop of radius 50 km, lying at ionospheric height (110 km), and carrying a current of $3 \times 10^5 A$ (ccw). . . . .	45
Fig. 22. Amplitude of the vector field shown in Figure 21. Distance increases radially outward from the orthogonal projection of the center of the loop on the ground (assuming a flat earth) . . . . .	45
Fig. 23. Amplitude of the phase shifted currents flowing through the loops. . . . .	50
Fig. 24. The Hall current network expands like a longitudinal travelling wave: $I(y, t) = I_m \sin(ky - \omega t)$ , the magnetic effects of which we need to integrate over the longitude $y$ . . . . .	50
Fig. 25. Horizontal ground magnetic vector: $B_H(n\Delta t) = \sum_{j=1}^n B_{Hm} \sin(k(n - j)\Delta y - \omega n\Delta t)\Delta_j$ . Each vector is plotted in the H-D plane at a time interval of 4 sec. The two stations are located 100 km north and south of the source region (S). The wave expands westward: $v=4$ km/sec, $f=16.7$ mHz, $H=0$ at the latitude of the source. . . . .	51
Fig. 26. Waveforms from magnetic vectors shown in Figure 25. Left: H component. Right: D component. . . . .	51
Fig. 27. Top: Polarization patterns predicted for stations located symmetrically around the source region (S). The arrow indicates the direction of expansion (westward in this case), $v=4$ km/sec, $f=16.7$ mHz. Bottom: same as top but the expansion is eastward. . . . .	52
Fig. 28. Same as Figure 27 but the speed is increased to 8 km/sec. . . . .	53
Fig. 29. Development of the aurora during the expansion phase. The midnight meridian is toward the bottom center of each panel (Akasofu, 1975). . . . .	58
Fig. 30. What is believed to be the initial ionospheric electric impulse imparted to a field-aligned current under the conditions of brightening of aurora. Travelling	



surge speed is 2 km/sec. The Hall current is the magnetic field observed on the ground. . . . .	59
Fig. 31. Resulting polarization patterns produced by the Hall current shown in Figure 30. . . . .	60
Fig. 32. Magnetograms from South End (SE), La Ronge (LR), Christopher Lake (CL) and Park Site (PS). Integrated from induction magnetometer with a three hour time integration time constant. August 08 1983. . . . .	64
Fig. 33. Latitude profile of H-D-Z displayed in Figure 32. August 08 1983. . . . .	65
Fig. 34. The electrojet normalized power compared to the Pi2 normalized power as a function of latitude. South End (SE), La Ronge (LR), Christopher Lake (CL), Park Site (PS). August 08 1983. . . . .	67
Fig. 35. Spectral content of Pi2 versus latitude: the dominant frequency and a possible higher frequency harmonic. South end (SE), La Ronge (LR), Christopher Lake (CL), Park Site (PS). August 08 1983. . . . .	70
Fig. 36. The dominant period of Pi2 events, obtained by visual inspection, as a function of $K_p$ . (Rostoker,G., 1967). . . . .	71
Fig. 37. Polarization characteristics of Pi2 averaged over the time interval. . . . .	76
Fig. 38. Same as Figure 37. . . . .	77
Fig. 39. Summary of polarization results. . . . .	78
Fig. 40. Same as Figure 37. . . . .	79
Fig. 41. Top: same sa Figure 37. Bottom: Dynamic polarization pattern in the time domain.La Ronge; left: 7.21'- 7.24' U.T; right: 7.24'-7.28' U.T; August 08 1983. . . . .	80
Fig. A1. Block diagram of analog-to-digital conversion system. . . . .	91
Fig. A2. Block diagram of digital pre-processing. . . . .	92
Fig. B1. Block diagram of a simple polarization filter. . . . .	99
Fig. B2. Integrator circuit. . . . .	102
Fig. C1. Ionospheric current loop. . . . .	103

## Acknowledgements

I would like to express my thanks to all those who have helped me in the completion of this work. Primary among these people is my supervisor T. Watanabe whose suggestions and invaluable optimism guided me through this research.

My next tribute goes to the people of the University of Saskatoon, University of Western Ontario and University of British Columbia who contributed to the success of the 1983 campaign.

I am also indebted to Professor Sofko of the University of Saskatoon for providing information on the auroral radar operations and for spending many hours discussing the topic in question.

Finally I am grateful to Ken Whittall and all the fellow graduate students who helped me to deal with the modern computer technology.

Financial support was provided by NSERC operating grant A-3564.

## Introduction

Pulsations in the earth's magnetic field have been observed for over a century since Stewart in 1861 noted the presence of a disturbing force 'of a throbbing or pulsatory' character while studying a great magnetic storm recorded at Kew observatory in England (Stewart, 1861). There was a period of intensive study of micropulsations in the 1960's marked by numerous observational and theoretical investigations. In the last decades, the major advances in the field are due to the study of spacecraft magnetometer data and to the development of digital recording and processing techniques.

Geomagnetic micropulsations are observed on the ground as transitory, short period fluctuations of the earth's magnetic field (usually on the order of seconds or minutes). Their amplitudes vary from fractions of nT to several 100 nT, which is usually less than one part in  $10^3$  of the earth's main field. In the magnetosphere, they propagate as hydromagnetic waves. Like magnetic substorms, these disturbances are of solar origin: the solar-terrestrial interaction involves the transfer of energy from the particle and field environment of the interplanetary medium to the particle and field environment of the earth (magnetosphere); under appropriate conditions, the energy supplied to the magnetosphere is released through steady-state processes by gigantic current systems, or explosively through unstable processes when the amount of energy received is excessive. Micropulsations and magnetic substorms return the balance of energy to the external environment.

When studying micropulsations, two points of view have to be considered: the theory and the observations, the theory being confirmed by observational facts. The major theoretical breakthrough came in 1954 with Dungey. He treated the magnetosphere as a hydromagnetic medium of infinite conductivity permeated by a non-uniform (dipolar)

magnetic field  $\underline{B}_o$ . Dungey assumed that if such a field configuration was perturbed, the perturbation magnetic field would be small ( $\underline{b} \ll \underline{B}_o$ ) so the governing equations for the system could be linearized ( $\underline{b} + \underline{B}_o \sim \underline{B}_o$ ). Dungey's treatment of linearized hydro-magnetic equations led to fundamental predictions of the characters of micropulsations. His work has proved to be the departure point for most of the ensuing studies.

Micropulsations observed on the ground show different morphological characteristics. In order to study these disturbances in a systematic way, a classification system was established in 1957 by the International Association of Geomagnetism and Aeronomy (IAGA). The micropulsations were divided in two main groups: the Pc group (continuous pulsations) and the Pi group (irregular pulsations). These two types were further subclassified according to their period range. Detailed information about this classification system can be found in Jacobs (1970). Let us note however that there is only a morphological significance to the dividing line between the types of pulsations, and there is no reason to believe that there might not be more than one generation mechanism for a given micropulsation. The category does not specify the generation mechanism simply because the morphology is not based on physics.

The Pi2 belongs to the irregular group. It is an impulsive wavetrain lasting  $\sim 8$  to 15 minutes; its period ranges from  $\sim 40$  sec to 140 sec and its amplitude from  $\sim 0.5$  nT in low latitude regions to over 100 nT in the substorm disturbed regions; its association with the development of a magnetic substorm is its main characteristic (see Figure 1). As one would expect for a substorm related phenomenon, Pi2 are observed primarily on the night side of the earth. On the magnetogram, the substorm is identified by a sudden deviation (often called a 'bay') from the normal baseline in all three components of the magnetic field. Many people have proposed that Pi2 starts at the onset of the expansion phase of the substorms (Troitskaya and Gul'elmi, 1967; Afanasyeva *et al.*,

1970; Pytte and Treffal, 1972; Pytte *et al.*, 1976; and many others). However 'the onset time' is still to our knowledge determined subjectively by the observer, and therefore it seems more reasonable to say that Pi2 is associated with the early stages of the bay as shown in Figure 1.

The generation theories of Pi2 are numerous and often very complex. They can be categorized into transient response mechanisms and instability mechanisms. A summary of the principal theories is given in Appendix D along with relevant references. In the present work, two preliminary models of simplified transient response mechanisms are presented and tested against data, collected from a latitudinal chain of stations between 66.3° and 61.5° (geomagnetic coordinates). If the Pi2 is the carrier of information between the magnetosphere and the ionosphere during a substorm event, then it is clear that an understanding of the mechanism(s) involved in the generation of Pi2's will lead to an understanding of the mechanism(s) involved in auroral break-up and substorm development in general. The methods of analysis are presented in Chapter 2, the models in Chapter 3, the experimental results in Chapter 4 followed by a discussion and suggestions for further work.

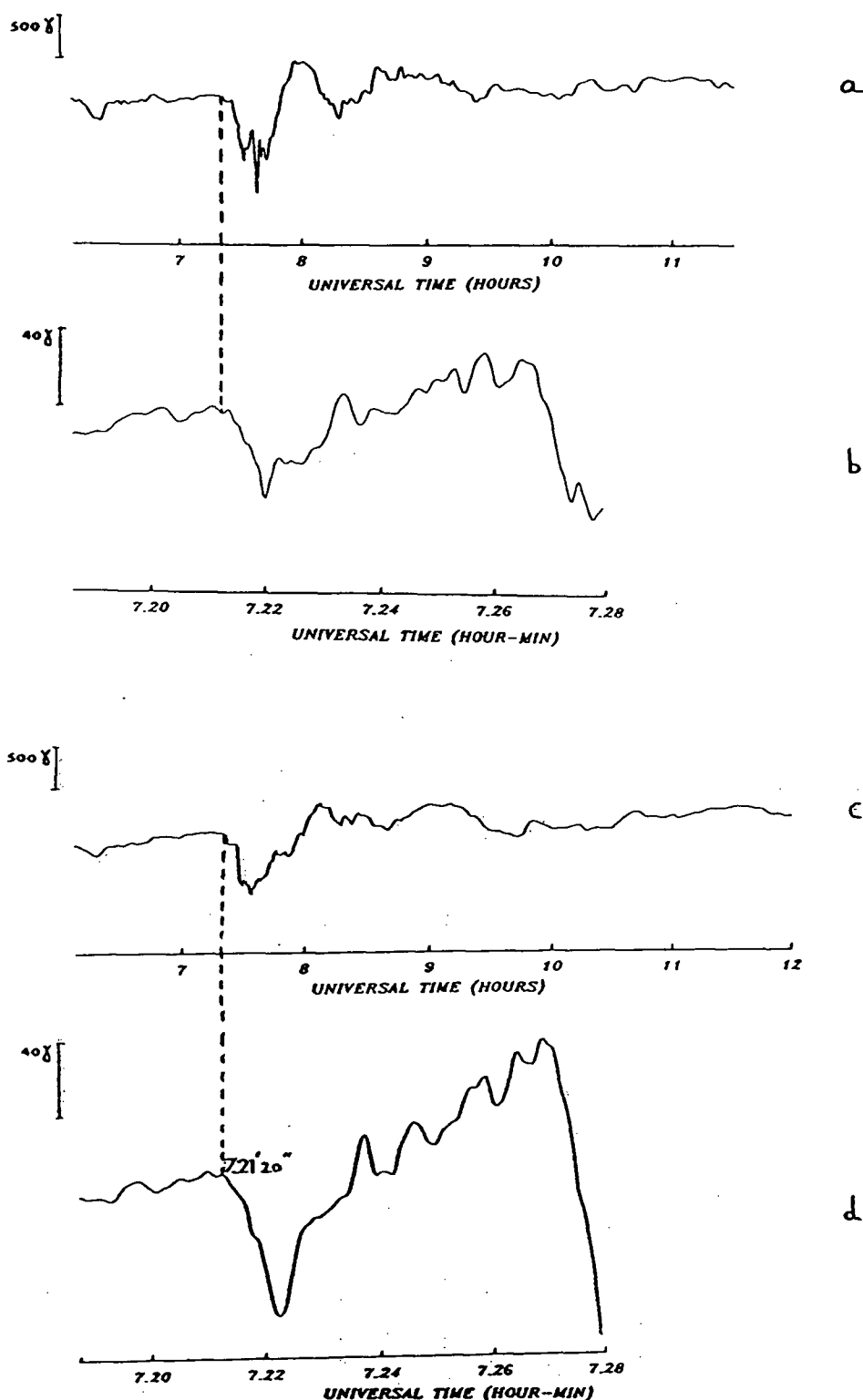


**Figure 1.** Integrated induction magnetometer data from South End (panel a and b) and La Ronge (panel c and d). Panel a and c: the magnetic substorm (three-hour time integration constant). Panel b and d: the associated Pi2 (ten-minute time integration constant). H component. August 08, 1983.

## Chapter 1

In this chapter, we will examine two physical processes related to the Pi2 generation and propagation: one which involves field-aligned currents (FAC), the other which involves the reflection of Alfvén waves by a uniform ionosphere.

### 1.1 The ionospheric and field-aligned currents

It is important, first of all, to realize that the magnetic perturbations observed on the earth's surface arise from ionospheric and possibly magnetospheric currents as well as induced earth currents. The separation of the magnetic field of these different current sources cannot be made properly from ground magnetic measurements alone. In the last decades, with the advent of new techniques, polar-orbiting ISIS, DMSP, TRIAD and S3-2 satellites provide us with plentiful information on characteristics of field-aligned currents and their relationship to both auroral intensity and auroral electrojet flow. Incoherent scatter radars at auroral latitudes can also determine simultaneously most of the electromagnetic properties in the ionosphere including the electric fields, conductivities, currents, neutral winds and Joule heat dissipation (see Banks and Doupnik, 1975). Recently, efforts to improve the ground-based magnetometer network by operating several meridian chains have made it possible to determine the auroral electrojet locations with an accuracy of  $1^\circ$  in latitude (see Akasofu et al., 1980). By combining these new observations, we are just beginning to construct the 'real' 3-D current model that can account for the complexity in behaviour of the magnetic perturbations during substorm disturbed times.

In the ground magnetic record, the vertical component of the magnetic field is the most affected by the earth's induced currents; therefore, in this study, we will restrict

ourselves to the analysis of the horizontal components H and D only.

A substorm event is most typically seen in the magnetic record by the occurrence of a sharp 'negative bay' in the auroral zone near local midnight (see Figure 1). The auroral zone is originally defined as a region of high occurrence frequency of aurora centered around  $67^\circ$ . The dominant feature in the ionosphere at this time is the westward auroral electrojet.

Figure 2 shows the distribution of the ionospheric current vectors during a typical magnetic substorm. One can observe two basic auroral electrojets: eastward and westward. The eastward electrojet flows in the equatorward half of the evening auroral belt, while the westward electrojet flows in wider regions in the evening and morning sectors. These electrojets are closed primarily in the magnetosphere by the FAC and secondly, in the ionosphere, by return currents in the polar cap and mid-latitudes.

As pointed out by Bostrom (1964), there are basically two possible closure configurations of the electrojets, type 1 and type 2 as schematically illustrated in Figure 3.

Type 1 was originally proposed by Birkeland (1908) and includes an inflow of currents in the morning half of the auroral oval and an outflow from the evening sector. These FAC drive the westward electrojet in the morning sector. In the evening sector the weaker eastward electrojet is connected to its magnetospheric counterpart: the partial ring current. In type 2 current system, an east-west electrojet is generated between FAC sheets aligned in the east-west direction (Watanabe, 1961). Zmuda and Armstrong (1974b) considered two pairs of such FAC, one in the morning sector and the other (with the reversed current direction) in the evening sector. According to their model, the FAC are closed via north-south Pedersen currents in the morning sector (south-north in the



evening sector). The associated east-west electrojet in the morning sector (west-east in the evening sector) is the Hall current and closes in the ionosphere.

A summary of the current configuration is given in Figure 4. The important feature is that each primary current system closed in the magnetosphere is subject to another secondary current system closed in the ionosphere: the Hall current.

Although more complicated models have been presented since 1974, this simple model was selected as a good starting point to understand the basic features of the ionospheric currents and FAC.

Nothing has been said about the main dynamo process which drives the 3-D current system. The generator is switched on in the magnetosphere and has its origin in the solar wind. The mechanisms involved are not fully understood at the present.

Before closing this section, there is one important question to ask: is it possible to differentiate between the 3-D primary current system and the secondary Hall current in the ground magnetic record?

Naoshi Fukushima (1969) gave a very elegant answer to that problem and I want to devote my next section to his explanation.

# IONOSPHERIC CURRENT VECTORS

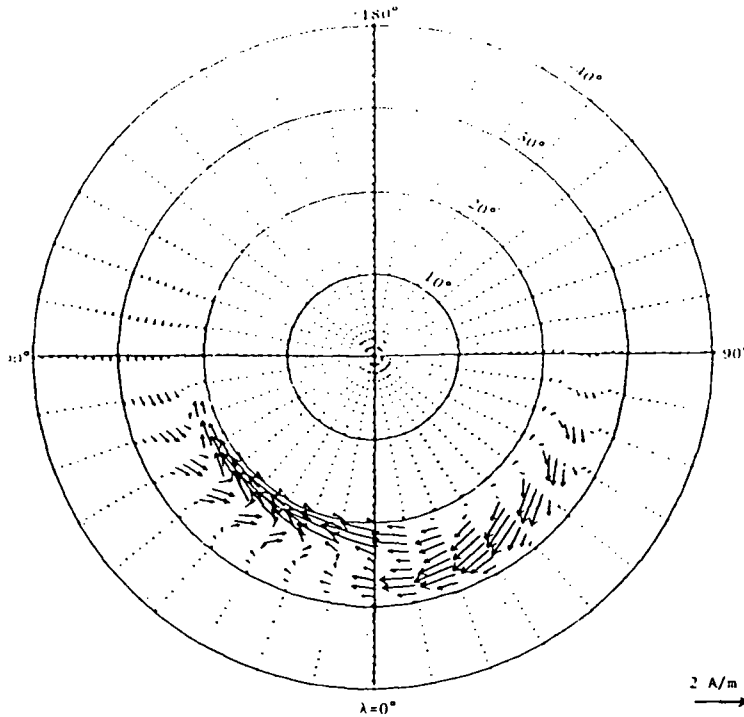
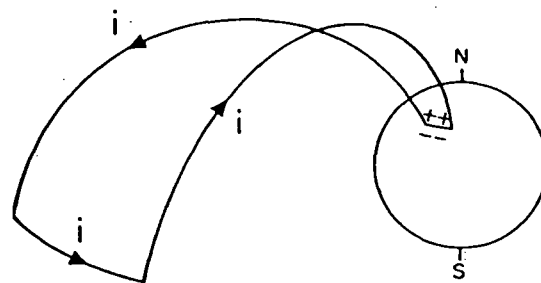
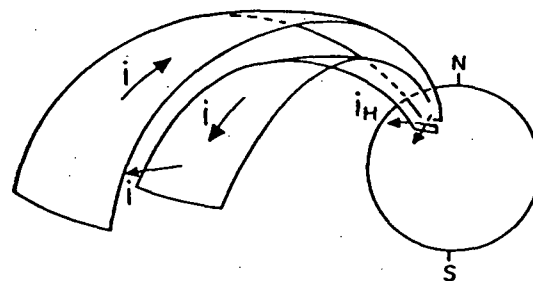


**Figure 2.** Vector distribution ( $2 \text{ A m}^{-1}$  vector scale) of the ionospheric current in latitudes higher than  $50^\circ$  during a typical substorm. (Kamide, Y. and Matsushita, S.: 1967<sub>b</sub>, *J. Geophys. Res.* **84**, 4099.)



TYPE I



TYPE II

**Figure 3.** Two possible configurations of field-aligned currents out of Bostrom (1964). (Bostrom, R.: 1964, *J. Geophys. Res.* **69**, 4983.)

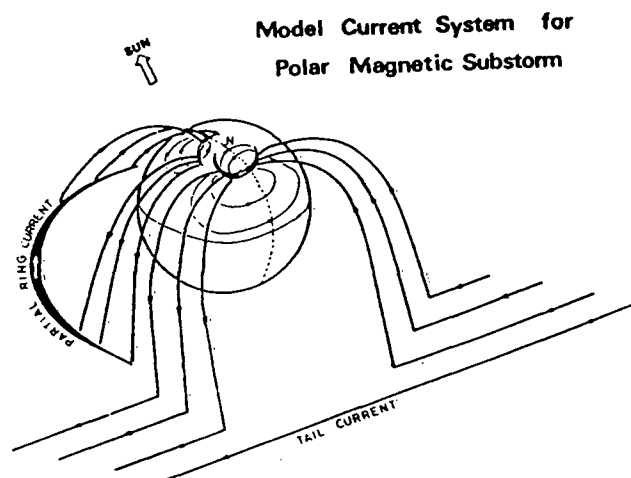


**Figure 4.** Schematic illustration of the model current system for a typical magnetic substorm. The current distribution is shown only for the northern hemisphere, though it is symmetric with respect to the equator. (Fukushima, 1969. )

## 1.2 Screening of field-aligned currents by a uniform ionosphere

Fukushima's theorem can be summarized as follows: Assuming that the magnetic perturbations at a point on the earth's surface are due entirely to the overhead current system, assuming secondly that the ionosphere is an infinitely thin sheet of uniform conductivity lying over a flat earth, then the magnetic effects of **FAC** are precisely cancelled by the magnetic effects of the Pedersen currents; the associated Hall current is therefore the only field seen on the ground.

In Figure 5, current A represents the 3-D system of the Birkeland current model. Current C represents the closed ionospheric Hall-current. The difference between A and C represents the combined effects of **FAC** and Pedersen currents which cancel each other. Since B is not seen on the ground (it is only seen above the ionosphere), A and C generate the same magnetic fields.

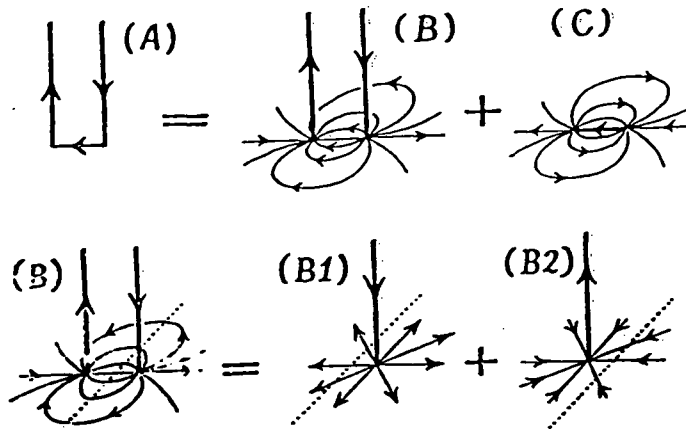


Figure 5. Relation between the models of Birkeland-Alfvén current-system (A) and Chapman-Vestine current-system (C). The difference between these two current-systems, denoted by (B), produces no magnetic effects on the ground. (Fukushima, 1969.)

This analysis gives us two results: the FAC are screened by the ionosphere, and the magnetic field on the ground is rotated through  $90^\circ$  relative to that in the ionosphere. This has been the subject of a paper by Jacobs and Watanabe (1964) and Hugues and Southwood (1976a,b).

This theorem is valid, only if we assume a uniformly conducting ionosphere. Of course, in the environment of an ionospheric electrojet, the ionospheric conductivity is not uniform and hence, one would not expect screening to be perfect. The non-screened component appears, however, as a second order effect. We feel that it is important to analyze the problem to its first order effect before looking at more complex, non-linear situations.

### 1.3 Reflection of an Alfven wave by a uniform ionosphere

It is now widely accepted that micropulsations are the magnetic signature of hydro-magnetic waves occurring in the magnetosphere. In cold plasma theory, two modes of MHD waves are possible, the Alfven mode and the fast mode; the former is a transverse mode which is guided along the ambient magnetic field, the latter propagates isotropically and, generally, there is some compression of the background magnetic field. In a dipole field, the Alfven mode and the fast mode are often coupled together: The Alfven mode transports its energy along the background magnetic field and the wave energy can, therefore, become trapped within a resonant cavity between conjugate ionospheres (see eg. Dungey, 1967; Southwood, 1975). The Alfven mode has received most of the attention in the theoretical literature of micropulsations.

The ionosphere can act in two different ways to an incoming Alfven wave:

1. It will either duct the micropulsation if the wavelength is on the order of the ionospheric duct ( $\sim 10^5$  m) or less. The ionospheric duct is defined by the altitude range

between maxima in Alfvén velocities ( $\sim 100$  km and  $\sim 2000$  km). This applies mainly to the Pc1 range signal.

2. It will reflect the micropulsation partially if the wavelengths are larger (Hugues, 1974<sub>a</sub>, Ellis and Southwood, 1983 ). This applies to the Pi2 which has a wavelength on the order of  $10^7$  m.

Let us consider an incoming transverse wave propagating in the  $Z$  direction. The ionosphere can be regarded as a thin conducting sheet since the vertical wavelengths are large. The wave carries a magnetic field  $\underline{b}$  and an electric field  $\underline{E}$ . The three components  $\underline{b}$ ,  $\underline{E}$ , and the ambient magnetic field  $\underline{B}_0$ , are orthogonal to each other. Figure 6 gives a schematic representation of the reflection process:

1. The electric and magnetic fields of the incident wave have the following relation:

$$b = \frac{1}{v_a} E \quad (1.1)$$

where  $v_a$  is the Alfvén velocity.

An incident wave of amplitude  $E$  gives rise to a reflected wave of amplitude  $E_1$ . Upon reflection, there is  $180^\circ$  phase shift in the electric field so that:

$$E_1 = -RE \quad (1.2)$$

where  $R$  is the reflection coefficient. For a uniform auroral ionosphere,  $R$  has typical value of 0.8-0.9 at high latitudes (Scholer, 1970); therefore, most of the energy is reflected back to the magnetosphere.

2. Pedersen currents,  $\underline{J}_P$ , flow in the ionosphere:

$$\underline{J}_P = \sigma_P(\underline{E} + \underline{E}_1) \quad (1.3)$$

where  $\sigma_P$  is the Pedersen conductivity.

3. The Hall conductivity ( $\sigma_H$ ) is several times larger than the Pedersen conductivity in the auroral ionosphere (  $\frac{\sigma_H}{\sigma_P} \sim 3 - 5$  are typical values ), and induced Hall currents,  $\underline{J}_H$ , also flow:

$$\underline{J}_H = \frac{\sigma_H}{B_o} \underline{B}_o \times (\underline{E} + \underline{E}_1) \quad (1.4)$$

Because  $\underline{B}_o \times (\underline{E} + \underline{E}_1)$  is perpendicular to the wave propagation vector  $\hat{k}$ , if  $\sigma_H$  is horizontally uniform, the ionospheric Hall current divergence is zero, and is closed by return currents, forming two ionospheric vortices as shown schematically in Figure 6 (bottom). This pattern of current flow was proposed by Kato and Watanabe, 1958.

This analysis gives us two interesting results: the magnetic fields of transverse waves must be seen rotated though  $90^\circ$  when observed on the earth, the rotation being caused by currents flowing in the ionosphere, and secondly, in the case of a uniform ionosphere, 80 to 90 % of the energy is reflected back to the magnetosphere.

Multiple reflections from ionospheres in opposites hemispheres give rise to standing Alfvén waves. Ionospheric reflection is however not perfect; and we expect the wave to be damped; the loss of energy is due to Joule dissipation in the ionosphere, associated with the Pedersen currents.

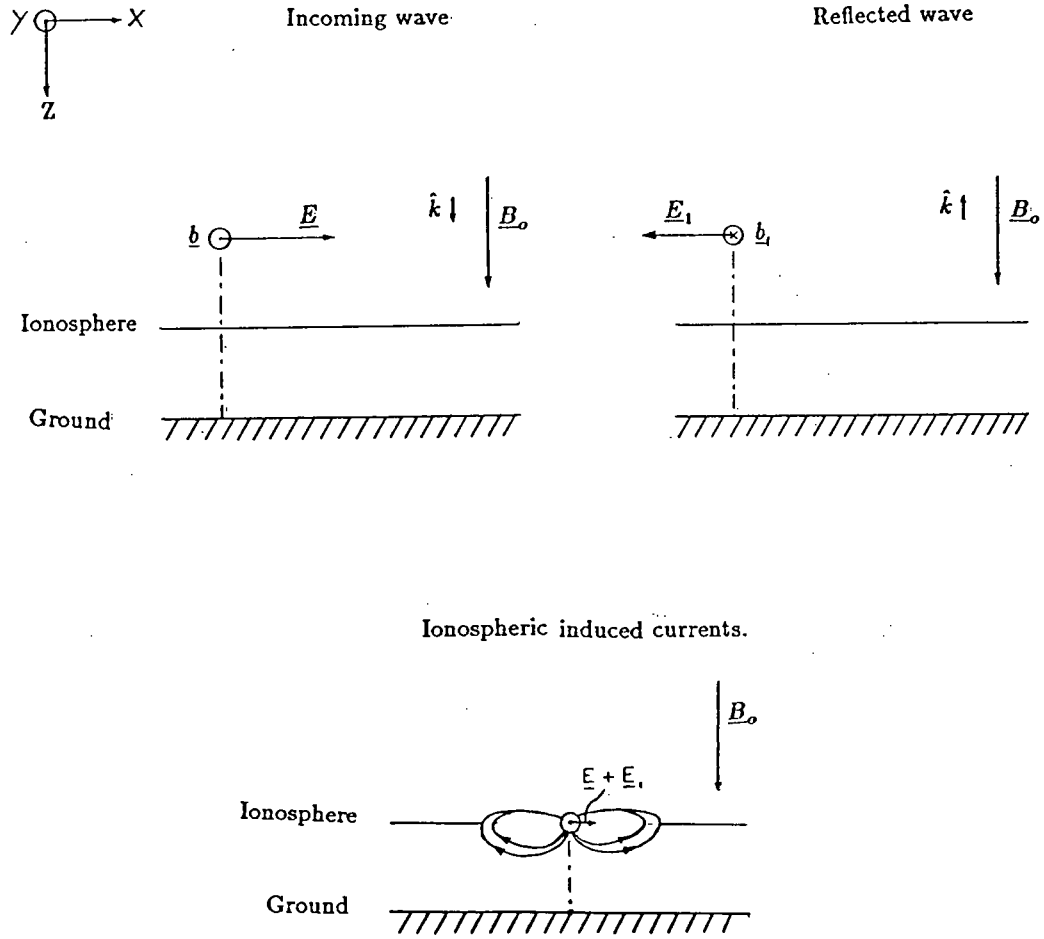


**Figure 6.** Reflection of an Alfvén wave by a uniform ionosphere. Top: the energy is transported along  $\hat{k}$ .  $\underline{B}_0$ ,  $\underline{E}$  and  $\underline{b}$  are orthogonal to each other. Upon reflection, the polarity of  $\underline{b}$  and  $\underline{E}$  are reversed;  $\underline{E}_1 = -R\underline{E}$  ( $R=0.8$ ). Bottom: closure configuration of the induced Hall current,  $\underline{J}_H = \frac{\sigma_H}{B_0} \underline{B}_0 \times (\underline{E} + \underline{E}_1)$ .



## Chapter 2

In this chapter, we will discuss the collection and processing of the micropulsation data: the field recording techniques, the selection of events, the digital filters and spectral analysis techniques used.

### 2.1 Detection and recording techniques

The micropulsation data analyzed in this thesis were collected during the summer of 1983 along a meridian chain of stations in Saskatchewan. See Table 1 for the coordinates of the stations.

	Geographic		Geomagnetic	
	Lat.(N)	Long.(W)	Lat.(N)	Long.(E)
Southend (SE)	56.3°	103.5°	66.3°	312.8°
La Ronge (LR)	55.2°	105.3°	64.8°	311.0°
Christopher Lake (CL)	53.5°	105.8°	63.0°	310.8°
Park Site (PS)	52.2°	107.2°	61.5°	309.8°

Table 1.

The 1983 campaign was organized by J.A Koehler of the Institute of Space and Atmospheric Sciences at the University of Saskatchewan; the University of British Columbia and the University of Western Ontario also collaborated to the experiment.

The sensors (on loan from the University of Tokyo) consist of three induction coils aligned on the local magnetic coordinate system (H,D,Z), where the north-south line lies in the local magnetic meridian plane. The time rate of change of the magnetic flux going through the coils induces an electromotive force (emf) which is fed to a high

impedance amplifier before recording. The frequency response curve shows the corner frequency to be at  $\sim 2$  Hz, well above the range of frequencies in which we are interested. The instrument sensitivity is capable of detecting signals of amplitudes as low as  $10^{-3}$  nT.

The data were recorded on a magnetic tape by means of a multi-channel analog tape recorder, including a coded time clock, WWVB and the three components of the time rate of change of the magnetic field.

The digitization and pre-processing techniques used are summarized in Appendix A.

## 2.2 Selection of events

Pi2's are pulsations essentially associated with magnetic substorms; therefore, one would expect to detect them during active geomagnetic days, on the night side of the earth, extending from the evening sector to the early morning sector. Several types of indices have been developed to measure the geomagnetic activity, of which two are of interest to us: the Kp index and the Ae index; the Kp index is a three-hourly quasi-logarithmic scale calculated from 13 stations located between  $46^\circ$  and  $63^\circ$  latitude (geomagnetic). The Ae index is a measure of the global auroral electrojet in the auroral zone, averaged over an hour.

August 08 1983 recorded the maximum geomagnetic activity of the month with a peak value of 1282 nT during which Kp index was 8<sup>-</sup>. These indices are listed in Appendix E.

The easiest way to detect Pi2 activity in the magnetic record is to look for the characteristic 'negative bay' which marks the beginning of the expansion phase of the substorm around local midnight and in the early morning sector. For that purpose, the induction magnetometer data were integrated with a three-hour time integration

constant to extract the substorm features and, subsequently, with ten minute time integration constant to extract Pi2 activity (see Figure 1). This technique is described in more details in Appendix B.

In the evening sector, the recognition of Pi2 is more difficult because the magnetic record does not show any distinctive 'negative bay'. In that time sector, as was shown in Figure 2, the westward electrojet is weaker and an eastward electrojet forms in the equatorward half of the auroral belt. The superposition of these two electrojets makes the magnetic record more confusing.

It was fortunate, however, that a 50 MHz CW bistatic doppler radar was operated concurrent by the I.S.A.S, the scattering area being located over South End. A section of the original record was made available by Professor Sofko and is displayed together with the induction magnetometer data in Figure 7.

A distinctive characteristic of the auroral echo is that the returned signal may be broadened and/or Doppler shifted, positively or negatively, by frequencies corresponding to target velocities of up to several hundreds  $\text{msec}^{-1}$ . In the E region of the ionosphere only electrons will back-scatter radar waves (the velocity of ions is several order of magnitude less than the convection velocity of electrons). As shown by Ecklund *et al.* (1975), Greenwald and Ecklund (1975) and Greenwald *et al.* (1978), the measured radial doppler velocity varies as the cosine of the angle between the radar wave vector and the electron drift motion:  $v_r = \underline{k} \cdot \underline{v}$ ; two doppler measurements of a common volume from different directions will then give the electron drift vector  $\underline{v}$ ; and since the gyro-frequency is much greater than the collision frequency in the E region, the relation  $\underline{V} = \frac{\underline{E} \times \underline{B}_0}{B_0^2}$  will yield the value of the electric field.

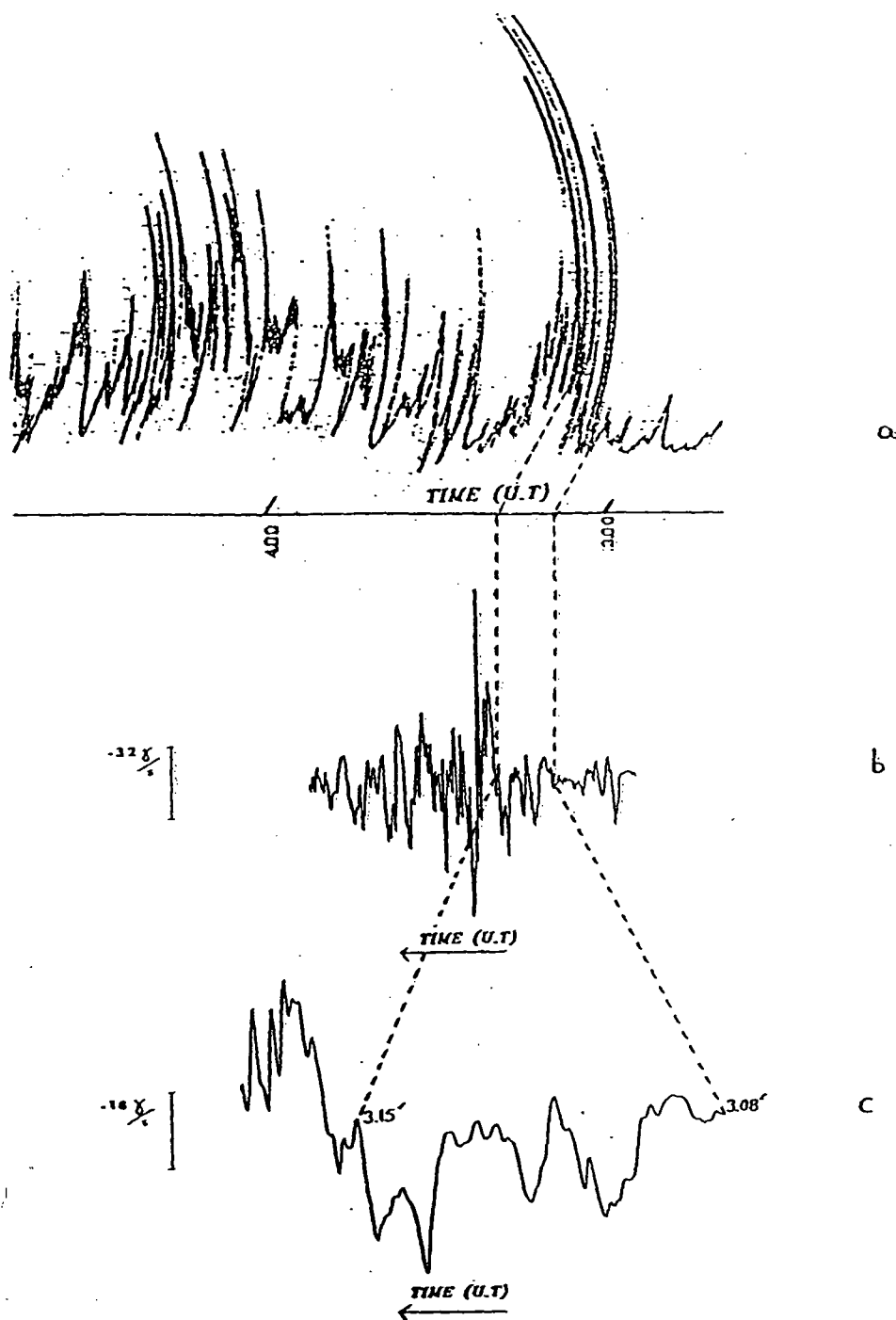
A drift velocity of  $1000 \text{ ms}^{-1}$ , corresponding to a doppler shift of 333 Hz at 50 MHz indicates an electric field of  $50 \text{ mvm}^{-1}$ . When the drift velocity is less than  $400 \text{ ms}^{-1}$ , no scattering usually takes place.

Figure 7 shows the scattered signal amplitude at the receiver. Only a fraction (1 kHz) of the 5 kHz bandwidth is recorded. Unfortunately, the amplitude scale was not made available. But, the main interest of the record is the distinctive, impulsive signature of Pi2 at 3.08 U.T. The event is well differentiated from the electrojet activity developing after 3.40'. The magnetic signature of Pi2 is not so clearly defined.

It was not the purpose of this research to analyze the radar echoes of Pi2, however a few observations between the magnetic and the radar records were helpful to select the Pi2 time intervals.

From 3.08 U.T to 3.15 U.T, the scattered signal amplitude (proportional to the enhanced local electric field) is considerably increased. At  $\sim 3.15$ , the electric field starts to weaken and the magnetic field intensifies considerably, meaning that the local ionospheric conductivity has changed, and the arrival of the electrojet overhead mixes with Pi2 power. This can be understood as follows: if conductivity suddenly increases in the ionosphere (by precipitation of electrons), polarization charges may develop at the edge of the conducting strip and weakens the local electric field, ie. the net electric field weakens where the conductivity is highest. For example, at  $\sim 3.24$ , a gap in the radar record is observed and it corresponds to a peak in the magnetic field (see Figure 7). At  $\sim 3.31$ , a second weaker impulse in the radar record corresponds to Pi2 activity in the magnetic record (see Figure 8).

Therefore, it seems reasonable to subdivide the Pi2 event into several sub-events each of which is not broken up by large conductivity changes in the ionosphere at the



**Figure 7.** Panel a: Auroral echo of a 50 mHz CW bistatic Doppler radar (operated by I.S.A.S). The scattering area is located over South End. Panel b: Simultaneous induction magnetometer data (H component). Panel c: Pi2 waveform expanded from panel b. South End, August 08, 1983.

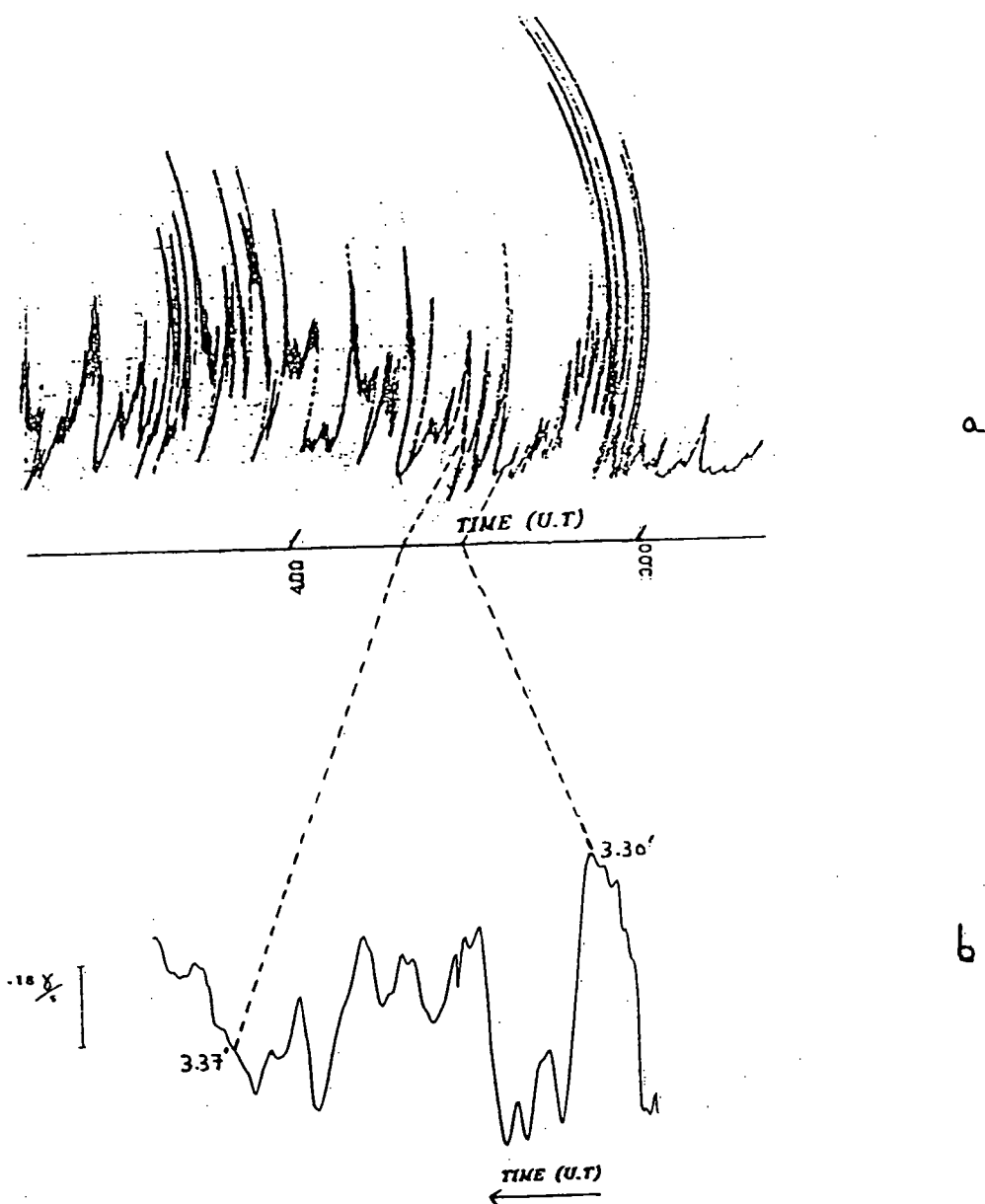


**Figure 8.** Panel a: Same as Figure 7<sub>a</sub>. Panel b: Simultaneous induction magnetometer data: Pi2 waveform (H component). South End, August 08 1983.

time. The average behaviour of the Pi2 can then be computed with more confidence using spectral analysis and polarization analysis techniques as will be explained in the next sections.

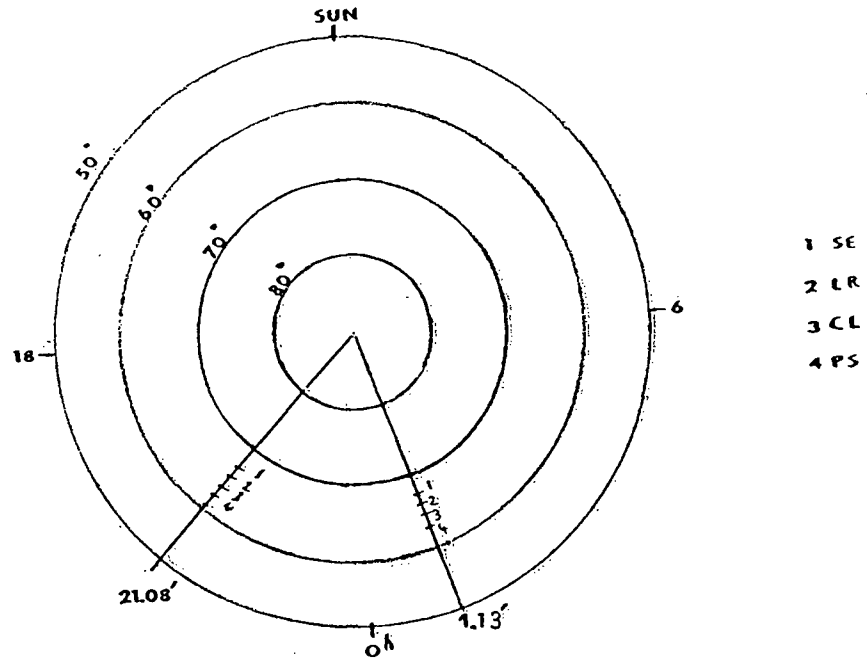
A general summary of the Pi2 time intervals used for this research is shown in Figure 9.

In the following sections, we will demonstrate the techniques used in this Pi2 research: the digital filtering, the spectral analysis and polarization analysis techniques. Before we start to process our Pi2, it is important to observe that during periods of magnetospheric activity, the power in the geomagnetic spectrum covers a wide band of frequencies with power decreasing with increasing frequency. In Figure 10, the substorm power spectra is computed for the event shown in Figure 1<sub>c</sub> (the selected time interval follows the occurrence of Pi2: 7.40'-8.00 U.T). The problem is that the Pi2 energy ( $\sim 7-25$  mHz) lies precisely within the same frequency range. Therefore, the distinction between a substorm feature and a Pi2 feature cannot be made from the spectral content of the time series alone. As mentioned before, visual inspection of the record can be ambiguous also because the irregular, impulsive character of Pi2 is sometimes a substorm electrojet characteristic.

### 2.3 Digital filters

Figure 11<sub>abc</sub> displays the result of three digital filters applied to the event shown in Figure 1<sub>c</sub>. Only the Pi2 time interval is shown in the figures. Each of them will be discussed separately. It is obvious from the Figures that the experimental result will depend entirely on the technique used.

A natural way to proceed in the time domain, is to apply a band pass filter to extract strictly the Pi2 frequencies and eliminate the substorm power outside that range.



<u>U.T</u>	<u>L.T</u>	<u>U.T</u>	<u>L.T</u>
3.08' 3.15'	21.08' 21.15'	7.13' 7.20'	1.13' 1.20'
3.16' 3.23'	21.16' 21.23'	7.21' 7.28'	1.21' 1.28'
3.30' 3.37'	21.30' 21.37'		

**Figure 9.** Pi2 events in their respective local time sector.  
 South End (SE), La Ronge (LR), Christopher Lake (CL), Park Site (PS). August 08, 1983.



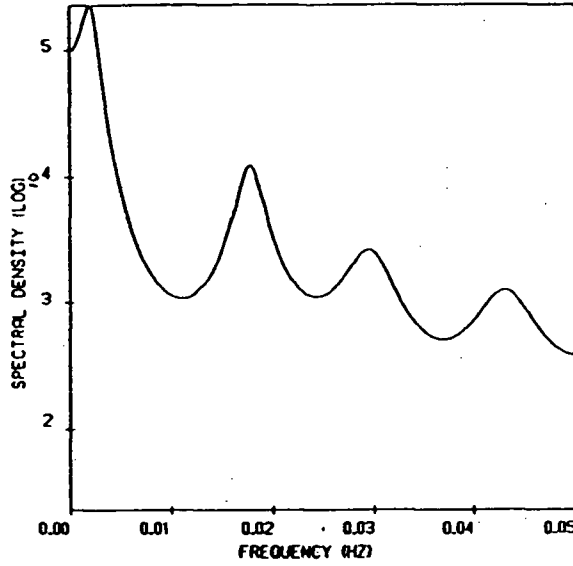


**Figure 10.** Maximum Entropy spectral density in units of  $(nT)^2/Hz$  (Burg's scheme, order at minimum FPE (13)). La Ronge, H component, 7.40'-8.00 U.T., August 08, 1983.

We applied an FIR (finite impulse response) digital filter using a Hanning smoothing window, with ideal cutoff frequencies of 5 mHz and 25 mHz (Programs for digital data processing, 1979, 5.2-1). If we denote  $N$ -point windows as  $w(n)$ , for  $0 \leq n \leq N - 1$ , and we denote the impulse response of the digital filter (obtained as the inverse Fourier transform of the ideal digital filter) as  $h(n)$ ,  $-\infty < n < \infty$ , then the windowed digital filter is given as:

$$\begin{aligned} \hat{h}(n) &= w(n)h(n) & 0 \leq n \leq N - 1 \\ \hat{h}(n) &= 0 & \text{otherwise} \end{aligned} \quad (2.1)$$

In figure 11<sub>c</sub>, we applied a 700-point Hanning window. Because our sampling frequency (0.4 Hz) is high compared to our cutoff frequencies, the filter acts as a narrow band pass with sharp transition bands and therefore, it produces in the filtered magnetogram

oscillations which do not stem from real geomagnetic pulsation activity (see Figure 11<sub>c</sub>). The nature of the data itself gives the same major problem: the Pi2 is initiated at the onset of the 'negative bay', or accompanies a sudden change in the background magnetic field. A sudden change will cause any bandpass filter to ring. Furthermore, there is no guarantee that, in the filtered data, there might not be still a mixture of substorm and Pi2 activity. The use of this technique was therefore rejected.

A second technique was experimented in this research. The polarization filters, originally developed by J.C Samson (Samson, 1981), is widely used now in micropulsation study. The calculations are derived in more details in Appendix B; the foundation of the technique and its assumptions are discussed here. This technique assumes that the micropulsation energy is a quasi-monochromatic plane wave of the form:

$$\begin{aligned}\underline{H}(t) &= A_1(t) \exp i(\underline{k} \cdot \underline{r} - \bar{\omega}t + \phi_1(t)) \\ \underline{D}(t) &= A_2(t) \exp i(\underline{k} \cdot \underline{r} - \bar{\omega}t + \phi_2(t))\end{aligned}\tag{2.2}$$

where  $H(t)$  and  $D(t)$  are the horizontal components: N-S and E-W, the frequency variations ( $\Delta\omega$ ) around the central frequency ( $\bar{\omega}$ ) are small ( $\frac{\Delta\omega}{\bar{\omega}} \ll 1$ ).

If the ratio of the amplitudes and the difference in the phases are time independent, so that  $q = \frac{a_2(t)}{a_1(t)}$  and  $\delta = \phi_1(t) - \phi_2(t)$  are constant, then the quasi-monochromatic wave will behave approximately like a monochromatic wave (Born and Wolf, 1975, p.550).

The second assumption made by the technique follows from the first and is based on a Pi2-substorm model which is not yet fully understood: the substorm electrojet generates a broad band power on the ground, and therefore, if Pi2 energy lies in the same frequency band as the substorm energy, it seems reasonable at first to assume that the substorm power is less polarized than the micropulsation (the magnetic vector oscillates

in a random way). Figure 12 gives a good visual representation of what we mean by polarization.

Following this idea, the time series can then be considered as the sum of polarized and unpolarized power. This superposition principle is largely used in optics and says that if independent light waves propagating in the same direction are superposed, the spectral matrix of the resultant wave is the sum of the spectral matrices of the individual waves. If this is true for the electric field, it is also true for the magnetic field (Born and Wolf, 1975, p. 24)

The filter calculations are done in the frequency domain, using the spectral matrix which is formed from the power and cross power of the H and D component. We form the spectral matrix, calculate at each frequency the % polarization (which is the ratio of the polarized power to the total power), weight the Fourier transform accordingly so that, for instance, the 5 % polarized spectral peak will be suppressed, enhancing considerably the 95 % peak, and finally, we inverse Fourier transform (see Figure 11<sub>a</sub> and 13). There are two more difficulties to point out: this filter design assumes that the noise is white. Our ionospheric substorm noise is however bandlimited and has some degree of correlation: in Figure 13, the minimum in % polarization (assumed to be noise) is 40 %; therefore, noise will remain in the output. The other difficulty is that the % polarization computation fails for short time series. Although the result of this filtering technique looks quite nice, the validity of the assumptions made can be discussed.

The third technique used in this research eliminates the difficulties of the two others: it does not act as a narrow band pass filter and therefore guarantees no intrusion of artificial peaks; secondly, it does not assume that the Pi2 is 100 % polarized; it simply performs the integration of the time derivative of the magnetic field using a time

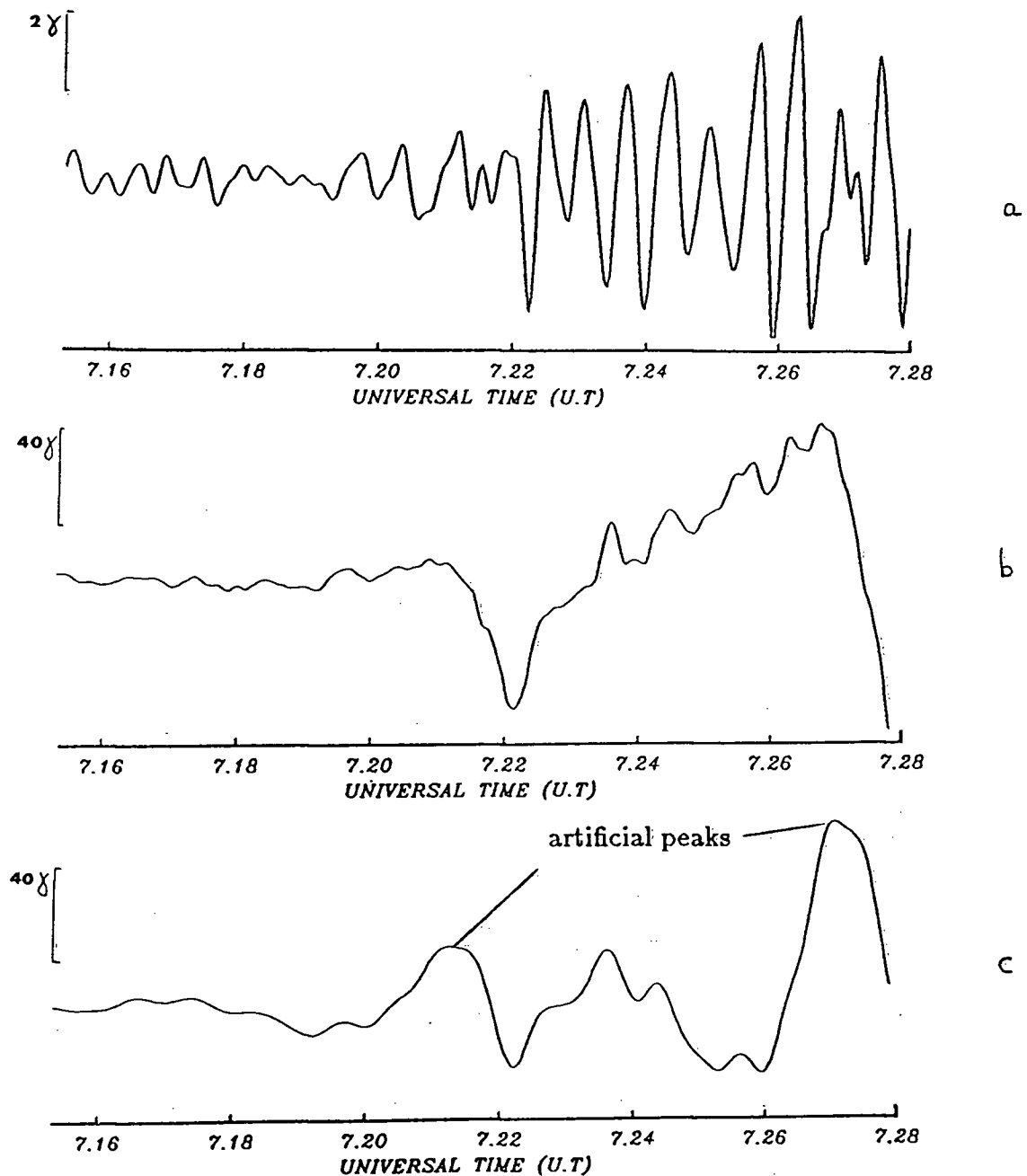


**Figure 11.** Panel a: Weighting polarization filter (the selectivity is increased by raising the % polarization,  $R$ , to the third power). Panel b: Integrator (ten-minute time integration constant). Panel c: Band pass filter (5-25 mHz), 700-points smoothing Hanning window.

La Ronge, H component, August 08, 1983.

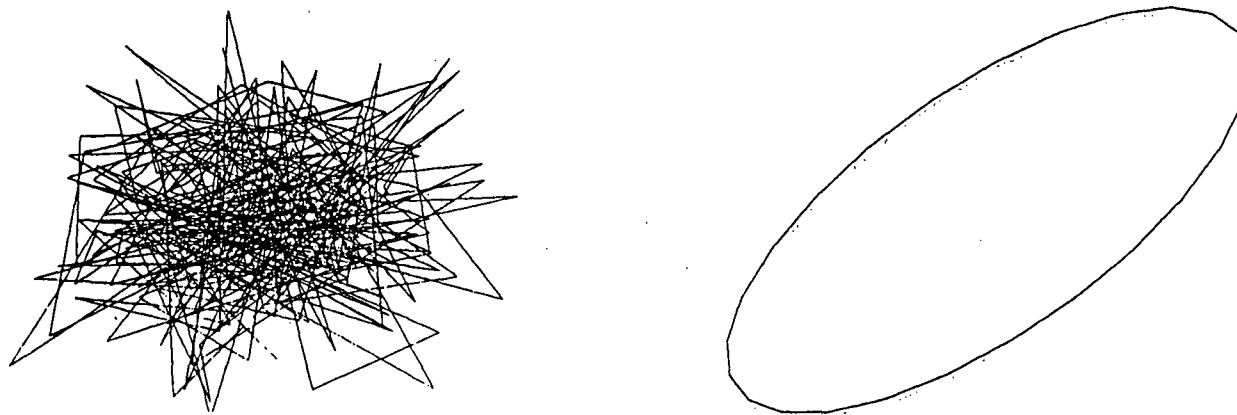


**Figure 12.** Left: Particle motion of two-channel white noise. Right: 100 % polarized pair of sinusoids phase shifted by  $\pi/4$ .

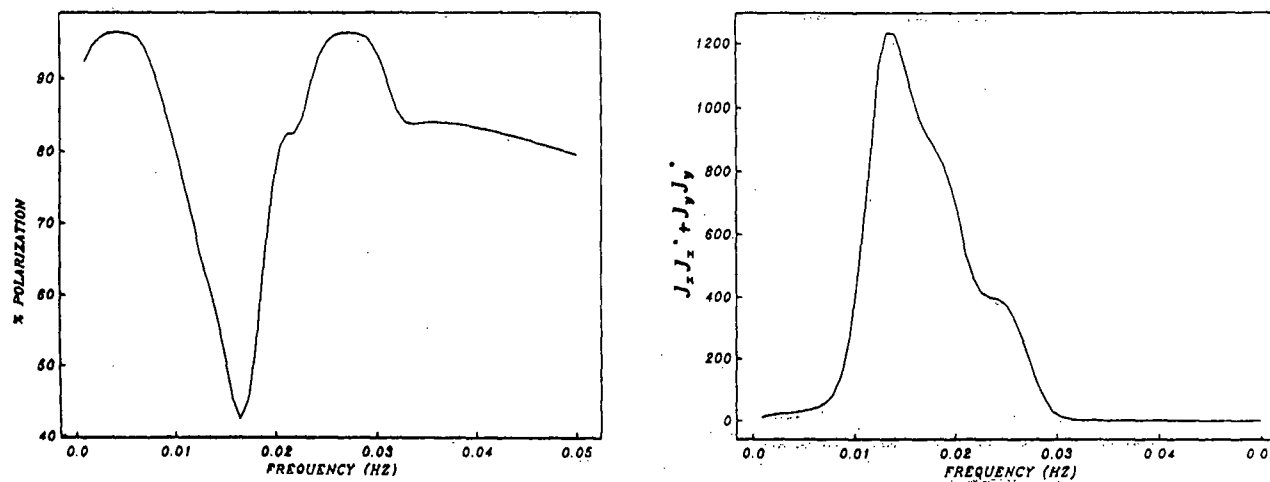


**Figure 13.** Right: Trace of the spectral matrix in units of  $(\text{nT})^2/\text{Hz}$ .  
Left: Associated % polarization.  
La Ronge, H and D component, 7.15'-7.28' U.T, August 08, 1983.

integration constant on the order of Pi2 time scale: ten minute. The integrator acts only under the conditions that the period  $T \ll \tau$  is satisfied. As can be seen in Figure 11<sub>b</sub>, periods  $\leq 1$  minute are the only ones emphasized by this integrator. This technique, suggested to me by T. Watanabe, was selected among the others because it extracts probably the most accurately the actual Pi2 waveform.

The outcome of this analysis is interesting: the band pass filter gives artificial peaks, and the polarization filter makes an assumption which may not be valid: if we compare closely Figure 11<sub>a</sub> and Figure 11<sub>b</sub>, the 60 sec period waveform (Figure 11<sub>b</sub>) has been completely suppressed (Figure 11<sub>a</sub>), leaving only the 35-40 sec harmonics. Since the 60 sec period was clearly observed at Southend as well as at La Ronge (see Figure 1<sub>b</sub> and 1 - d). using the third technique, it was selected as real and not noise; therefore, there are two possibilities: either the 35-40 sec waveform is harmonically related to the Pi2, or it arises from a different source mechanism. What is presently believed is that the Pi2 is disturbed by the dynamic development of the substorm to such a degree that the polarization filter assumptions might not be valid.

## 2.4 Spectral analysis

In the frequency domain, different spectral estimators were also investigated. The different techniques used are shown together in Figure 14 for comparison (computed from Figure 1<sub>d</sub>). The periodogram power or the amplitude square of the Fourier transform gives an exact measure of the power or energy at any given frequency. The truncation of the time serie with the addition of zeros produces side lobes on either side of the peak and this effect proved to be particularly strong for our time series selection: one can barely identify the peaks (see Figure 14<sub>c</sub>).

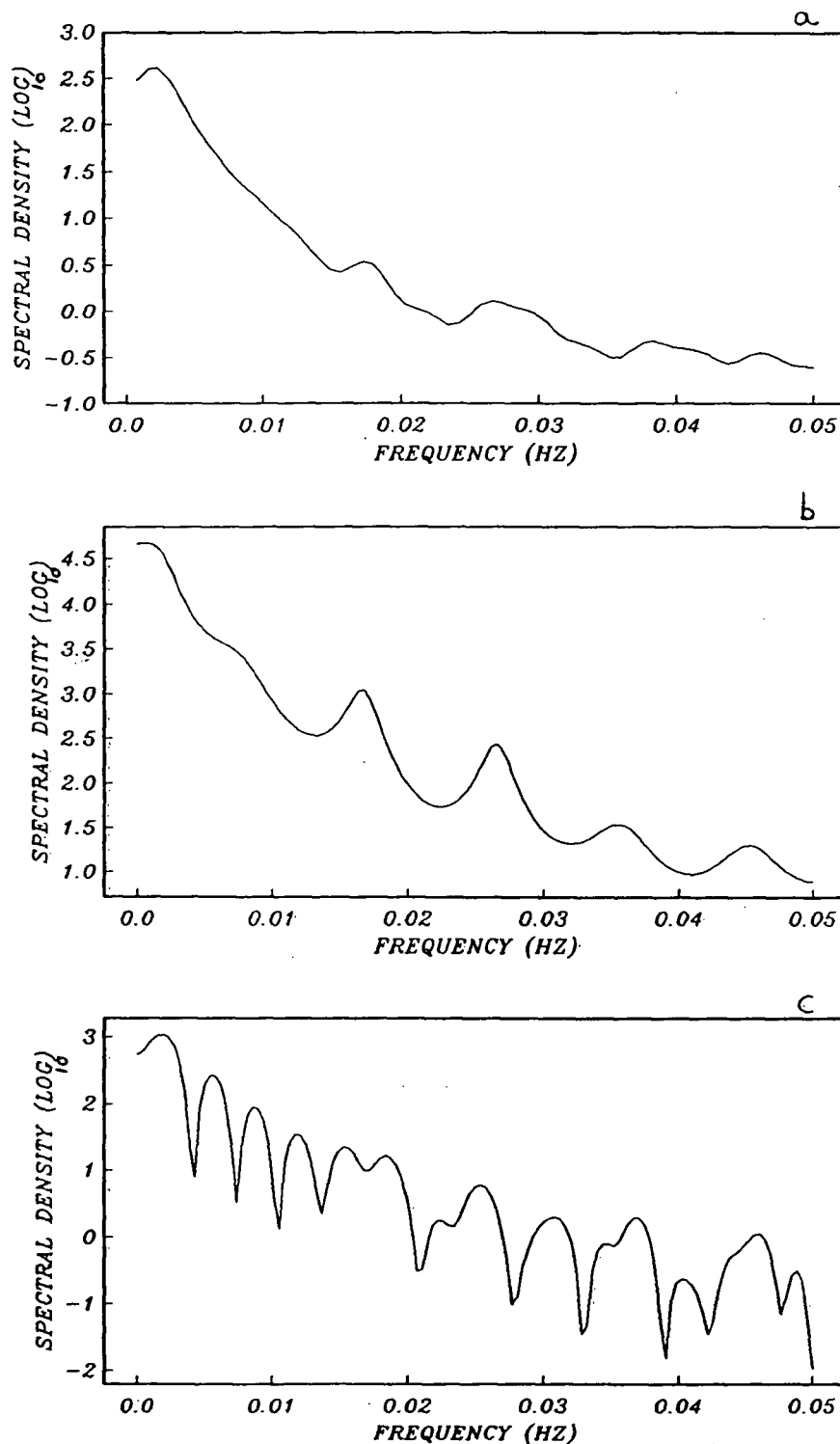


**Figure 14.** Spectral estimates of the Pi2 event illustrated in Figure 1<sub>d</sub>. All spectral densities are expressed in units of  $(nT)^2/Hz$ . Panel a: Smoothed power spectra (Bartlett window with 7 degrees of freedom). Panel b: Maximum Entropy Method (Burg's scheme, with AR order at minimum PFE (13)), the amplitude of this estimator is unreliable. Panel c: Raw power spectra (periodogram).

La Ronge, H component, 7.20'-7.28' U.T, August 08, 1983.

The variance of the spectral estimates can be reduced by weighting the periodogram  $C_x C_x^*(f)$  over a small range of frequencies. This is done by convolving the power spectra with a window to obtain the band averaged power:

$$\overline{C_x C_x^*}(f') = \frac{1}{\Delta f} \int_{-\infty}^{\infty} C_x C_x^*(f) W(f' - f) df \quad (2.3)$$

A Bartlett smoothing window is applied to the data:

$$W(f') = T \left( \sin \frac{\pi f' T}{\pi f' T} \right)^2 \quad (2.4)$$

where  $T$  specifies the length of the time serie (Kanasewich, 1981, p.458). The resulting spectra is shown in Figure 14<sub>a</sub>: a smoothed power, with decreased resolution but increased stability ; the effective resolution of the spectrum is now 2.5 mHz which means that two peaks closer than 2.5 mhz will be smeared into one. The power is now defined as a power spectral density or power per bandwith (2.5 mhz). This technique will be used to compare the relative power of Pi2 at different latitudes.

The maximum entropy method is also presented in this analysis (see Figure 14<sub>b</sub>). The potential superiority of M.E.M over other spectral estimators, in particular for short data lengths, is by now well recognized. Although the remarkable resolution property of this technique is its main appeal, the method has three main difficulties, the first being the lack of criterion for choosing the length of the prediction error filter, the second being that the amplitude of the spectral peaks cannot be determined accurately, the third being the lack of a variance estimate (Ulrych, 1975). However, the method is very useful in our case, not to compare the relative Pi2 power at the stations, but to detect



with high resolution the frequency variations of Pi2 versus latitude and the frequency variations from the H component to the D component.

## 2.5 Polarization analysis

Even though the Pi2 is disturbed by the dynamic development of the substorm, we can still attempt to analyze its polarization properties in the horizontal plane. The best method to use is the dynamic approach: plotting directly from the filtered data (using the third technique described above) the tip of the magnetic vector. The patterns were too complicated to follow in most cases. Applying a narrow band filter will lead into the problems exposed previously. Therefore, we need to average the Pi2 polarization characteristics over the selected time interval using another technique.

The complete derivation of the averaged polarization parameters can be found in Born and Wolf, 1975, p. 547. In Figure 15, we define our coordinate system and the angle used for this computation.

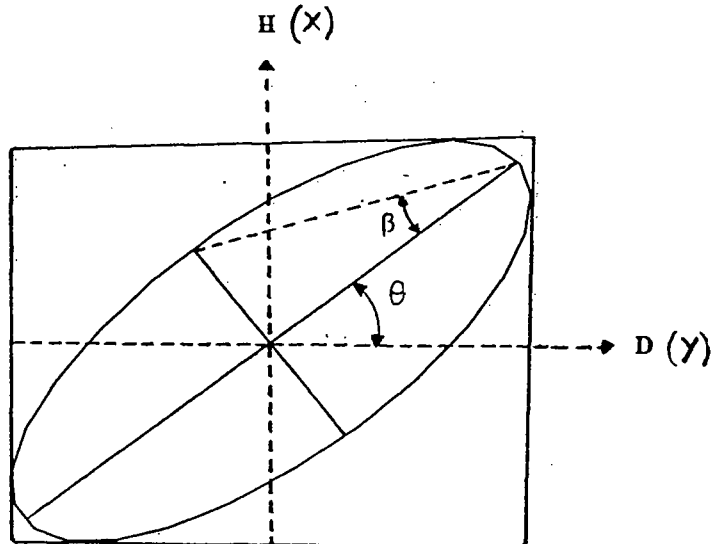


**Figure 15** Elliptically polarized wave. The vibrational ellipse for the magnetic vector.

1. The angle  $\theta$  of the major axis of polarization is measured counter-clockwise from the D (Y) axis and is defined by:

$$\tan 2\theta = \frac{2\text{Re}(J_{xy})}{(J_{xx} - J_{yy})} \quad (2.5)$$

where J is the spectral matrix formed from the power and cross-power spectra of the original data:

$$J = \begin{pmatrix} J_{xx} & J_{xy} \\ J_{yx} & J_{yy} \end{pmatrix} \quad (2.6)$$

2. The ellipticity is defined as the ratio of the length of the minor axis to the major axis and is given by the numerical value of  $\tan \beta$ .  $\beta$  can be expressed in terms of the spectral matrix J as follows:

$$\sin 2\beta = \frac{2\text{Im}J_{xy}}{(Tr^2(J) - 4 \det J)^{\frac{1}{2}}} \quad (2.7)$$

A negative ellipticity means that the magnetic vector is rotating clockwise when viewed in the direction of the earth's field.

These derivations are also based on the assumption that the Pi2 is a quasi-monochromatic plane wave. As discussed earlier, at the present time, it is difficult to say how many spectral peaks Pi2 contains, and whether the peaks found in the Pi2 band are harmonically related or originate from different source mechanism(s). It is therefore difficult to evaluate the damping characteristic of Pi2.

This polarization technique was tested with a synthetic example chosen not to represent the actual waveforms of the Pi2 and the substorm, but their relative power. Six damped

sinusoids (three X-Y pairs) of 15, 20 and 30 mHz were hidden in some artificial substorm power in the typical ratios found in the real data (see Figure 16):

$$\begin{aligned} Y(t) &= 10 \sin \omega t + \left( 3 \sin(3\omega t + \frac{3\pi}{4}) + \sin(4\omega t + \frac{5\pi}{4}) + 0.3 \sin(6\omega t + \frac{7\pi}{4}) \right) e^{-at} \\ X(t) &= 10 \sin \omega t + \left( 3 \sin 3\omega t + \sin 4\omega t + 0.3 \sin 6\omega t \right) e^{-at} \end{aligned} \quad (2.8)$$

where  $\omega = 2\pi f$  and  $f=5$  mHz,  $a=1.4 \times 10^{-3}$  is the damping factor chosen to be the same for all three sinusoids (the amplitude of the signals after 8 minutes being  $\frac{1}{2}$  of that at time  $t=0$  is a reasonable choice).

The best way to represent the phase difference between each individual pair of sinusoid ( $\Delta\phi = \phi_y - \phi_x$ ) is to plot the polarization ellipses (see Figure 17<sub>abc</sub>). In this Figure, the inward spiralling is obviously associated with the signal damping. Since the damping factor of the X and Y component is the same, the ellipticity remains constant in all three cases. The polarization parameters are computed using (2.5) and (2.7) from the original synthetic data and the result can be compared with the known values (see Table 2).

Frequencies	$\phi_y - \phi_x$	DB down from max	Rotation angle	Ellipticity
15 mHz	$\frac{3\pi}{4}$	15	known: $-45^\circ$ computed: $-45^\circ$	known: 0.41 (ccw) computed: 0.41 (ccw)
20 mHz	$\frac{5\pi}{4}$	23	known: $-45^\circ$ computed: $-55^\circ$	known: -0.41 (cw) computed: -0.38 (cw)
30 mHz	$\frac{7\pi}{4}$	27	known: $45^\circ$ computed: $75^\circ$	known: -0.41 (cw) computed: -0.05 (cw)

**Table 2.**

At a power 27 db down from the maximum power, the angle  $\theta$  was derived with an error of  $30^\circ$ , which gives, within a total variable of  $180^\circ (\pm 90^\circ)$ , an error estimate of 17 %; the ellipticity which is a measure of the phase difference between the two components was derived with an error of 0.36 which gives within a total possible variable of 2 (-1 to 1), an error estimate of 18%.

From this synthetic example it was found that the polarization parameters could be computed with  $\approx 80\%$  confidence for a signal  $\approx 30$  db down from the maximum sub-storm power. This particular example represents the weakest Pi2 event analyzed in this research; this technique was therefore applied to the data. In the present study, the spectral peaks are studied independently using the error criteria developed by the synthetic example and the results of the analysis will show whether they are harmonically related or if they originate from different sources.

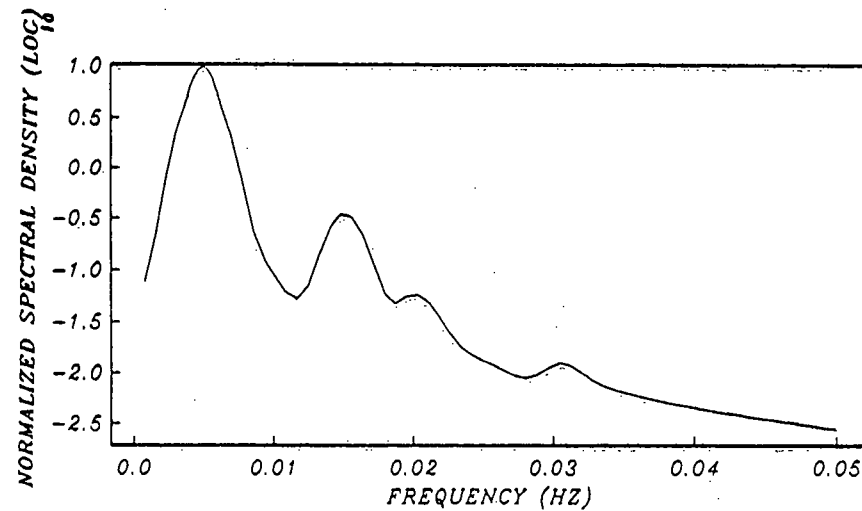


**Figure 16.** Smoothed power spectra of the following two-channel series:

$$Y(t) = 10 \sin \omega t + \left( 3 \sin(3\omega t + \frac{3\pi}{4}) + \sin(4\omega t + \frac{5\pi}{4}) + 0.3 \sin(6\omega t + \frac{7\pi}{4}) \right) e^{-at}$$

$$X(t) = 10 \sin \omega t + \left( 3 \sin 3\omega t + \sin 4\omega t + 0.3 \sin 6\omega t \right) e^{-at}$$

where  $\omega = 2\pi f$  and  $f=5\text{mHz}$ ,  $a=1.4 \times 10^{-3}$  is the damping factor ( the amplitude of the signals after 8 minutes is 0.5 of that at time  $t=0$ ).

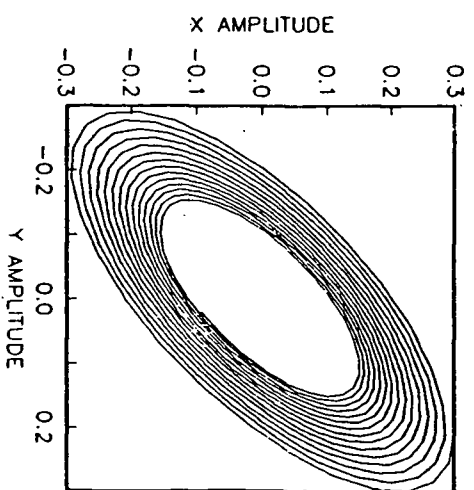
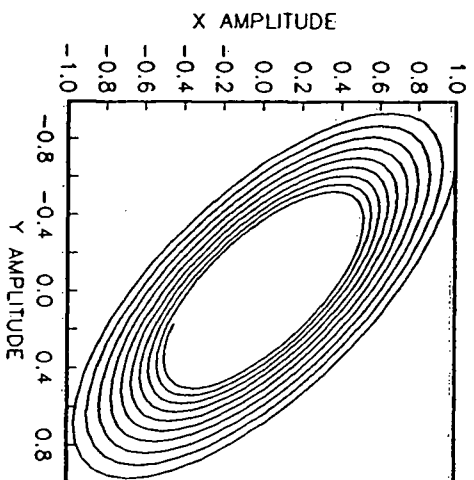
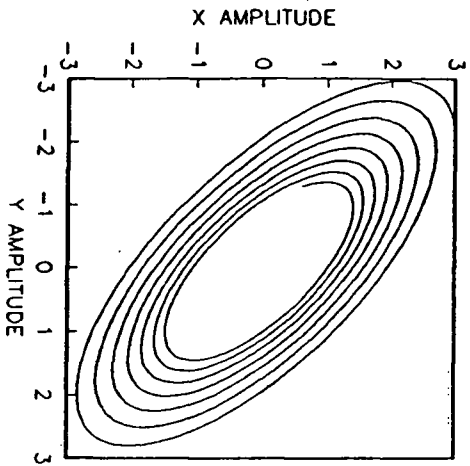


**Figure 17.**

Panel a: 15 mHz X-Y pair:  $X(t) = (3 \sin 3\omega t)e^{-at}$ ,  $Y(t) = (3 \sin(3\omega t + \frac{3\pi}{4}))e^{-at}$ .

Panel b: 20 mHz X-Y pair:  $X(t) = (\sin 4\omega t)e^{-at}$ ,  $Y(t) = (\sin(4\omega t + \frac{5\pi}{4}))e^{-at}$ .

Panel c: 30 mHz X-Y pair:  $X(t) = (0.3 \sin 6\omega t)e^{-at}$ ,  $Y(t) = (0.3 \sin(6\omega t + \frac{7\pi}{4}))e^{-at}$ .

where  $a = 1.4 \times 10^{-3}$  and  $\omega = 2\pi f$  ( $f = 5\text{mHz}$ ).

## Chapter 3

The electric coupling between the ionosphere and the magnetosphere is fundamental to the understanding of such phenomena as magnetic substorms and the associated Pi2 micropulsations. Due to the high electrical conductivity along geomagnetic field lines that connect these regions, the large scale distribution of the electric fields in the ionosphere E and F layers is an image of the magnetospheric field distribution and vice versa.

Sudden changes in the currents or voltages taking place in the ionosphere or the magnetosphere disturb the electric balance, and may cause intense currents to flow along these field lines, resulting in oscillations of the 3-D current system. At the same time, the magnetic lines of force themselves can be perturbed through a variety of plasma instabilities, generating hydromagnetic waves. We believe that the Pi2 generation and propagation lie in the coupling mechanism under these disturbed conditions. In this chapter, we deal with the types of ground magnetic oscillations that we might expect from the electric coupling between the ionosphere and the magnetosphere. Two preliminary Pi2 models are presented: the first one uses lumped circuit elements to model the magnetosphere-ionosphere interaction, the second one examines the possibility of an ionospheric electric impulse imparted to a field-aligned current (FAC) under the conditions of the brightening of the aurora. †

### 3.1 The lumped circuit elements model

---

† Throughout this work, the curvature of the earth's surface and of magnetic field lines is ignored. The FAC's are replaced by vertical electric currents and the ionosphere is treated like a thin plane of uniform electric conductivity.

The generation of micropulsation activity as an alteration of such magnetosphere-ionosphere current system has been considered by many people. Boström (1972) explained the Pi2 micropulsations as the resonant oscillation of the 3-D current system of the magnetic substorm (his parameters are, however, only rough estimates). Lam and Rostoker (1978) explained the early morning Pc5 micropulsation activity in the same fashion. Reid and Holzer (1975) and many others have looked at the coupling between the magnetosphere and the ionosphere similarly.

These past efforts to model the magnetosphere-ionosphere coupling have used idealized electric circuits with lumped impedances: capacitors, resistors and inductors. The magnetosphere is the main voltage generator, which stems from charge separation due to the differential motion of protons and electrons as plasma is injected from the tail towards the inner magnetosphere. † The resistance is associated with the ionosphere, while the inductance is a function of the geometry of the current system.

A sudden change in the electric field strength in a localized region of the nightside magnetosphere will be transferred in the circuit with a characteristic time constant  $(LC)^{\frac{1}{2}}$ . Since the Pi2 is observed at the early stage of the magnetic substorm, when sudden electric field changes take place in the magnetosphere, it is reasonable to attempt to model the micropulsation as LC oscillations. Our first model extends the LC circuit analogy further: we associate the Pi2 with the magnetic field of a system of resonant LC circuits developing symmetrically to the west and to the east of a growing magnetospheric potential source, lying in the equatorial plane.

---

† The injection of plasma into the inner magnetosphere represents one of the consequences of the energy transfer from the solar wind to the earth's magnetosphere and depends on the Interplanetary Magnetic Field (IMF) conditions.

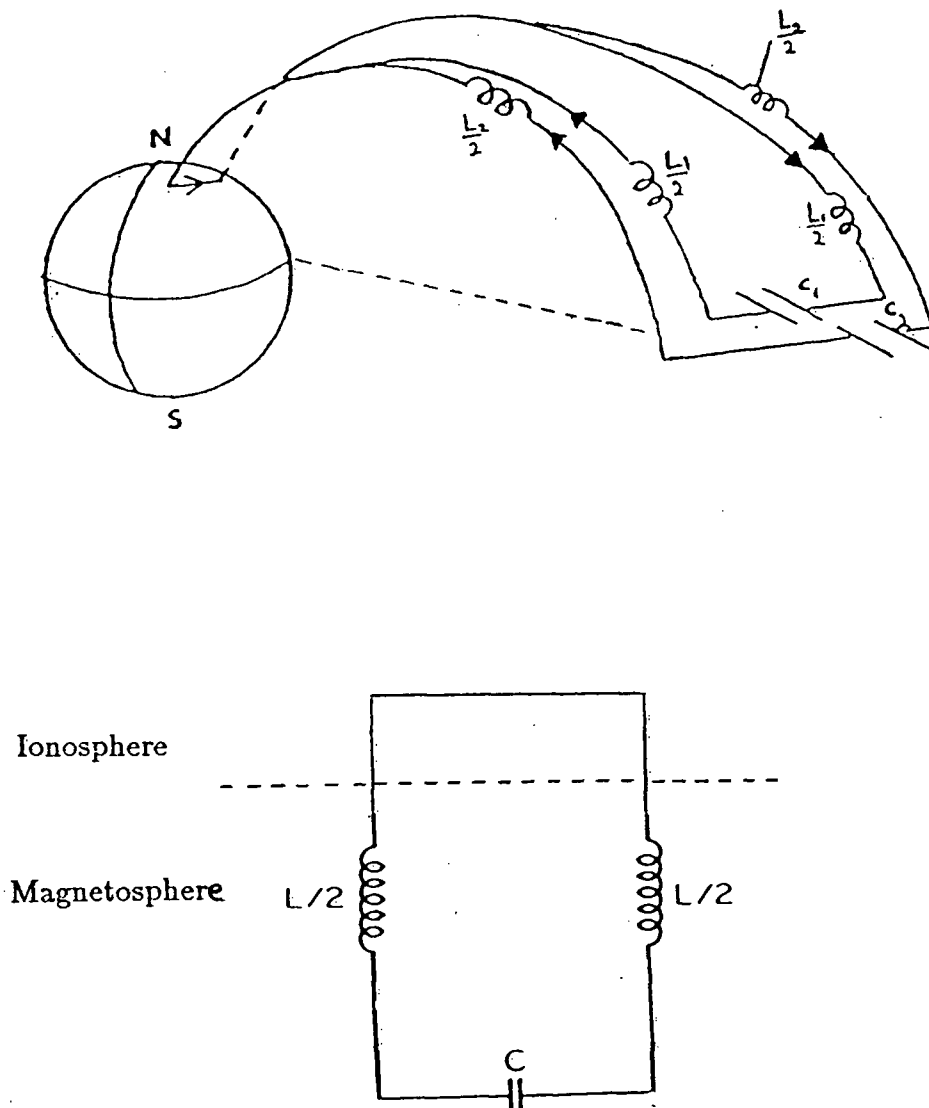


Figure 18 gives a 'snapshot' representation of an expanding network of LC circuits in the magnetosphere. At the onset of the expansion phase of the substorm, the main voltage generator is switched on in the magnetosphere, a potential drop builds up across the drifting magnetized plasma or energy is stored in the equivalent capacitor  $C_1$ , the current starts to flow in FAC1 and the electric field energy is progressively transferred to the magnetic field of the inductor  $L_1$ . As more plasma is injected from the tail, additional electric field energy is stored in the capacitor  $C_2$  which starts to discharge through FAC2. Because a time delay exists between the onset of the  $L_1C_1$  and  $L_2C_2$  oscillations, the current flowing in FAC2 is phase shifted with respect to the current flowing in FAC1, similarly FAC3 with respect to FAC2 and FAC1 and so on. Each additional FAC current pair forms an independent LC circuit, symmetrically around the potential source and oscillates at its natural frequency.

In order to obtain quantitative predictions from the model, one must specify the LC parameters. Deriving the magnetospheric capacitance requires the computation of the kinetic energy of the magnetospheric plasma which requires other parameters such as the plasma velocity, the number density and its corresponding volume element. These calculations are not derived at the present time. Reasonable assumptions based on observations and physical intuition are sufficient to test what is only a preliminary model.

It is postulated that the resonant angular frequency of each circuit is the same:

$$\omega = (L_1C_1)^{-\frac{1}{2}} = (L_2C_2)^{-\frac{1}{2}} = \dots = (L_nC_n)^{-\frac{1}{2}} \quad (3.1)$$



**Figure 18.** Top: snapshot representation of a symmetrically growing magnetospheric potential source lying in the equatorial plane. The equivalent electric circuit elements  $L$  and  $C$  represent the inductance of the field-aligned currents ( $L_1$  associated with FAC1,  $L_2$  with FAC2 ... ) and the capacitance of the drifting plasma respectively. The LC circuits develop symmetrically to the west and to the east and oscillate at their own natural frequency (mutual inductance is neglected). The FAC's are phase shifted one with respect to the other. Bottom: equivalent single loop.

It is also postulated that each closed circuit carries the same maximum current:

$$I_{max} = I_{1max} = I_{2max} = \dots = I_{nmax} \quad (3.2)$$

Therefore it is easy to show that each capacitor stores the same amount of charge,  $q$ .

The maximum stored energy in each capacitor must equal the maximum stored energy in each inductor:

$$\begin{aligned} \frac{1}{2}C_1V_{1max}^2 &= \frac{1}{2}L_1I_{1max}^2 \\ \frac{1}{2}C_2V_{2max}^2 &= \frac{1}{2}L_2I_{2max}^2 \\ &\vdots \\ \frac{1}{2}C_nV_{nmax}^2 &= \frac{1}{2}L_nI_{nmax}^2 \end{aligned} \quad (3.3)$$

where  $V_{1max}, V_{2max}, \dots, V_{nmax}$  are the maximum voltages across the individual capacitors.

Solving for  $I_{max}$  gives:

$$I_{max} = V_{1max}\sqrt{\frac{C_1}{L_1}} = V_{2max}\sqrt{\frac{C_2}{L_2}} = \dots = V_{nmax}\sqrt{\frac{C_n}{L_n}} \quad (3.4)$$

Replacing (3.1) into (3.4) gives:

$$q = C_1V_{1max} = C_2V_{2max} = \dots = C_nV_{nmax} \quad (3.5)$$

where  $C_1, C_2, \dots, C_n$  are the successive additions of capacitors as the potential drop across the drifting plasma increases. In the present work,  $C_n$ ,  $V_n$  and  $L_n$  are not quantitatively derived.

The ionospheric view of the same physical process is more complicated (see Figure 19-20). Following the discussion of Chapter 1, each FAC diverges in the ionosphere as Pedersen currents, the associated Hall current is however divergence free and closes in the ionosphere (modelled as circular for simplicity).

The Hall current oscillates with the same period as the FAC, successively clockwise (associated with the downward FAC (+)) and counterclockwise (associated with the upward FAC (-)). Since the LC parameters are not derived, the frequency has to be postulated: it is fixed at 16.7 mHz throughout this work.

In Figure 20, the initial FAC is downward to the west of the potential source and expands in a westward direction (initial upward to the east of the potential source and expands eastward). This ionospheric configuration should be compared with the preceding magnetospheric diagram.

As discussed in Chapter 1, assuming uniform conductivity, the Hall currents are the only magnetic effects observed on the ground.

A model of the physical process described above has been implemented on the computer. The first version of the model computes at the ground the magnetic effects of a single DC current loop lying at ionospheric height (110 km). A more realistic model of the Hall current should include concentric loops carrying currents of decreasing amplitudes as one goes further away from the point of incidence of the FAC.

The amplitude of the Hall current has to be determined from the magnetospheric parameters as well as the ionospheric electric fields parallel to the Pedersen currents. These

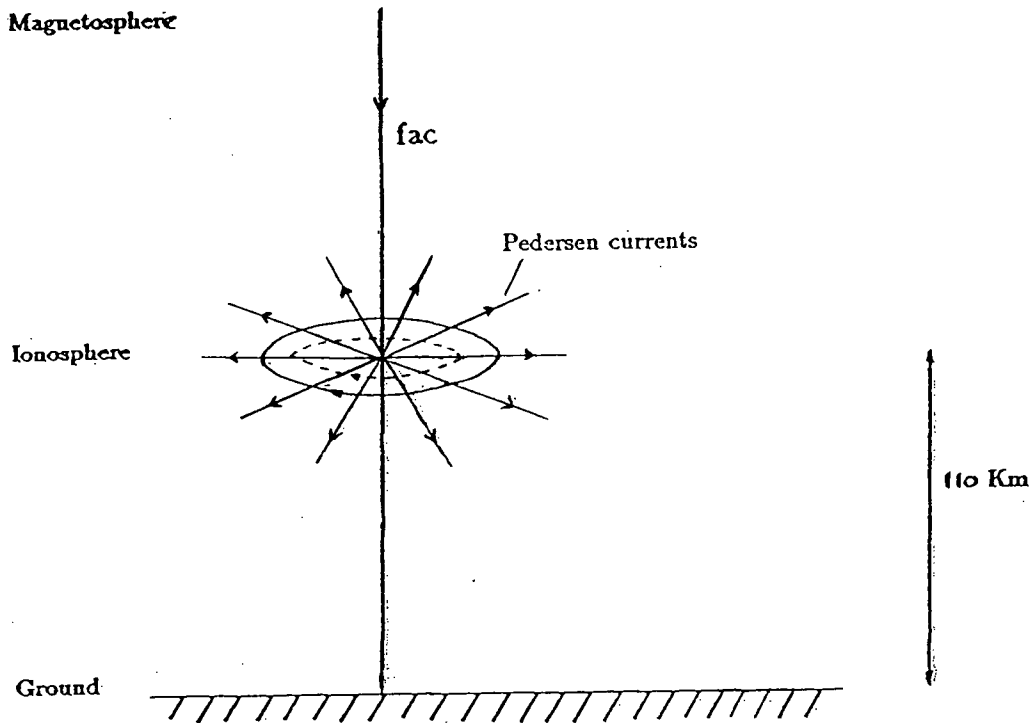


**Figure 19.** The FAC diverge in the ionosphere as Pedersen currents. The associated Hall current closes in the ionosphere.

presently unknown parameters make the numerical estimation of the Hall current difficult. Since the purpose of this preliminary model is to test the relative amplitudes and spatial variations produced by this dynamic current system, we can fix our amplitude in a reasonable way, using observed ionospheric current density.

In the auroral ionosphere, a current density of  $3\text{ A/m}$  integrated over a width of  $100\text{ km}$ , giving a total current amplitude of  $3 \times 10^5\text{ A}$  is not unreasonable. The current flowing through an analog single loop of  $50\text{ km}$  radius is therefore chosen to be  $3 \times 10^5\text{ A}$ . (This parameter might be revised in subsequent studies). The horizontal ground magnetic field generated by the DC loop carrying a total current of  $3 \times 10^5\text{ A}$  is shown in Figure 21. The amplitude of the perturbation reaches a maximum at  $70\text{ km}$ ; an

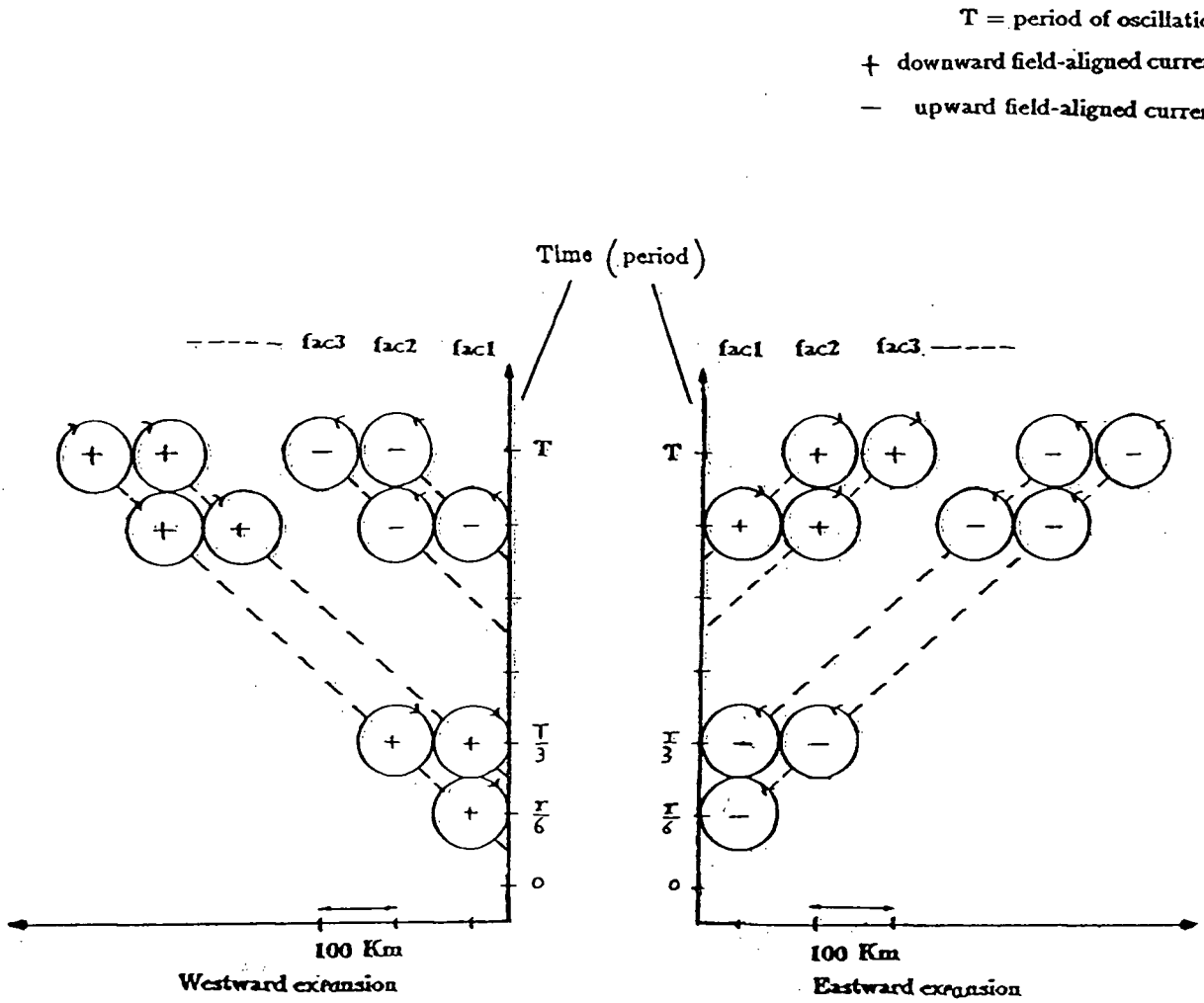


**Figure 20.** Longitudinal expansion of the induced AC Hall currents. The frequency of oscillation is assigned by the local fac passing through the center of the loop. Each step in the expansion is associated with a phase lag in the current:  $\Delta\phi = \frac{\Delta t}{T} \times 2\pi$ .

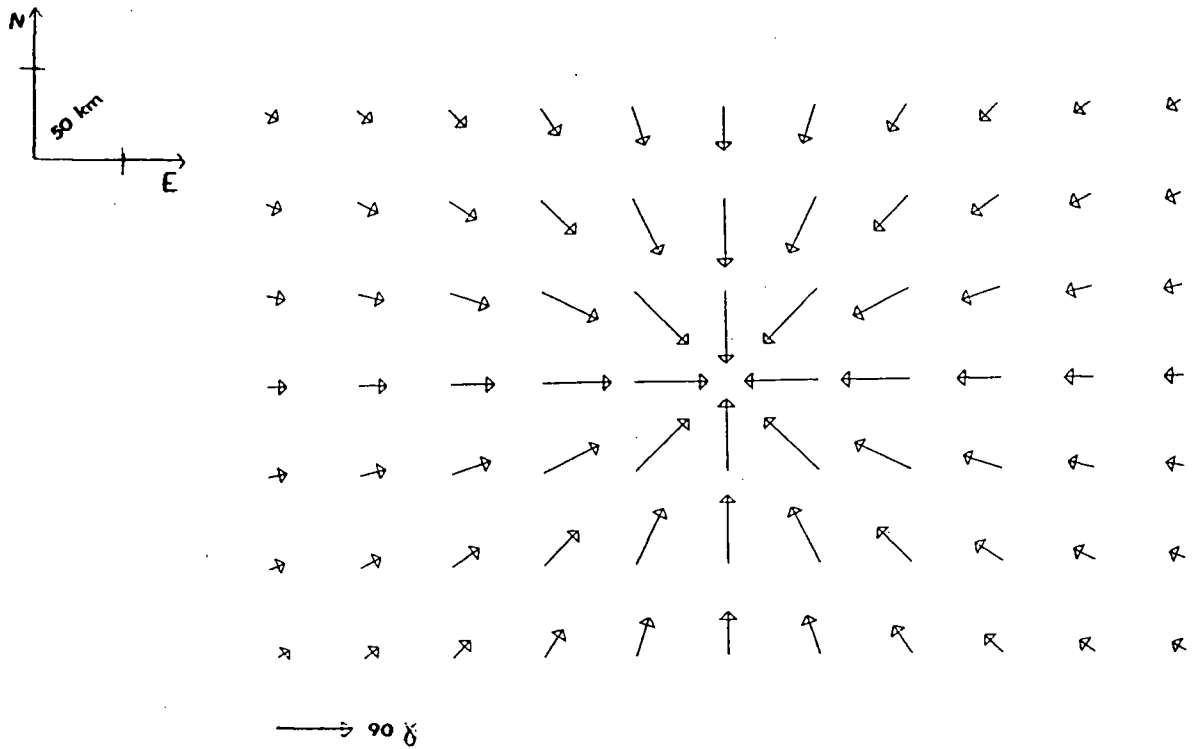


**Figure 21.**Horizontal vector field generated by a current loop of radius 50 km, lying at ionospheric height (110 km), and carrying a current of  $3 \times 10^5 A$  (ccw).

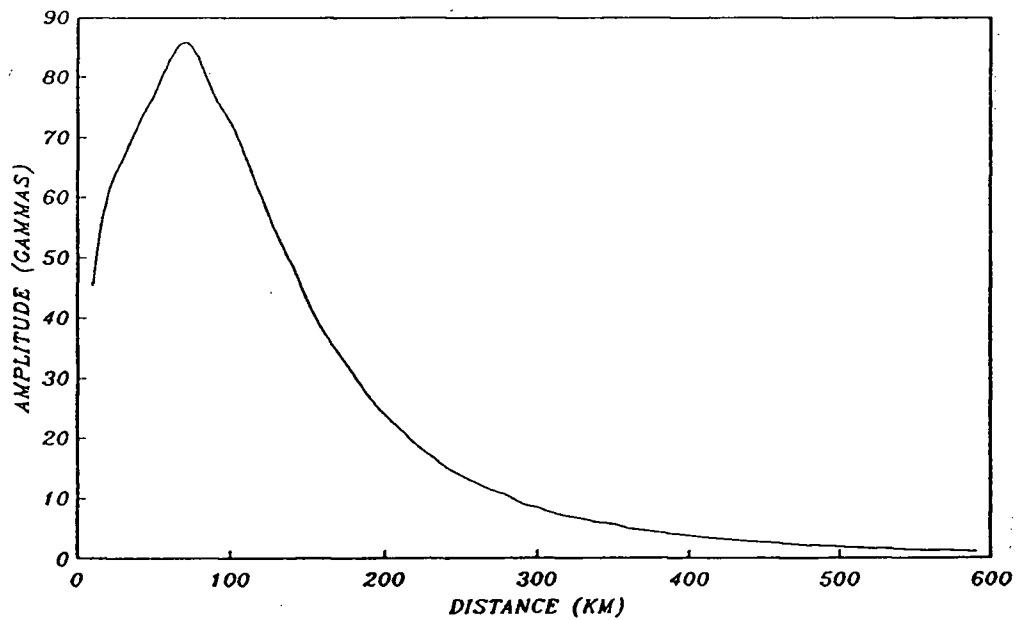


**Figure 22.**Amplitude of the vector field shown in Figure 21. Distance increases radially outward from the orthogonal projection of the center of the loop on the ground (assuming a flat earth).

km ; an exponential-like decay takes place beyond that point (See Figure 22). The calculations are derived in Appendix C.

As discussed earlier, our purpose is to model an expanding network of induced AC Hall current, the frequency being assigned by the resonant frequency of the circuit (the frequency is fixed at 16.7mHz (60 sec)). The amplitude of the current going through the loops are shown in Figure 23. The time delay in each additional step of the expansion produces a phase lag in the current amplitude:  $\Delta\phi = \Delta t/T \times 2\pi$ .

In more rigorous mathematical terms, at latitude X, the current system expands like a travelling wave:

$$I(y, t) = I_m \sin(ky - \omega t) \quad (3.6)$$

where  $\omega = 2\pi f$  is the angular frequency (f is fixed at 16.7 mHz),  $k = \frac{2\pi}{\lambda}$ ,  $\lambda = v/f$  is the wavelength of the travelling wave and v is its speed,  $I_m$  is the amplitude of the current. In Figure 24, the current  $I(y, t)$  is zero at the position  $y=0$  at time  $t=0$ .

The speed of propagation is symmetric to the east and to the west of the magnetospheric potential source. In the ionosphere and on the ground, it was chosen to vary between 1 and 10 km/sec. Rapid expansion of the substorm has indeed been proposed to occur in this speed range (see Samson, 1985 and Opgenoorth *et al.*, 1983).

The magnetic induction of the travelling current wave is integrated over the longitude Y (see Figure 24) :

$$B_H(t) = \int_y^0 B_{Hm} \sin(ky - \omega t) dy \quad (3.7)$$

where  $B_{Hm}$  is the horizontal component of the field generated by  $I_m$  ( $3 \times 10^5$  A).



The integral can be approximated numerically as follows (for small  $\Delta y$ ):

$$B_H(n\Delta t) = \sum_{j=1}^n B_{Hm} \sin(k(n-j)\Delta y - \omega n\Delta t) \Delta y_j \quad (3.8)$$

where  $n$  is the number of data points and  $\Delta t$  is the discrete time interval. This equation means that a ground station will record the sum of the magnetic fields of each current loop, phase shifted one with respect to the other.

The resulting magnetic field patterns are shown in Figure 25 for two stations located 100 km north and south of the source region. The source region is defined as the ionospheric point of incidence of FAC1 (see Figure 14), and expands to the east in this case. Each horizontal vector is computed at a time interval of  $\Delta t = \frac{\Delta x}{v}$ , where  $v$  is the speed of expansion ( $\Delta t=4$  sec and  $v=4$  km/sec). Note that at the latitude of the source  $H=0$  and the stations located north and south of the source region are  $180^\circ$  phase shifted in the  $H$  component.

The waveform generated by the current system (see Figure 26) is slightly damped in the first cycles, until the wave finds a new stationary condition, then it becomes a sinusoid. It is also interesting to note that in both components, the first cycle of the waveform has a longer period: 70 sec for the  $H$  component and 95 sec for the  $D$  component.

The best way to display this result at different geographic locations is to follow the magnetic vector over time and plot the polarization patterns.

The results are shown in Figure 27 and 28 for the following speeds of expansion (ground and ionospheric): 4 km/s and 8 km/s. The source region is denoted by the  $S$  and the arrow indicates the direction of expansion. The stations are located 100 km apart around the source.

The primary results of this model can be summarized as follows:

1. A simple oscillating current loop produces linear polarization.
2. A westward (eastward) expanding current system produces elliptical polarization, clockwise (counterclockwise) north of the current source and counterclockwise (clockwise) south. For a meridian chain of stations, the sense of polarization is reversed across a minimum in the H component (from cw to ccw when the expansion is westward or from ccw to cw when the expansion is eastward). Therefore the minimum in the power spectrum of the H component computed at each stations should give us the approximate latitude of the source region, when it is associated with a reversal of polarization (see also Watanabe *et al.*, 1978) .

A maximum in the H-D power will also indicate that the station is close to the source region (see Figure 18).

3. If, the source expands towards the station, the ellipticity is increased (the ratio of the minor axis to the major axis as defined in Chapter 2) ie. the ellipse is fat. If, the system expands away from the station, the polarization ellipse is more linear.
4. A sign change in the rotation angle of the ellipse takes place when crossing the latitude of the source region ( $H=0$ ) and its longitude ( $D=0$ ). This will have to be compared with more caution with the experimental work because of our simplified circular current loop model; In the environment of the ionosphere, complicated closure configurations could distort considerably the main axis of oscillation.
5. When the speed of the expanding system is increased, the wave stabilizes more quickly to a new stationary state, the damping characteristic decreases and the polarization ellipse is defined more clearly.

The main characteristics of this preliminary model will be compared with experimental results in Chapter 4.

A more complete model should include several other parameters, including the calculations of the potential source (emf), the inductance, and the capacitance, the calculation of a damping factor due to the dissipative Pedersen currents and the derivation of a characteristic time constant for the magnetosphere-ionosphere system to reach another equilibrium state. The present model also assumes that the magnetospheric potential source remains in a localized region of the midnight equatorial plane. Due to the non-steady nature of the solar wind-magnetosphere interaction, one might expect the source region itself to move, in which case more than one spectral peak would be observed on the ground. Let us say immediately that a current model, even more sophisticated than the one presented in this study, is insufficient to explain Pi2, because if Pi2 is simply a small scale electrojet oscillation, then one would not expect to observe such a distinctive radar signature between Pi2 and the electrojet activity in general (see Figure 7).

We believe that the FAC's (as examined in the circuit analogy above) can be associated with a strong shear mode of oscillation in and above the ionosphere.

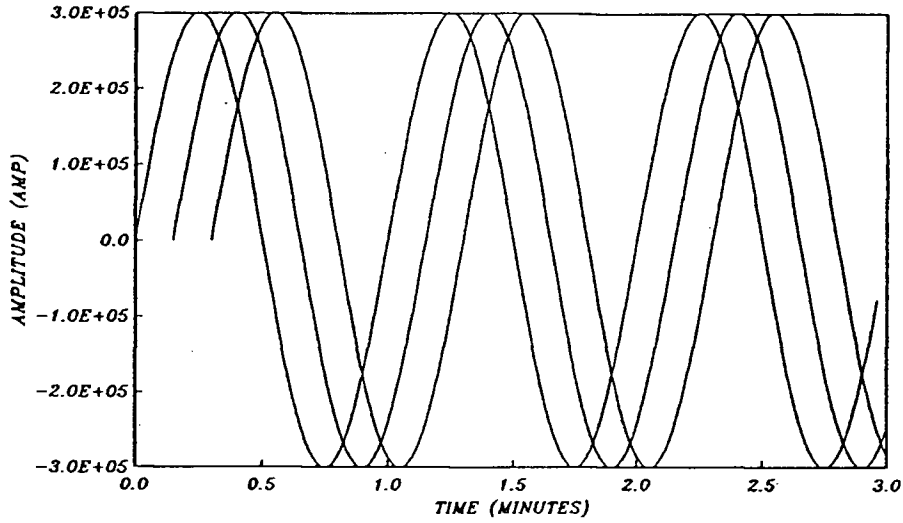


**Figure 23.** Amplitude of the phase shifted currents flowing through the loops. The phase shift comes from the time delay in each additional step of the expansion:  $\Delta\phi = \Delta t/T \times 2\pi$ .

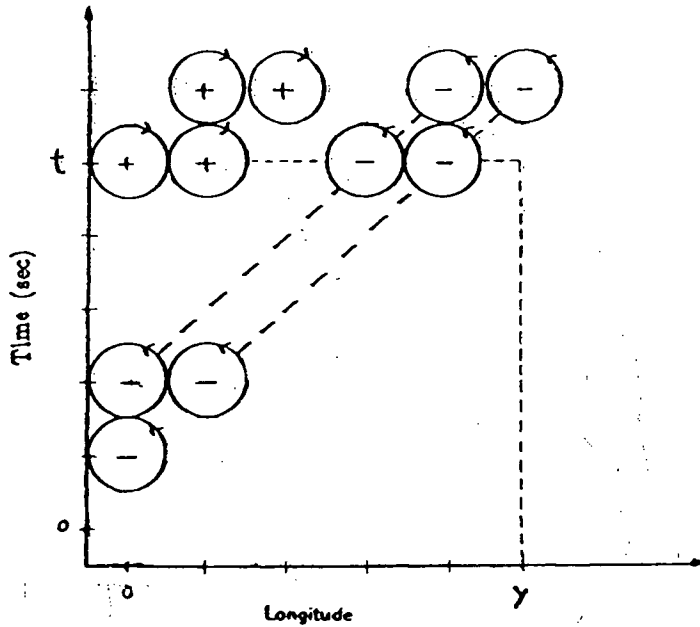


**Figure 24.** The Hall current network expands like a travelling wave:  $I(y, t) = I_m \sin(ky - \omega t)$ , the magnetic effects of which we want to integrate over the longitude  $y$ .  $I_m$  is the amplitude  $3 \times 10^5 \text{ A}$ ,  $\omega = 2\pi/f$  is angular frequency ( $f$  is kept fixed at 16.7 mHz),  $k = 2\pi/\lambda$ ,  $\lambda = v/f$  is the wavelength of the expanding wave, and  $v$  its speed.

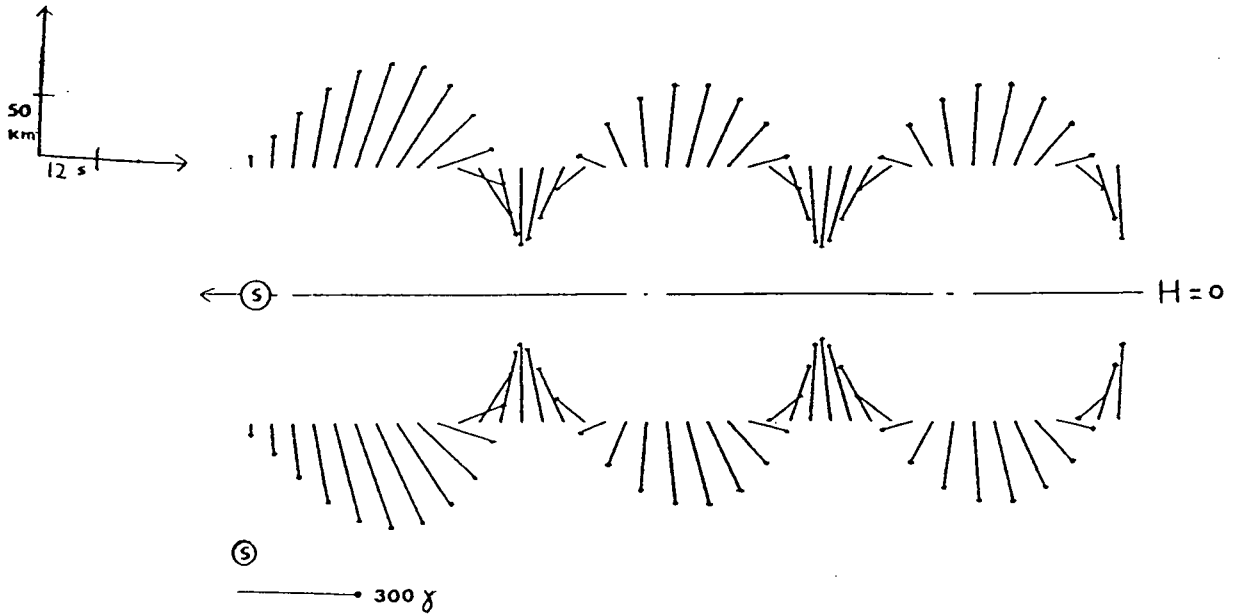


**Figure 25.** Horizontal ground magnetic vector:

$B_H(n\Delta t) = \sum_{j=1}^n B_{Hm} \sin(k(n-j)\Delta y - \omega n\Delta t) \Delta y_j$ . Each vector is plotted in the H-D plane (assuming a flat earth) at a time interval of 4 sec. The two stations are located 100 km north and south of the source region (S). The wave expands westward:  $v=4$  km/sec,  $f=16.7$  mHz,  $H=0$  at the latitude of the source.

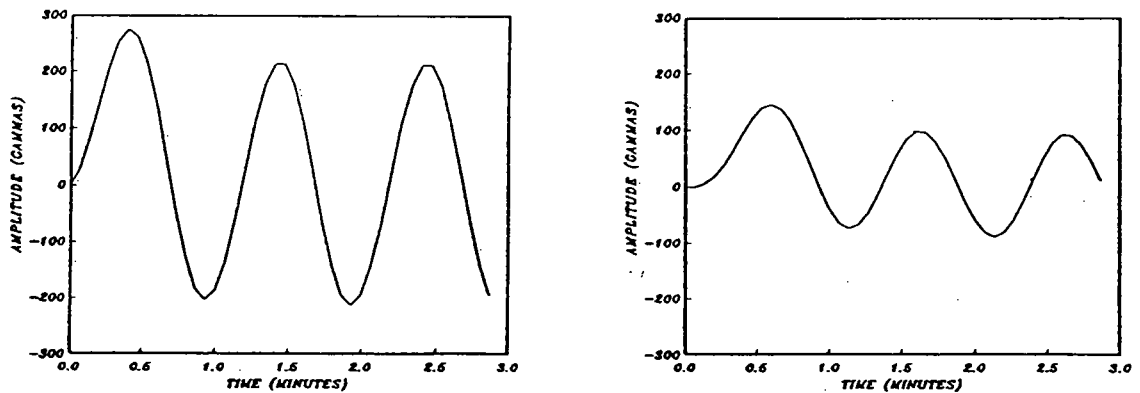


**Figure 26.** Waveform of magnetic vectors shown in Figure 25. Left: H component. Right: D component.

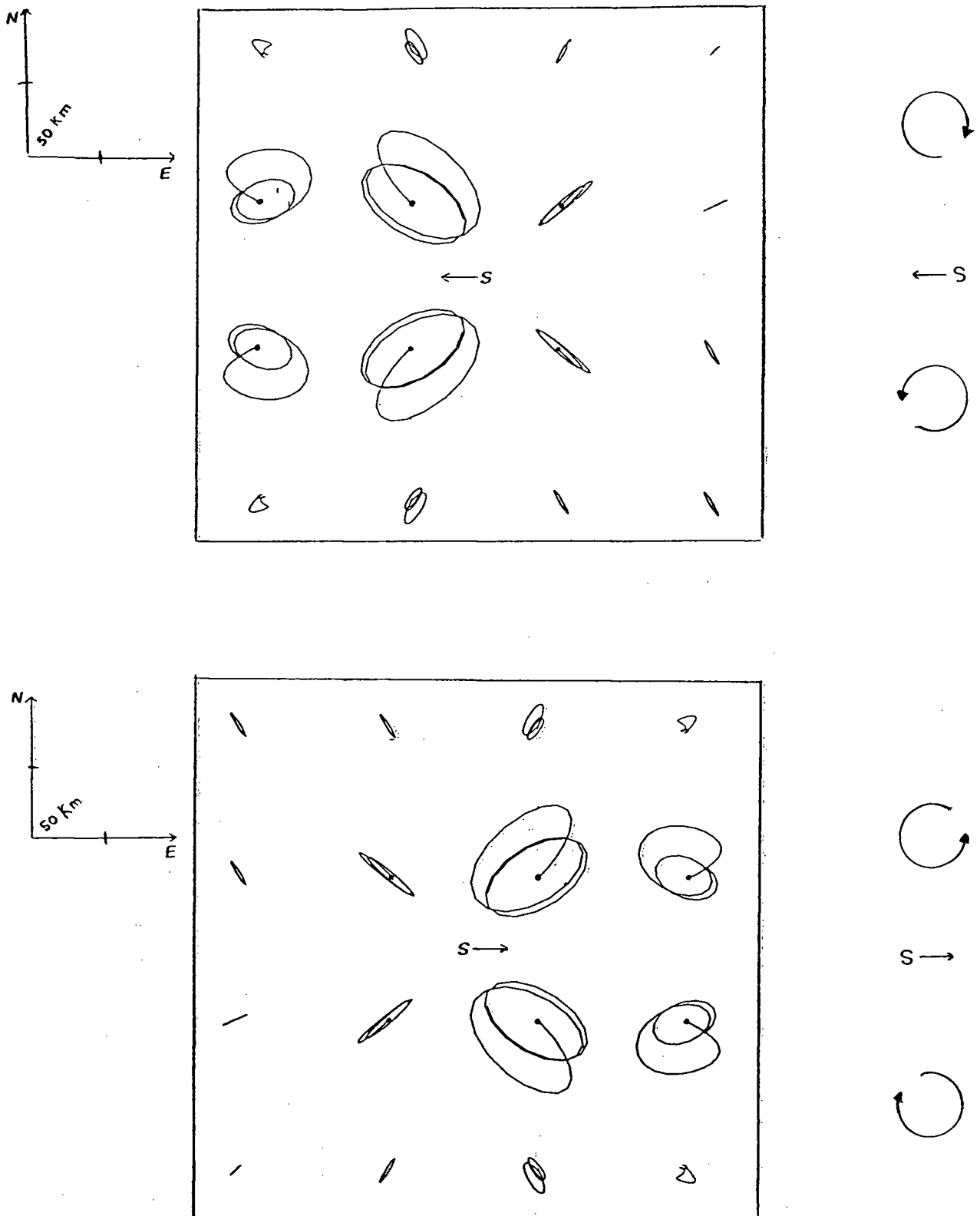


**Figure 27.** Top: Polarization patterns predicted for stations located symmetrically around the source region (S). The arrow indicates the direction of expansion (westward in this case),  $v=4\text{km/sec}$ ,  $f=16.7\text{mHz}$ . The dot indicates the initial position ( $t=0$ ). The sense of polarization is schematically indicated on the right of each Figure. Bottom: same as Top but the expansion is eastward.

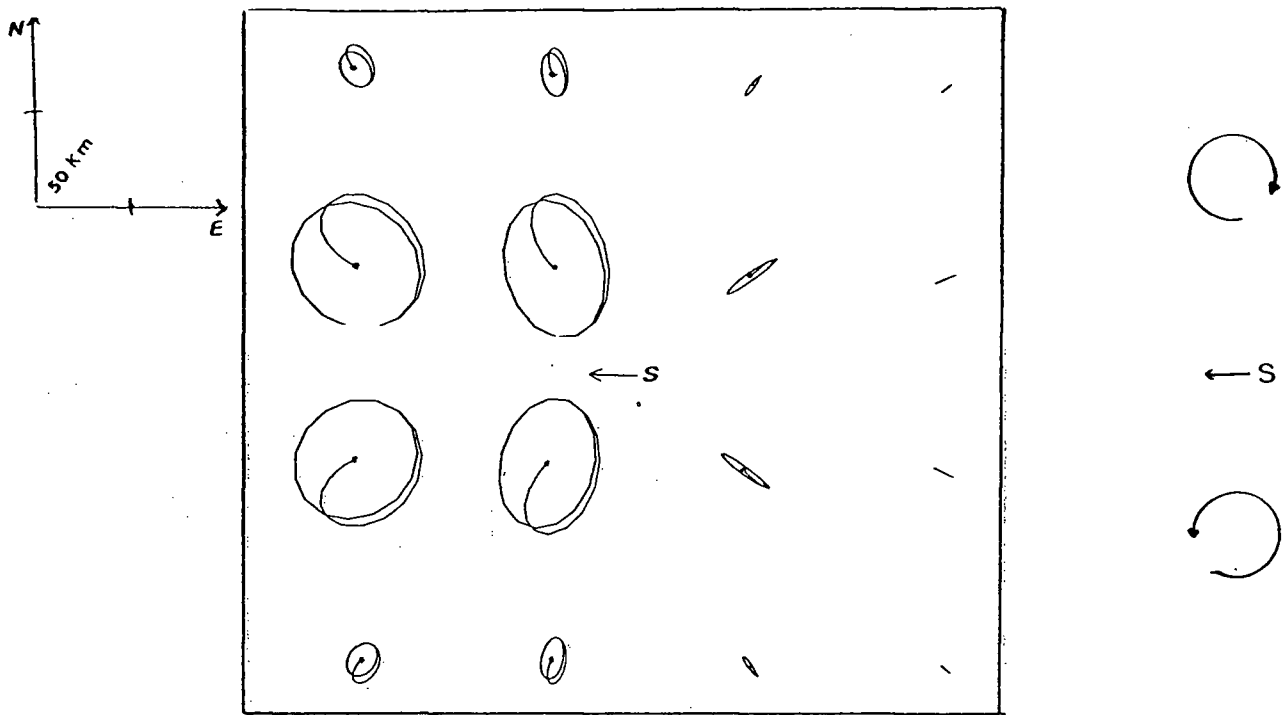


**Figure 28.** Same as Figure 27 but the speed is increased to 8km/sec.

### 3.2 The hydromagnetic wave or, possibly, the 'FAC shear mode'

This point of view considers the transfer of energy from particles to hydromagnetic waves through a variety of plasma instabilities.

If Pi2 is a shear Alfvén mode, the source region is either the ionosphere or the magnetosphere.

Some of the most interesting theories are briefly described in the following sections.

Perhaps, the still most widely accepted of the generation theories is that put forward by Rostoker (1967), in which Pi2 is initiated when oppositely directed field lines reconnect impulsively across the neutral sheet in the tail of the magnetosphere (Atkinson, 1966; Piddington, 1967). The resulting release of energy causes a stream of energetic particles to 'catapult' on the closed magnetosphere, causing the field lines which form

the outer boundary of this region to oscillate in the torsional mode and thus to generate a Pi2. The oscillations couple to the auroral ionosphere which then acts as a secondary generator from which the signal propagates to other sites. The energetic particles after their impact with the closed magnetosphere, precipitate in the auroral zone, where they cause an auroral break-up and a magnetic bay. As the recombined field lines are added to the closed magnetosphere, they form a bulge in it, so that the precipitating particles are incident on the ionosphere further towards the poles as the break-up progresses. As more field lines reconnection takes place, additional Pi2's are generated. Since the auroral zone is located further north, the new Pi2's have longer periods (which can be verified in the data analysis).

Saito and Matsushita (1968) have suggested that when the stream of energetic particles hits the closed magnetosphere, the magnetospheric cavity rings in a combination of poloidal and toroidal modes which they consider can be approximated by the poloidal mode alone. They interpret the resulting signal as containing only one period, equal to the time taken by the modified Alfvén wave to travel from the outer boundary of the closed magnetosphere to the earth and back again.

Some other researchers (Fukunishi, 1975; Lanzerotti, 1974) have suggested that the particle energy can be coupled into field line(s) where there is a sharp discontinuity in the thermal plasma density, such as the plasmapause, located between 55° north and 61° north. If this is the case, then the maximum power of Pi2 is achieved at this latitude. This can be quite easily checked with the observations.

The plasmapause is not the only candidate source region. A sharp decrease in the ambient magnetic field as one crosses the earthward region of the ring current might well provide conditions necessary for coupling of waves as proposed by Samson and Rostoker (1980a).



All these theories suggest that the Pi2 Alfvén wave is generated in the magnetosphere. From a ground observational point of view, if the high conductivity of the ionosphere acts to reduce the electric field of HM waves ( $R=0.8-0.9$  for a uniform ionosphere, referred in Chapter 1), then most of the energy of incoming waves having a wavelength greater than the ionospheric duct (which is the case for Pi2) is reflected back to the magnetosphere. As discussed in Chapter 1, a weak Hall current associated with the electric field of the wave is generated in the ionosphere. Since the Pi2 is associated with the expansion phase of the substorm during which FAC's are observed in the entire disturbed sector, there is strong reason to believe that the Hall current induced by the electric field of the wave are masked by the Hall current arising from the FAC's.

these theories predict linear polarization on the ground : the induced Hall current is spatially invariant in the ionosphere.

It has also been suggested that HM waves could be generated in the ionospheric auroral arcs, which are associated with sudden changes of ionospheric conductivity; they are subsequently reflected between both hemispheres. In the presence of a westward external (primary) electric field the following process is believed to take place: at the time of the auroral break-up, the ionospheric conductivity is suddenly enhanced (by electron precipitations); the excess current flowing in the region brings positive and negative charges to the western and eastern edges of the enhanced conducting strip respectively; consequently, an opposing electric field is created, which drives return currents and weakens the external electric field in the region. This electric impulse, close in magnitude to the undisturbed ionospheric electric field but in the opposite direction could generate a shear Alfvén mode. This possible mechanism has been studied by many scientists (Wescott *et al.*, 1969; Haerendel, 1970; Heppner, 1972; Maltsev, 1974 ), and can also be described in terms of motion of magnetic field lines as follows:

The electric convection field makes the magnetic field lines move towards the earth in the midnight sector of the magnetosphere (Heppner,1972), a sudden enhancement of conductivity leads to a sudden stop of the magnetic field ends crossing that region. The magnetospheric parts of these field lines will continue to move by inertia until the stop signal reaches them. As a result, a resonant oscillation will arise.

All these theories assess that the coupling between the electric field of the magnetosphere and the ionosphere could generate the Pi2 HM wave, the source region being the ionosphere.

None of these generation theories are complete yet. What is clear is that sudden conductivity enhancement are associated with auroral arcs, the dynamic development of which can be examined in Figure 29. Satellite photographs show that these arcs expand rapidly to the west and form a 'westward traveling surge' at an estimated speed of 1-2 km/sec.

We believe that, if the FAC is the main feature during the brightening of the aurora (upward FAC is the carrier of precipitating electrons), then the electric impulse described above in simple words could set into motion the FAC which remains 'frozen-in' the westward travelling surge' and subsequently oscillates back. The induced Hall currents would be the only observed ground magnetic effects.

From an observational point of view, this initial impulse can be simulated on the computer by calculating the ground magnetic effects of a Hall current loop moving at the speed of the 'westward traveling surge' (assuming that it oscillates back at the same speed (see Figure 30)). A figure of eight polarization characteristic is expected as shown in Figure 31. Of course, in reality, non uniform speeds are expected and therefore, very disturbed polarization patterns.

This model of polarization can only be verified experimentally using the dynamic approach, which consists in plotting the tip of the magnetic vector in the H-D plane (without previously applying a narrow band pass filter). Since Kp index was high (see Appendix E), the events were noisy and disturbed. This model will therefore be more difficult to verify. However, for further work, the Physics of Figure 30 should be further investigated and possibly verified mathematically as an appropriate boundary condition which satisfies the MHD equations.

In this Chapter, we have considered the electric coupling between the ionosphere and the magnetosphere in two possible ways; in the first case, the generation region of Pi2 lies in the magnetosphere equatorial plane, and Pi2 develops as LC oscillations of the 3-D current system; in the second case, Pi2 is generated in the ionosphere by an initial electric impulse imparted to a FAC under the conditions of brightening of Aurora. In the next Chapter, we will test the different ideas and models presented in this Chapter.

# Implosion in the Magnetotail

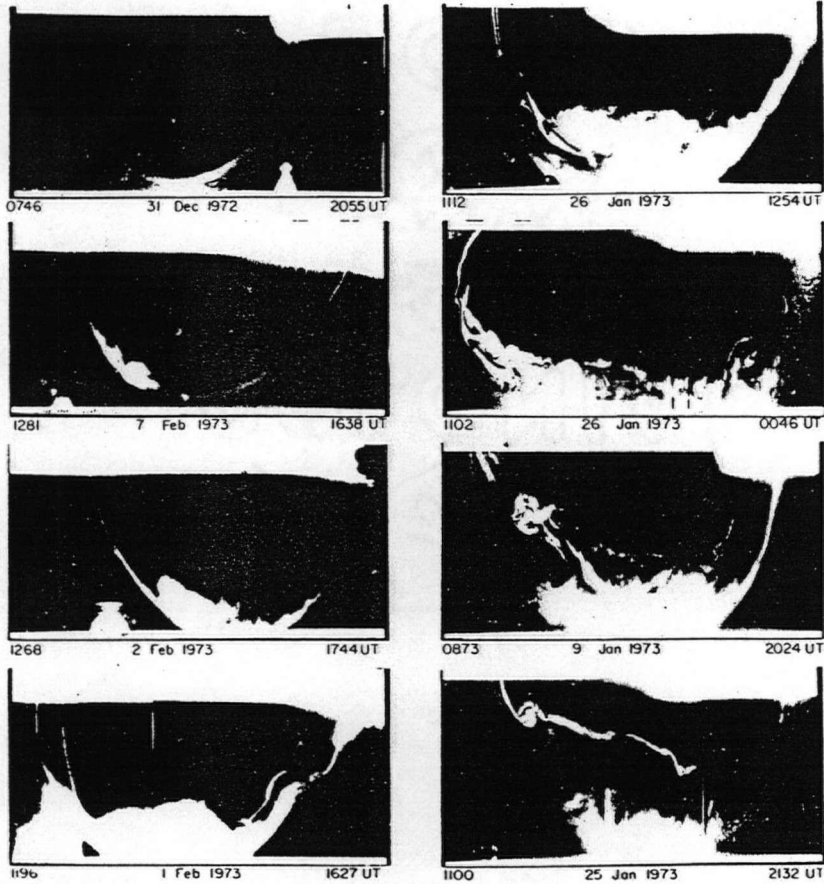
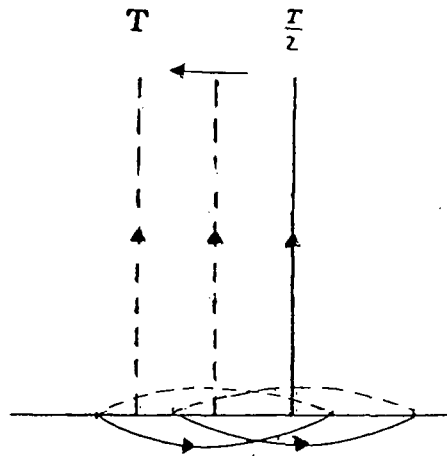


**Figure 29.** Development of the aurora during the expansion phase. The midnight meridian is toward the bottom center of each panel (Akasofu, 1975).



$T$  = period of oscillation

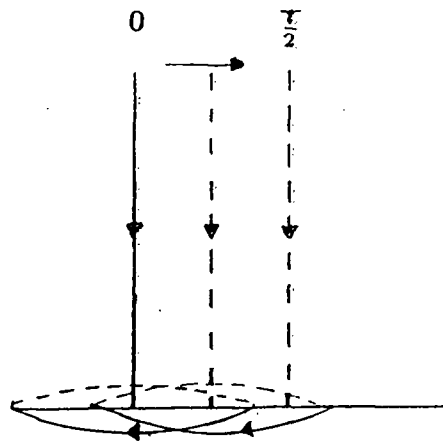


**Figure 30.** What is believed to be the initial ionospheric electric impulse imparted to a field-aligned current under the conditions of brightening of aurora. Travelling surge speed is 2 km/sec.  $T=60$  sec. The Hall current is the magnetic field observed on the ground.

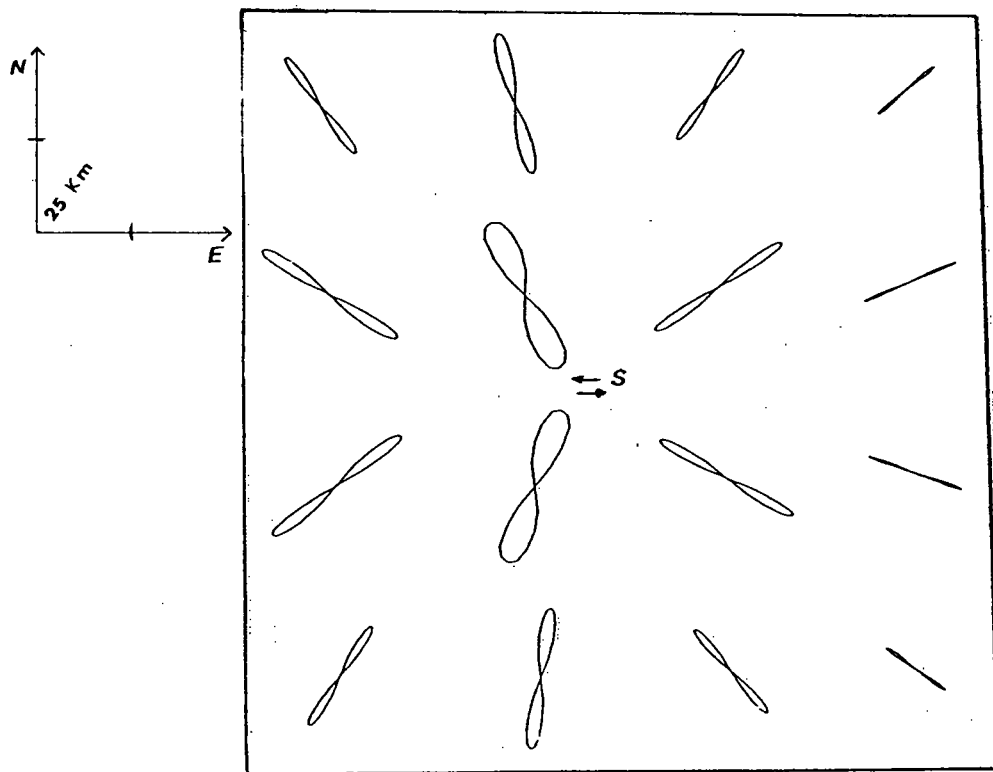


**Figure 31.** Resulting polarization patterns produced by the Hall current shown in Figure 30. Source region is denoted by S.

## Chapter 4

As mentioned in Chapter 2, two basic set of events were analyzed, one in the morning sector, the other in the evening sector. Different aspects will be considered in this experimental analysis: the association of Pi2 with magnetic substorm in general, the frequency content of the wave versus latitude, and the polarization results which will be compared with the theoretical expectations from the model presented in Chapter 3. In the interpretation of the results, we will have to be careful not to generalize from special cases.

### 4.1 Pi2 and substorm

In the early morning sector, the association between Pi2 and the substorm is easier to analyze because the 'negative bay' is characteristic at all stations. It is difficult by looking at the magnetogram alone to decide when precisely the micropulsation activity starts, some subjective decision has to be made. What is clear, however, is that the Pi2 is associated with the early stage of the expansion phase as can be seen in Figure 1. Figure 32 displays the three components of the magnetic field variations H, D, Z (positive being defined as north, east and down respectively). The onset of the 'negative bay' appears in multiple steps: onset A is first seen at Park Site at 7.13 (U.T), onset B is seen at Christopher Lake, La Ronge and Southend at 7.21'.20" (U.T) although the change in the background magnetic field in the H component is sharper at Christopher Lake than at the other two stations. Onset C is finely seen simultaneously at South End and La Ronge at 7.28 (U.T). Pi2 activity is associated with at least two of these onsets. The possible events after 7.28' were so complex that a latitude comparison was not possible. An important fact to note is that eventhough the expansion phase of the substorm has not started at South End and La Ronge at 7.13' (U.T), Pi2 is observed at

these stations concurrently with Park Site. In Figure 1, a very weak Pi2 micropulsation can be seen before the onset time 7.21'20". This tells us that the transmission of Pi2 energy in latitude is different from that of the substorm.

It is first important to understand the background substorm electrojet over which the Pi2 develops. For that purpose, a latitude profile of the three components of the magnetic field is plotted every two minutes in Figure 33 from 7.13' to 7.29' U.T ( the Pi2 time interval selection). A reference level before the substorm onset is chosen and the deflection in all three components H, D, Z components are measured in gammas. Figure 33 should be analyzed together with Figure 32.

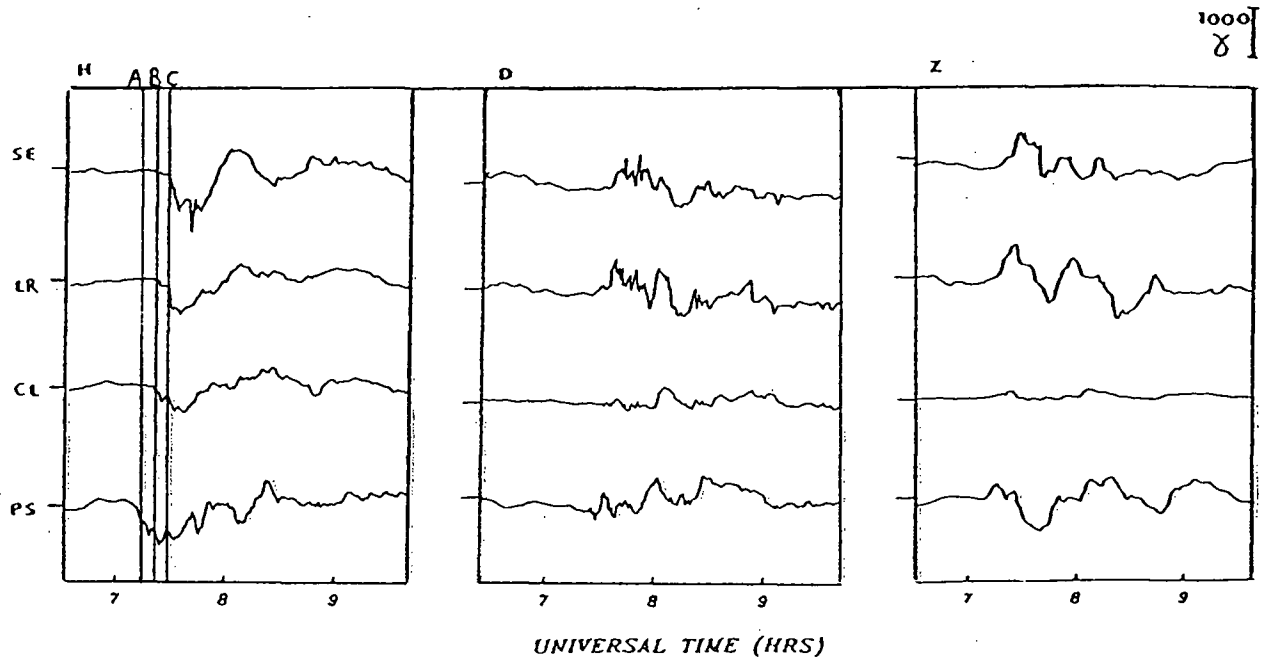
The Z component is indicative of the center of electrojet: a positive bay ( Z being positive in the direction of the field) means that the magnetic field is increased, the observing station being located to the north of the center of the westward electrojet. At 7.28, the Z component becomes negative at Park Site which means that the center of electrojet has just gone overhead. At Christopher Lake the Z component shows very small fluctuations around 0. It seems at first that the station is the center of activity throughout the substorm. But this is not consistent with the fact that we have multiple onsets shifted from the south to the north in the H component and secondly that La Ronge and South End show negative bays in the Z component after 7.42', which means that the center of electrojet has gone overhead. What is intriguing is that Christopher Lake does not show the same morphological characteristics as the other stations in the Z component. It might be that some higher ground conductivity has the effect of suppressing the vertical component of the magnetic field.

The D component indicates the tilt in the westward electrojet (assuming that ionospheric currents only determine the D behaviour), a positive bay meaning that the electrojet is tilted in NE-SW direction (a negative bay SE-NW). The behaviour in the D component



should therefore give us some information on the conductivity of the ionosphere. If the conductivity is uniform over a certain period of time, the current should flow in that region in the same direction and therefore the latitude profile should be stable. The D component is fairly stable at all stations until 7.28', except at Park Site which shows variations of -200 gammas between 7.23' and 7.25' and +280 gammas between 7.25' and 7.29'. Such rapid changes in the 'tilt' of the electrojet suggest that the ionosphere is susceptible to enhance considerable 'noise' in a wide range of frequencies; this means that if the Pi2 develops on top of the electrojet as a small scale feature, the result of an averaging technique (polarization and spectral analysis) will have to be regarded with caution because mixing of Pi2, electrojet and fac's will most likely take place. From 7.13' to 7.28', Park Site is the station the closest to the center of electrojet (see H and Z component). It might be surprising at first to observe that the break-up region is located that far south. It has been suggested in the literature that there is a correlation between the geomagnetic activity index and the break-up latitude. Rostoker (1967a) mentions that a combination of auroral activity and magnetic storm activity governs the latitudinal position of the auroral electrojet. Akasofu (1964b) has shown that as the index of planetary magnetic activity increases one would expect the auroral break-up to be initiated at lower latitudes.

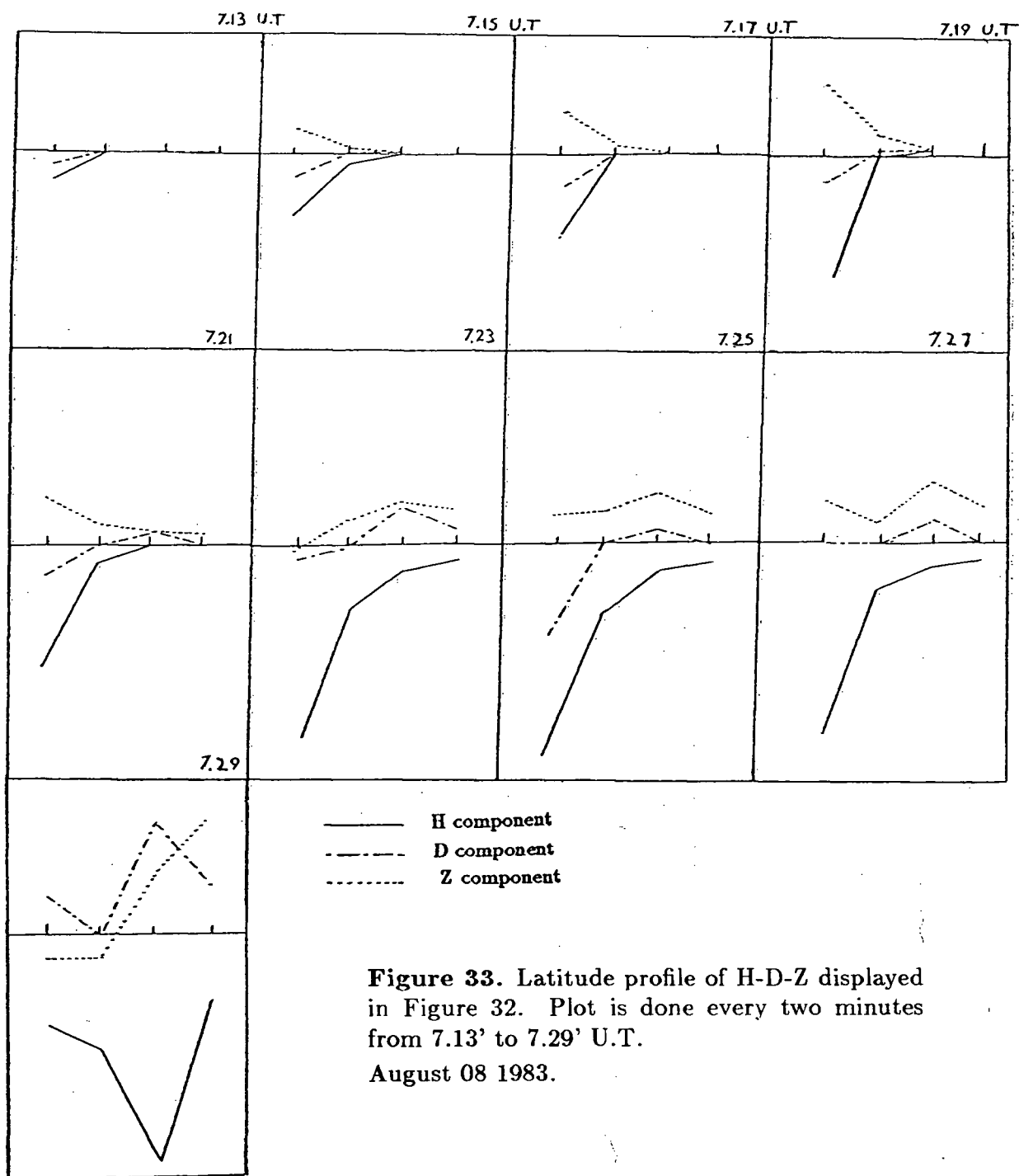
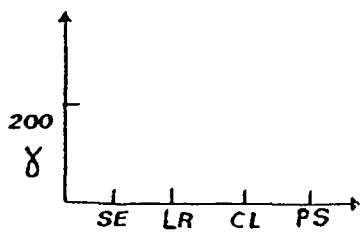
It is generally accepted now that the substorm phases occur in multiple steps, the center of the electrojet being shifted progressively to the northwest (Wiens and Rostoker, 1975). This is verified by the multiple onset of the negative bay in the H component, starting first at Park Site and progressing to South End. To investigate whether the Pi2 source region and the substorm source region are the same, the normalized power versus latitude can easily be computed and compared for the substorm electrojet and for the Pi2 central frequency. The main substorm electrojet power can be identified quite safely



**Figure 32.** Magnetograms from South End (SE), La Ronge (LR), Christopher Lake (CL) and Park Site (PS). Integrated from induction magnetometer with a three-hour time integration constant.

August 08 1983.

as the maximum peak in the lower frequency end of the spectrum (see Figure 10). Its main range varies between  $\sim 0.1$  mHz to  $\sim 5$  mHz (although it can also enhance power in the higher frequency part of the spectrum). Visual inspection of the magnetogram is, so far, the best way to differentiate the Pi2 from the general substorm. In Figure 1<sub>a</sub> and 1<sub>c</sub>, the substorm waveform lasts  $\sim$  one hour. In Figure 1<sub>b</sub> and 1<sub>d</sub>, the Pi2 waveform is riding on top of large oscillations lasting between  $\sim 3 - 8$  minutes; and there is definitely no Pi2 characteristic in these long waveforms. The results of this analysis are shown in Figure 34: The power maxima and minima do not correspond in all 5 cases. In the evening sector, the maximum in the Pi2 power has been shifted clearly from Park Site (3.08'-3.15'event) to La Ronge (3.16'-3.23') even though the substorm electrojet peak remains at Park Site. It is interesting to note that the northward shift of the Pi2 peak



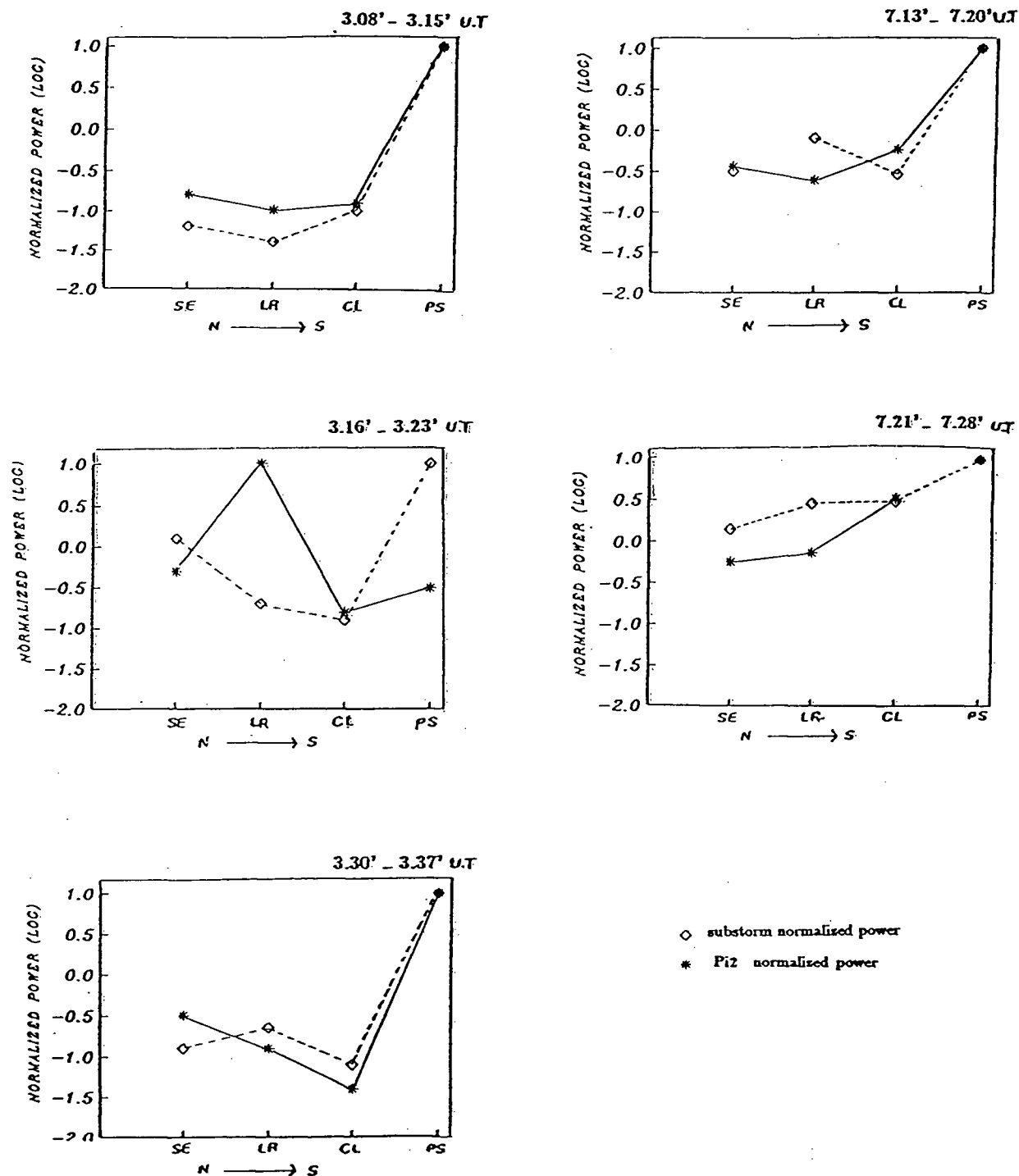


**Figure 34.** The electrojet normalized power (defined in text) compared to the Pi2 normalized power (the dominant frequency shown in Figure 34) as a function of latitude.

South End (SE), La Ronge (LR), Christopher Lake (CL), Park Site (PS). August 08 1983.

is associated with a change in the central frequency of the dominant peak (from 20 mHz at Park Site to 13 mHz at La Ronge). This point will be discussed later. In the morning sector, the minima in the Pi2 and the substorm normalized power do not correspond between 7.21' and 7.28'. If the power maxima and minima are indicative of the latitude of the source region, then, this result suggests that the Pi2 and the substorm source regions are not the same. This will have to be confirmed with other observations.

## 4.2 Pi2 frequency shifts

The frequency content of the events under study is displayed in Figure 35. Let us remember that the 25-30 mHz peak was the only power detected by our polarization filter (Chapter 2); Whether this peak is harmonically related to the Pi2 dominant frequency (15-20 mHz), or arises from a different source mechanism will be discussed in the next section. Figure 35 shows the spectral content of the H and D components, as well as the frequency shifts versus latitude in the five events under study. The maximum entropy method was used to analyze with high resolution the spectral content of Pi2 (same parameters as in Chapter 2, Fig. 1<sub>b</sub>).

In Figure 35, the circled peaks (H and D) represent the selected Pi2 band power. They were identified according to the three following criteria:

1. Visual inspection of the magnetograms.
2. Latitude comparison: isolated peaks observed only at one station were eliminated.
3. Peak 'correlation' of the H and D components as found in the trace of the spectral matrix ( defined in Chapter 2 ) : the 'correlated' power is indicated by the location of the dashed line at the observing station.

The difference in the spectral content between the three components of the magnetic field seems to be avoided in the literature. But, if we look at Figure 35 very rarely

the H and D components show the same central frequency. This was also observed by Kato and Watanabe, 1957. It is particularly clear in the morning sector (7.21'-7.28' U.T.). The problem is that the polarization techniques generally used are based on the cross-power spectrum between the different components at the same frequency, it might actually be better to correlate the shifted frequencies. In the present work, we do not attempt to solve this problem, we apply the classical polarization analysis as found in Born and Wolf, 1975, p. 24-29.

The frequency shift versus latitude is easier to discuss, and is mentioned more widely in the literature (Olson and Rostoker, 1976; Sutcliffe, 1976). If Pi2 is a resonant field line oscillation which couples to other sites through the ionospheric Hall current as was discussed in Chapter 1 and 3, then one would not expect a frequency shift versus latitude i.e. we would not expect the lower latitude stations to have a higher frequency content than the higher latitude stations. No such frequency shifts are observed in four events out of five.

But if Pi2 is a field line resonance coupled to higher or lower latitude regions by a mechanism other than the Hall current, then one would expect a dominant lower frequency content of the higher latitude stations. This is only verified in the 7.13'- 7.20' (U.T) event: Park Site has a dominant frequency centered at 20 mHz, the other three stations at 15 mHz.

There are two possibilities: Park Site might have observed a completely different event (we have to remember that the morning sector Pi2's are associated with multiple onsets of 'negative bays' as shown in Figure 32); or Park Site, being at the latitude of the plasmopause, might be the source region as proposed by Fukunishi (1975) and Lanzerotti (1974). In the evening sector (3.30'-3.37' U.T), the opposite situation takes place:

the higher latitude station (S.E) has a higher frequency content than the other three stations.

No conclusions can be drawn at the moment: theoretical investigations combined with a detailed study of the spectral content of world-wide Pi2 events will be necessary before the mechanism by which the Pi2 energy is diffused to higher and lower latitudes is understood.

The shift of the source region to the north as successive Pi2's are generated is predicted by Rostoker's theory (1967). This would be observed on the ground by an increase in the period of the Pi2 micropulsation in two successive events. This is verified in the evening sector which shows a shift in frequency from 20-22 mHz (3.08'-3.15'U.T) to 14-16 mHz (3.16'-3.23'U.T). But the opposite takes place in the morning sector: a shift from a lower frequency content to a higher frequency content, from 7.13'-7.20' U.T to 7.21'-7.28' U.T. This point will have to be verified with other observational results.

The frequency content of Pi2 is also expected to vary with geomagnetic activity. Figure 36 shows a statistical analysis of the variation of Pi2 period with Kp index. According to the study of Troitskaya (1965) and Rostoker and Samson (1967a), when Kp index is close to 1, Pi2 has fundamental period close to 100 sec, as when Kp index is close to 4 and higher, the Pi2 fundamental period is raised to 60s and above. This tells us that as Kp increases, the Pi2 source region, initially, originates at lower latitudes, ie, field lines with feet in the lower latitude regions are shorter than field lines with their feet in the higher latitudes, therefore the shorter eigenperiods observed at times of strong magnetic activity originate further to the south. This is verified in our data: In the early morning sector, the Pi2 central frequency (of the dominant peak) lies at 15 mHz at Southend, La Ronge and Christopher Lake, Kp index is 6<sup>-</sup>; in the evening

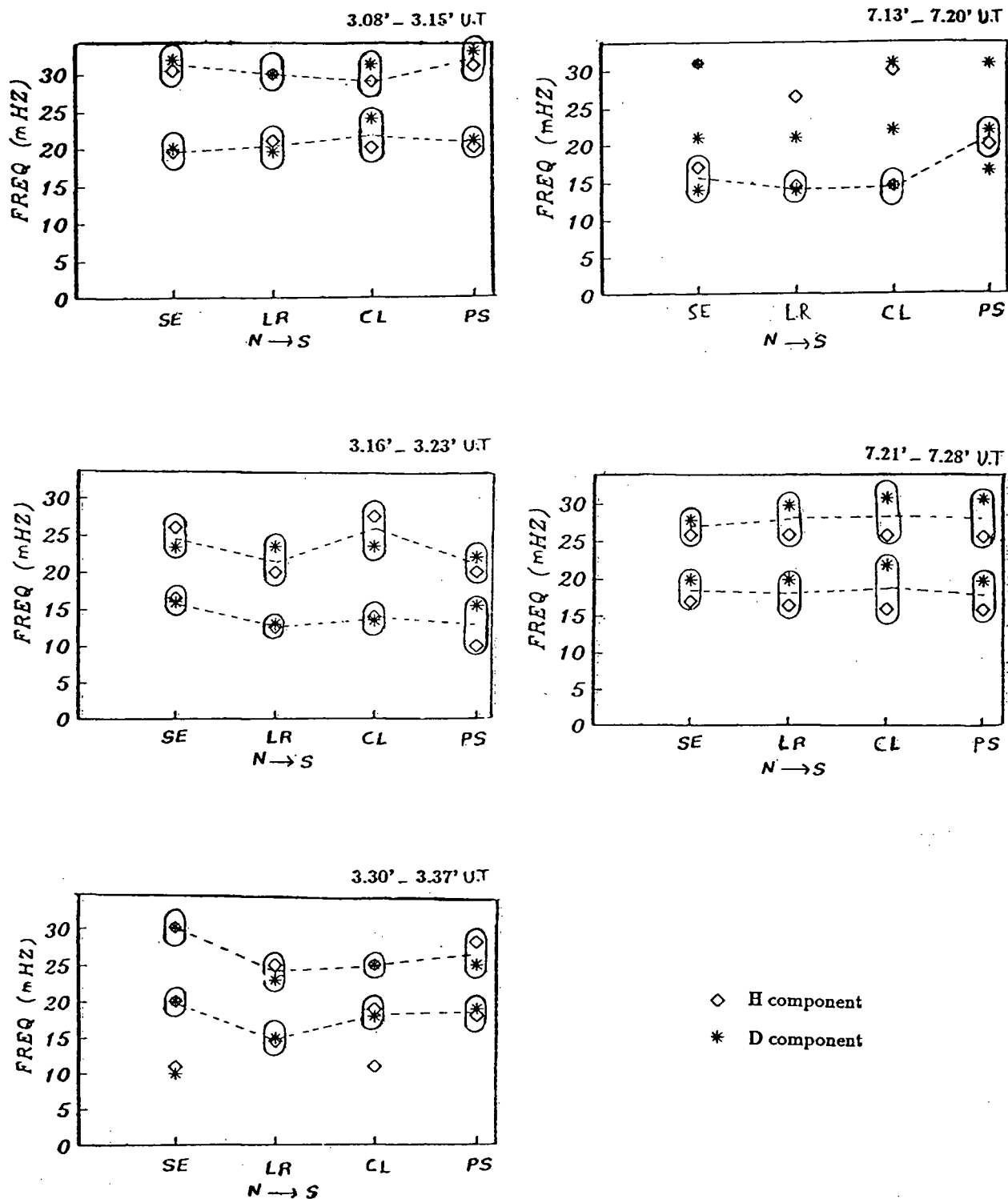


**Figure 35.** Spectral content of Pi2 versus latitude: the dominant frequency and a possible higher frequency harmonic. ◇ shows the correlated H and D power. The location of the dashed line at the observing station indicates the peak found in the trace of the spectral matrix which is the intensity of the signal (H + D).

South End (SE), La Ronge (LR), Christopher Lake (CL), Park Site (PS). August 08, 1983.





This analysis was applied to the Pi2 dominant frequency and its possible higher frequency harmonic (see Figure 35). The result will show if they are harmonically related or not.

The evening sector results are shown in Figures 37 and 38. Two pieces of information are displayed on the graph: first of all, the polarization characteristic of Pi2 averaged over the selected time interval and secondly the relative power of the H and D component with respect to the other stations (same parameters as in Chapter 2 Fig. 14<sub>a</sub>). According to our current model, the two pieces of information have to be combined in the following way: a minimum in the H component (close to  $H=0$ ) or a maximum in the H and D components should correspond to a reversal of polarization across the stations (This was proven theoretically by Chen and Hasegawa (1974) for Pc3-Pc5 micropulsations). In the first event (Figure 37), one can see that there are two discontinuities, one across La Ronge which corresponds to a minimum in power in the H component, the other at Park Site which corresponds to a maximum in the horizontal components. Both of these discontinuities are associated with a reversal of polarization (see Chen and Hasegawa, 1974). In terms of current model, this means that the current source originally located at a latitude between La Ronge and Christopher Lake, to the west of the stations expands away from the stations (the polarization becomes more linear). Park Site shows the polarization characteristic of a current source, originally located to the west and expanding towards Park Site (the polarization ellipse is fat). This result seems contradictory at first, but we have to remember that Park Site is at the latitude of the plasmopause which might be the demarcation line between two current sources, one expanding to the west north of the dividing latitude the other expanding to the east, south of the dividing latitude. So the plasmopause seems to be a possible source region of Pi2. The orientation of the main axis of polarization ellipse cannot be compared

with the current model, because, most likely, the Hall current closure system is more complicated than a circular loop. Within the error estimate established in Chapter 2, the 30-32 mHz possible harmonic shows the same phase and power characteristics as the dominant frequency, the main difference in the two spectral peaks is in the % polarization, as shown in Figure 13. It might well be that the main power originates from the initial Pi2 impulse and the higher frequency component from the partial ionospheric reflections at both hemispheres.

The second event shows a central frequency at 15 mHz (dominant peak). As mentioned earlier, longer periods suggest that the Pi2 source region is shifted to the north. The polarization results are shown in Figure 38. The maximum has moved to La Ronge, with ccw polarization north and cw polarization south of the discontinuity, the same polarization characteristics were seen in the preceding event across Park Site. The minimum in the H component at Christopher Lake is not associated with a reversal of polarization probably because the station is far away from the current source. The 22-26 mHz power shows the same polarization characteristics as the dominant frequency within the error estimate defined in Chapter two except at La Ronge which shows a reversal of polarization. A diagram summarizes the results of these two consecutive events(see Figure 39).

Figure 40 (top) shows the results of the third event (3.30'-3.37' U.T). The same characteristic in power and polarization as event 1 (3.08'-3.15'U.T), except at Park Site which shows more linear polarization, this suggests that the current source is originally to the east of Park Site, and expands away from the station. Regarding the same event, we found that the power of the higher frequency harmonic (25-30 mHz) was  $\approx 38$  DB down from the maximum, and following the error criteria established in Chapter 2, we did not compute the polarization parameters for that peak.

There are two facts which suggests that Pi2 source region moves to the north in the evening sector: The frequency shift from event 1 to event 2, and the polarization characteristics: the maximum in power is shifted to the north with consistent changes of polarization from the first event to the second.

The result of the early morning sector (Figure 40-bottom) is quite clear at least for the 7.13'-7.21'20" event and has to be compared with the first event of the evening sector: all the polarization senses are reversed, meaning according to our current model that the system is expanding to the east. The symmetry in the Pi2 polarization properties between the evening sector and the morning sector is an interesting result.

The second event (7.21'-7.28'U.T, shown in Figure 41-top) has two basic problems, the first being the wide frequency shifts observed from the H component to the D component (3-5mHz), the second being the dangerous possibility of analyzing mixed events. The polarization results are therefore more suspicious, at least at Christopher Lake and Park Site. South End and La Ronge do not show any polarization changes from the preceding event, the minimum power in the H component is however shifted from La Ronge to South End, which again suggests that the Pi2 source region has been shifted to the north.

The second model presented in Chapter 3 is more difficult to verify experimentally because it cannot be computed, it has to be observe directly from the data: the best examples found are shown in Figure 41 (bottom). A mixture of elliptical polarization, figure of eight polarization and overall confusion is apparent. This example is the dynamic equivalent of the computed average shown above (both the orientation and ellipticity are in good agreement). To verify experimentally this theoretical model, it is proposed that events occuring during quieter geomagnetic times be analyzed.

It is also interesting to note that in all the Pi2 events under study (20 events), we found only two cases of linear polarization. This suggests that a strong toroidal field is not only taking place in the magnetosphere, but also in the ionosphere. This is well suggested by Figure 41. These interesting experimental results will be discussed in the following conclusion along with suggestions for further work.

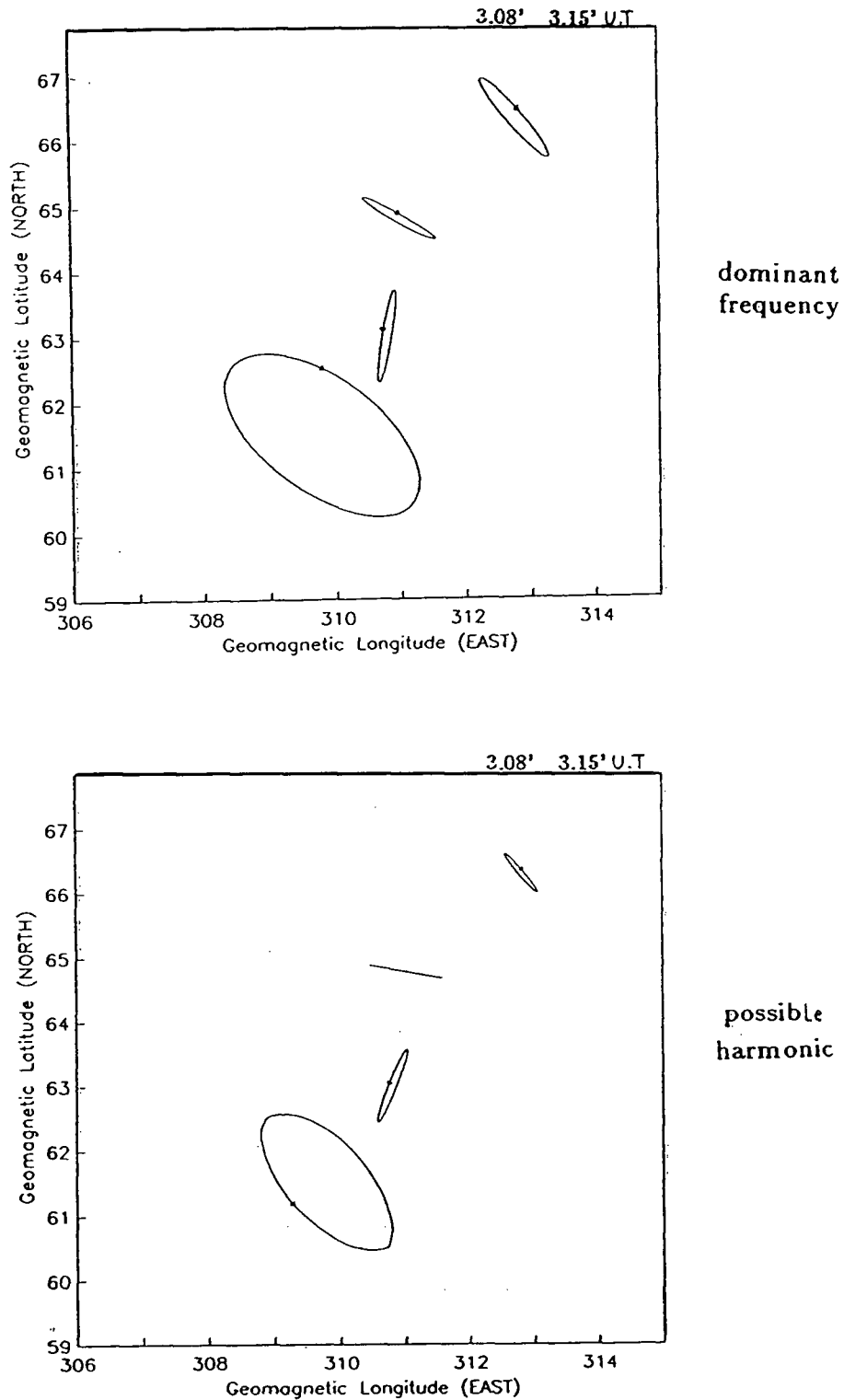


**Figure 37.** Polarization characteristics of Pi2 dominant peak(top) and possible harmonic(bottom) averaged over the time interval (Refer to Figure 35 for frequency information). The computation is done in the frequency domain and is normalized to the maximum power in the H and D components (measured in units of  $(nT)^2/Hz$ ). Top:  $H_{max} = 3.7(\log_{10})$ ,  $D_{max} = 3.4(\log_{10})$ . This computation was done for the spectral peaks shown in Figure 34. bottom:  $H_{max} = 2.9(\log_{10})$  and  $D_{max} = 2.75(\log_{10})$ .

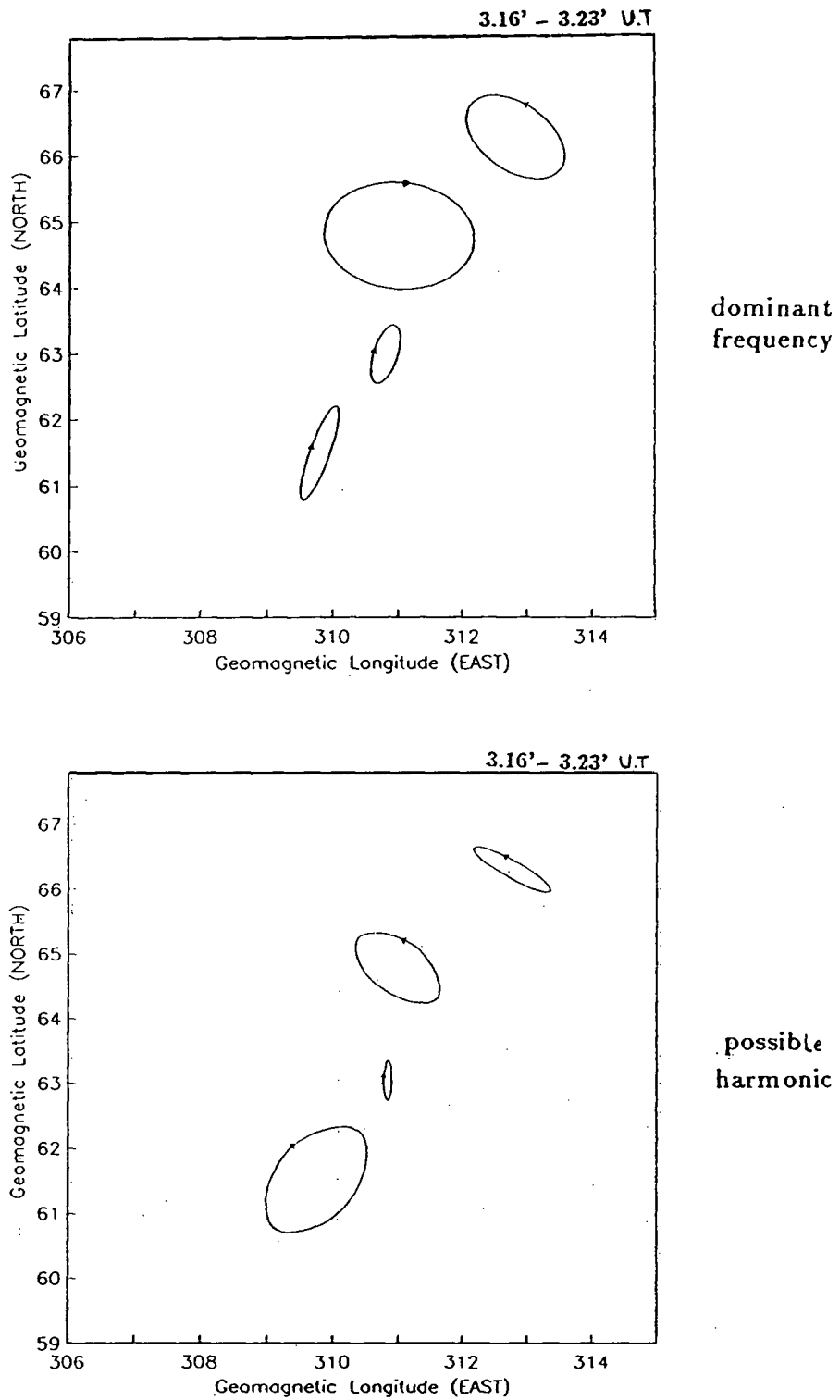


**Figure 38.** Same as Figure 37. Top:  $H_{max} = 3.5(\log_{10})$  and  $D_{max} = 3.9(\log_{10})$ . Bottom:  $H_{max} = 3.1(\log_{10})$  and  $D_{max} = 3.1(\log_{10})$ .

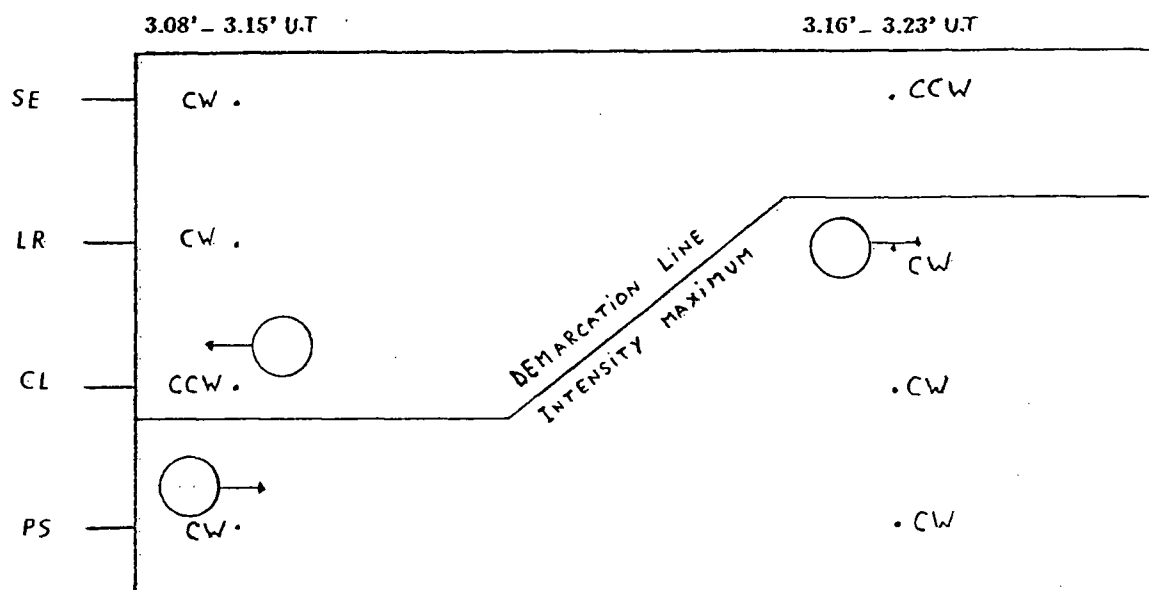


**Figure 39.** Summary of polarization results. The two successive events (left and right) show similar polarization characteristics shifted northward. The demarcation line is shifted northward in these two successive events.



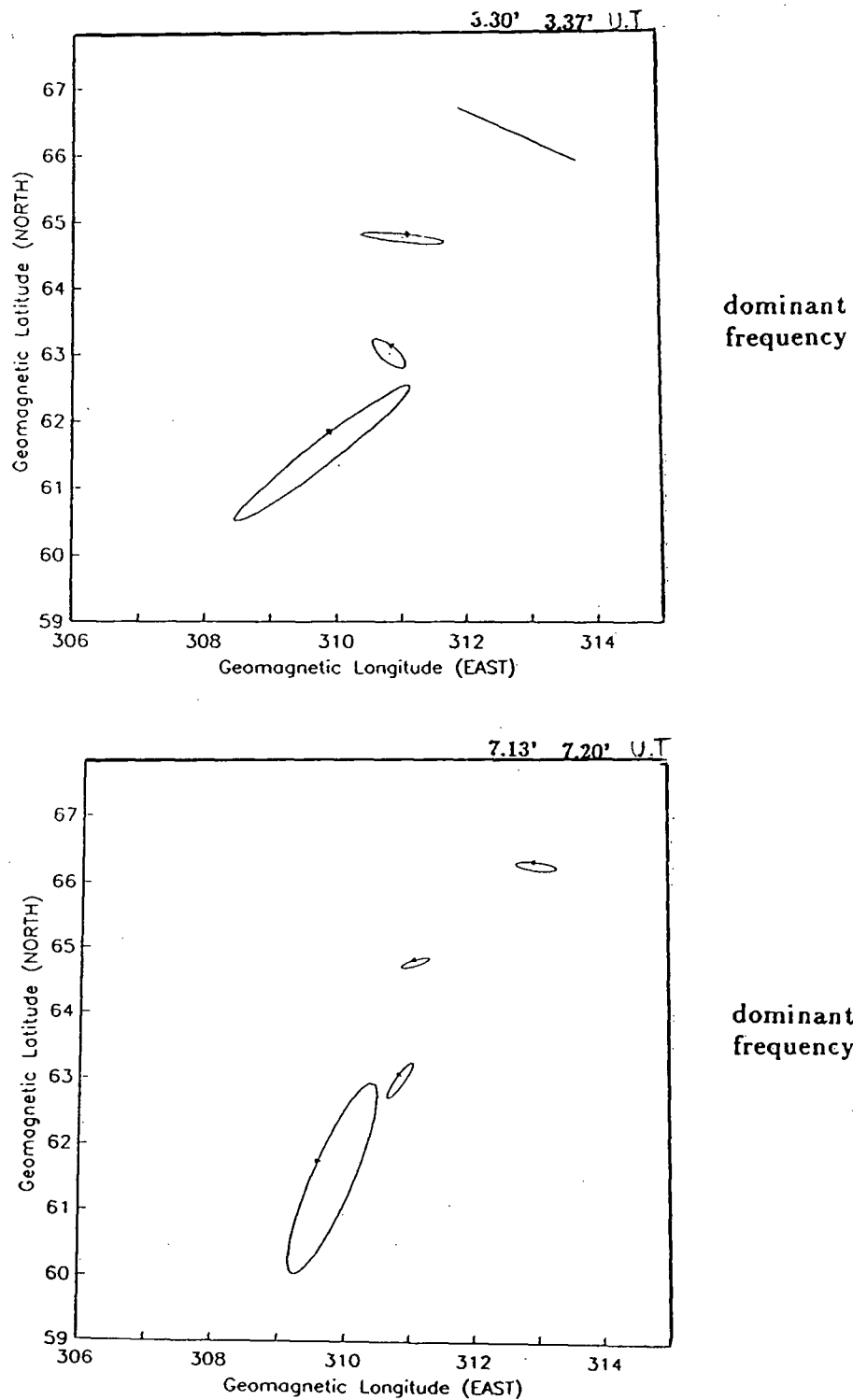


**Figure 40.** Same as Figure 37. Top:  $H_{max} = 3.1(\log_{10})$  and  $D_{max} = 3.4(\log_{10})$ . Bottom:  $H_{max} = 3.9(\log_{10})$  and  $D_{max} = 3.1(\log_{10})$ . In both events, the higher frequency component does not meet the criteria of acceptance established in Chapter 2 and the computation is omitted for that peak.

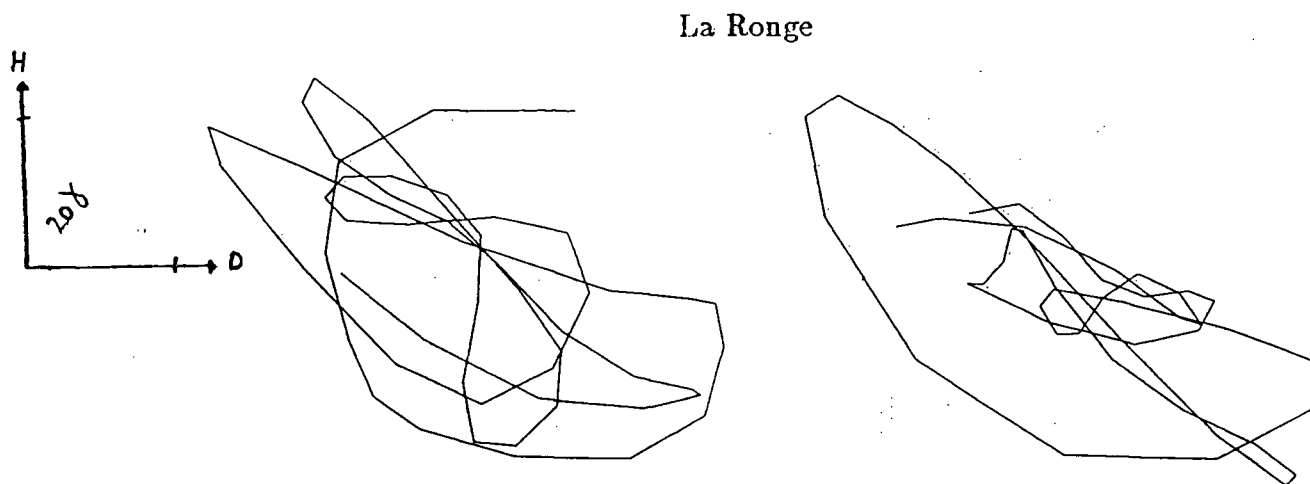
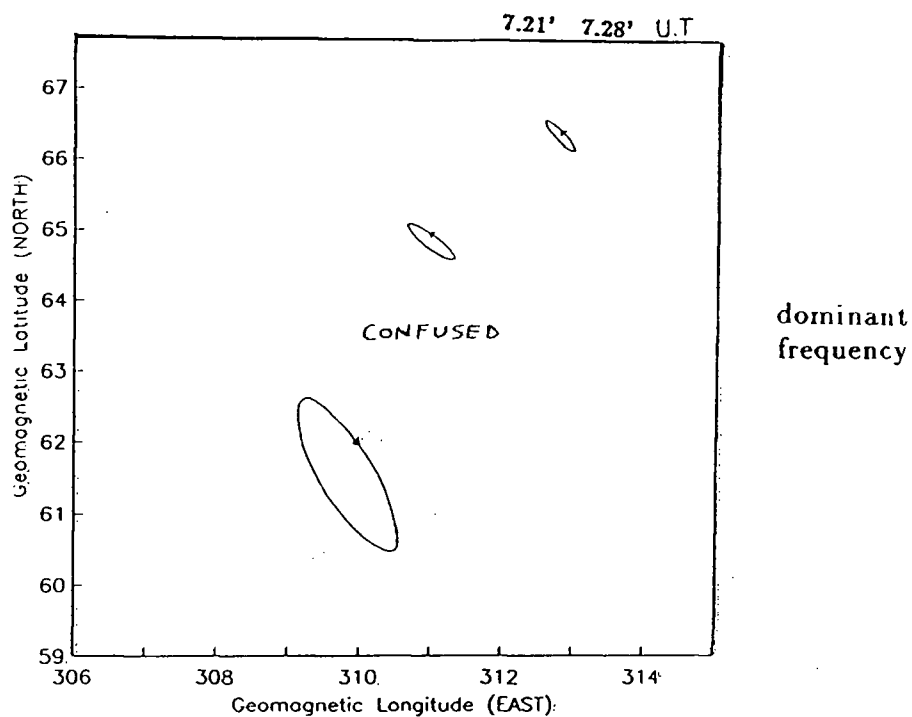


**Figure 41.** Top: same as Figure 37.  $H_{max} = 4.2(\log_{10})$  and  $D_{max} = 3.7(\log_{10})$ . As in Figure 40 the computation of the higher frequency component is omitted. Bottom: Dynamic polarization pattern in the time domain.

La Ronge; left: 7.21'- 7.24' U.T; right: 7.24'-7.28' U.T; August 08 1983.

## Conclusions

Two possible ionospheric electric currents were investigated to explain the Pi2 micropulsation. Both of them are based on the idea that the Pi2 generation and propagation lie in the coupling mechanism between the ionosphere and the magnetosphere when the electric balance is disturbed.

The first one uses an expanding network of lumped circuit elements to model the magnetosphere-ionosphere interaction; the second one examines the possibility of an ionospheric electric impulse imparted to a field-aligned current under the conditions of brightening of aurora. In the first case, the magnetosphere is the source region of Pi2; in the second case, the ionosphere is the source region. In both cases, the induced ionospheric Hall currents are the fields observed on the ground to first order.

It is found experimentally that the Pi2 originates possibly from these two source regions and can be explained as a resonant oscillation of the 3-D current system coupled together with a strong toroidal field existing in the ionosphere.

Observational results supporting the resonant current model are the following: the resonant region (located by the minimum in the H component or the maximum in the H and D components) is associated with a reversal of polarization in four out of five events. A symmetry is also found in the polarization result between the evening sector and the morning sector. In addition to that, eighteen Pi2 events out of twenty show elliptical polarization, which is also predicted. Data from a longitudinal chain of stations would be helpful to verify the polarization patterns predicted by Figures 27 and 28 and to locate the source region more precisely. So, there is a strong suggestion that the Pi2 is associated with a resonant oscillation of an expanding network of FAC at the early stage of the magnetic substorm.

The real current configuration of Pi2 cannot be known from ground magnetic observations alone: because the Pedersen current system produces no magnetic effects on the ground, one cannot conclude which current system predominates, the 3-D system or the Hall current. However the Pedersen currents produce a magnetic field above the ionosphere. The detection of these magnetic effects in and above the ionosphere is essentially important for knowing the real current configuration of the Pi2. Satellite data as well as a worldwide network of Pi2 events are therefore necessary.

It is also suggested that a strong toroidal field originates in the auroral arcs. The observational results supporting this model can be found in the dynamic Pi2 polarization patterns as shown in Figure 41: a highly disturbed figure of eight, which could be generated by an impulsive motion of FAC in the ionosphere (as proposed in Figure 30 and 31). To give more observational support to this model, it is suggested that events occurring during quieter geomagnetic days be analyzed, so that the dynamic polarization patterns would be less disturbed. In addition to that, the study of optical data showing the development of visible aurora during the events under study should be combined with an analysis of satellite data showing how field-aligned currents are related to different auroral features. If the Pi2 toroidal field originates in the ionosphere, then simultaneous onset should be observed on the ground and in the magnetosphere.

These preliminary models have to be proven in more rigorous mathematical terms. First of all, complete LC parameters should be derived. In particular, we assumed a linear or steady-state magnetospheric convection. In reality it is expected that magnetospheric convection is a highly non-steady state process owing to time variations in solar wind-magnetosphere interaction. A non-steady process would include the possibility that the source region itself might be shifted, in which case several spectral peaks could be predicted, as well as the presence of harmonics in the spectra. But maybe it is

possible to construct quantitative theoretical models of certain non-steady convection phenomena that to first order can be isolated from the complete convection problem. This particular point has to be examined carefully.

The possibility of a strong toroidal field of FAC's generated in the ionosphere (as shown in Figure 30), should also be verified mathematically as a possible initial condition and boundary condition which satisfy the MH equations.

Interesting results which cannot presently be explained are the following:

1. Even though the Pi2 is associated with the early stages of the substorm, the transmission of energy across latitudes is different from that of the substorm electrojet, and more surprising maybe the Pi2 source region seems to be different from the center of the substorm electrojet.
2. It was also found that the Pi2 source region is shifted to the north as successive events take place. This is suggested by three facts in the evening sector: the longer periods of successive Pi2's and the northward shift of their power and polarization characteristics. This is not so clearly verified in the morning sector which shows mixing of different events.
3. Another experimental result which cannot be clearly explained at the moment is the maximum in the power found at Park Site in four events out of five. Even though, Park Site is at the latitude of the plasmapause, one should not conclude too rapidly that the plasmapause is most likely the source region candidate for the Pi2 generation. It was observed in section 4.2 that the break-up latitude of the substorm was located far to the south (in relation to the high Kp index value). If the break-up of aurora also takes place far to the south, the Pi2 could be generated at this latitude in the ionosphere.

4. Finally, a higher frequency spectral peak (25-30 mHz) is related in phase and relative power to the dominant frequency (15-20 mHz). Their main difference lies in the % polarization, the dominant frequency showing disturbed polarization characteristics and the higher frequency component between 90 % and 100 % polarization (see Figure 13). One cannot conclude yet whether these two peaks are harmonically related or arise from different sources.

The last concluding remarks are the following: Ground magnetic observations are not sufficient for two reasons. First of all, one cannot always identify clearly the Pi2 in the time domain by visual inspection of the magnetogram or in the frequency by spectral analysis. The second reason is that, if mixed sources give rise to the Pi2 (a source of fac and an ionospheric source of shear mode oscillation), one needs a combination of optical data, radar auroral data as well as satellite data to separate these sources. Our experimental results are therefore limited and we have to guard ourselves from generalizing from what might only be special cases.

## Bibliography

- Afanas'yeva, L. T., Raspopov, O. M., and R. V. Shechepetnov, Relationship between geomagnetic perturbations of the Pi2 type and the parameters of the auroral zone, *Geomagn. Aeron.*, **10**, 600, 1970.
- Akasofu, S. -I., The latitudinal shift of the auroral belt, *J. Atmospheric. Terrest. Phys.*, **26**, 1167, 1964.
- Akasofu, S. -I. and A., Byung-Ho, Distribution of field-aligned currents and expected magnetic fields resulting from auroral currents along circular orbits of satellites. *J. Geophys. Res.*, **85**, 6883, 1980.
- Banks, P. M., *J. Atmos. Terrest. Phys.*, **37**, 951, 1975.
- Birkeland, K., The Norwegian Aurora Polaris expedition 1902-1903.1, *Cristiana*, Aschehoug, Norway, 315pp., 1908.
- Born, M. and Wolf, E., Principles of optics, *Pergamon Press*, Oxford, 1975.
- Bostrom, R., A model of the auroral electrojets, *J. Geophys. Res.*, **69**, 4983, 1964.
- Bostrom, R., Critical problems of magnetospheric Physics, *Eds E. R. Dyer*, Washington, D. C., 1972.
- Chang, R. P. H., and L. J. Lanzerotti, On the generation of magnetohydrodynamic waves at the onset of the substorm, *Geophys. Res. Lett.*, **2**, 489, 1975.
- Coroniti, F.V., and C.F.Kennel, Auroral micropulsation instability, *J. Geophys. Res.*, **75**, 1863, 1970.
- Dungey, J. W., Hydromagnetic waves, in *Physics of geomagnetic phenomena*, *Academic Press*, New York, 1967.
- Ecklund, W.L., Basley, B.B., and R. A., Greenwald, Crossed beam measurements of the diffuse aurora, *J. Geophys. Res.*, **80**, 1805, 1975.
- Ellis, P., and D.J. Southwood, Reflection of Alfvén waves by non-uniform ionospheres, *Planet. Space Sci.*, **31**, 1983.
- Fukunishi, H., Polarization changes of geomagnetic Pi2 pulsations associated with the plasmopause, *J. Geophys. Res.*, **80**, 98, 1975.
- Fukushima, N., Equivalence in ground geomagnetic effect between Chapman-Vestine's and Birkeland-Alfvén's electric current-systems for polar magnetic storms, *Rep. Ionos. Space Res.*, 219, 1969.
- Goertz, C. K., and R. W. Boswell, Magnetosphere-ionosphere coupling, *J. Geophys. Res.*, **84**, 7239, 1979.
- Greenwald, R. A., and W.L. Ecklund, A new look at radar auroral motions, *J. Geophys. Res.*, **80**, 3642, 1975.

- Greenwald, R. A., Weiss, W., and E. Nielsen, STARE: a new radar auroral backscatter experiment in northern Scandinavia, *Radio Science*, **13**, 1021, 1978.
- Haerendel, G., Preprint from Max-Planck-Institut, MPI-PAE-Extraterr. 44-70, July, 1970.
- Hasegawa, A., and L. Chen, Theory of magnetic pulsations, *Space Sci. Rev.*, **16**, 347, 1974.
- Heacock, R. R., and J. K. Chao, Type Pi magnetic field pulsations at very high latitudes and their relation to plasma convection in the magnetosphere, *J. Geophys. Res.*, **85**, 1203, 1980.
- Heppner, J. P., Electric field variations during substorms: OGO-6 measurements, *Planet. Space Sci.*, **20**, 1475, 1972.
- Hugues, W. J., The effect of the atmosphere and ionosphere on long period magnetospheric micropulsations, *Planet. Space Sci.*, **22**, 1157, 1974<sub>a</sub>.
- Hugues, W. J., and D. J. Southwood, The screening of micropulsation signal by the atmosphere and the ionosphere, *J. Geophys. Res.*, **81**, 3234, 1976<sub>a</sub>.
- Hugues, W. J., and D. J. Southwood, An illustration of modification of geomagnetic pulsation structure by the ionosphere, *J. Geophys. Res.*, **81**, 3241, 1976<sub>b</sub>.
- Jacobs, J. A., Geomagnetic micropulsations, Springer-Verlag, New York, N.Y., 1970.
- Kan, J. A., and R. R. Heacock, Generation of irregular (type Pi C) pulsations in the plasma sheet during substorms, *J. Geophys. Res.*, **81**, 2371, 1976.
- Kan, J. A., and L. C. Lee, Generation of Alfvén waves by deceleration of magnetospheric convection and broadband Pi pulsations, *J. Geophys. Res.*, **87**, 3511, 1982.
- Kanasewich, E. R. Time sequence analysis in geophysics, *The University of Alberta Press*, Edmonton, 1981.
- Kato, Y., and T. Watanabe, Studies on geomagnetic storm in relation to geomagnetic pulsation, *J. Geophys. Res.*, **63**, 741, 1958.
- Kato, Y., and T. Watanabe, Studies on geomagnetic pulsation, *Pc, Geophys.*, **8**, 1, 1957.
- Lanzerotti, L. J., and H. Fukunishi, *Rev. Geophys. Space Phys.*, **12**, 724, 1974.
- Mallinckrodt, A. J., and C. W. Carlson, Relations between transverse electric fields and field-aligned currents, *J. Geophys. Res.*, **83**, 1426, 1978.
- Maltsev, Yu . P., Leontyev, S. V., and W. B. Lyatsky, Pi2 pulsations as a result of evolution of an Alfvén impulse originating in the ionosphere during a brightening of aurora, *Planet. Space Sci.*, **22**, 1519, 1974.
- Maltsev, Yu . P., Lyatsky W. B., and A. M., Lyatskaya, Currents over the auroral arc, *Planet. Space Sci.*, **25**, 53, 1977.



- Miura, A., and T. Sato, Numerical simulation of global formation of auroral arcs, *J. Geophys. Res.*, **85**, 73, 1980.
- Nishida, A., Possible origin of transient dusk to dawn electric field in the nightside magnetosphere, *J. Geophys. Res.*, **84**, 3409, 1979.
- Olson, J. V., and G. Rostoker, Latitude variation of the spectral components of the auroral zone Pi2, *Planet. Space Sci.*, **25**, 663, 1977.
- Opgenoorth, H. J., Pellinen, R. J., Baujohann, W., Nielsen, E., Marklund, G., and L. Eliasson, Three dimensional current flow and particle precipitation in a westward travelling surge, *J. Geophys. Res.*, **88**, 3138, 1983.
- Pytte, T., and H. Treffall, Auroral zone electron precipitation event observed at the onset of negative bays, *J. Atmos. Terr. Phys.*, **34**, 315, 1972.
- Pytte, T., Mcpherron R. L., and S. Kokubun, The ground signature of the expansion phase during multiple onset substorms, *Planet. Space Sci.*, **24**, 1115, 1976.
- Reid, G. C., and T. E. Holzer, The response of the day side magnetosphere-ionosphere system to time varying field line reconnection at the magnetopause. Theoretical model, *J. Geophys. Res.*, **80**, 2050, 1975.
- Rostoker, G., The frequency spectrum of Pi2 micropulsation activity and its relationship to planetary magnetic activity, *J. Geophys. Res.*, **72**, 2032, 1967.
- Rostoker, G., and H.-L. Lam, A generation mechanism for Pc5 micropulsation activity at the polar cusp, *J. Geophys. Res.*, **77**, 4700, 1972.
- Rostoker, G., and H.-L. Lam, The relationship between Pc5 micropulsation activity in the morning sector to the auroral westward electrojet, *Planet. Space Sci.*, **26**, 473, 1978.
- Rostoker, G., and J.C. Samson, Polarization characteristics of Pi2 pulsations and implication for their source mechanisms: location of their source region with respect to the auroral electrojets, *Planet. Space Sci.*, **29**, 225, 1981.
- Saito, T., and S., Matsushita, *J. Geophys. Res.*, **73**, 267, 1968.
- Saito, T., Sakurai, T., and Y. Koyama, Mechanism of association between Pi2 pulsation and magnetospheric substorm, *J. Atmos. Terr. Phys.*, **38**, 1265, 1976.
- Samson, J.C., Description of the polarization states of vector processes: applications to ULF magnetic fields, *Geophys. J. R. astr. Soc.*, **34**, 403, 1973.
- Samson, J.C. and G. Rostoker, Polarization Characteristics of Pi2 micropulsations and implications for their source mechanisms. *Planet. Space Sci.*, 1980<sub>a</sub>.
- Samson, J.C., and G. Rostoker, Data adaptive polarization filters for multichannel geophysical data, *Geophys.*, **46**, 1423, 1981.

- Samson, J.C., Large-scale studies of Pi2's associated with auroral breakups, *J. Geophys.*, **56**, 133, 1985.
- Sato, T., and T. Iijima, Primary sources of large-scale Birkeland currents, *Space Sci. Rev.*, **24**, 347, 1979.
- Scholer, M., On the motion of artificial ion clouds in the magnetosphere, *Planet. Space Sci.*, **31**, 435, 1970.
- Southwood, D. J., Comments on field line resonance and micropulsations, *Geophys. J. R. Astr. Soc.*, **41**, 425, 1975.
- Stewart, A. M., On the great magnetic disturbance which extended from August 28 to September 7, 1959, as recorded by photography at the Kew Observatory, *Terr. Mag.*, **2**, 105, 1861.
- Stuart, W. F., A mechanism of selective enhancement of Pi2's by the plasmasphere, *J. Atmos. Terr. Phys.*, **36**, 851, 1974.
- Sutcliffe, P. R., Harmonics in Pi2 power spectra associated with the plasmopause, *J. Atmos. Terr. Phys.*, **38**, 1183, 1976.
- Troitskaya, J.A., and A. V. Gul'emi, Geomagnetic micropulsations and diagnosis in the magnetosphere, *Space Sci. Rev.*, **7**, 689, 1967.
- Troitskaya, J.A., Micropulsations and the state of the magnetosphere, in *Solar-Terrestrial Physics*, Academic Press, London, 1967.
- Ulrych, T. J., and T. N. Bishop, Maximum Entropy analysis and autoregressive decomposition, *Rev. of Geophys. and Space Phys.*, **13**, 183, 1975.
- Zmuda, A. J., and J. C. Armstrong, The diurnal flow pattern of field-aligned currents, *J. Geophys. Res.*, **79**, 4611, 1974.
- Watanabe, T., Geomagnetic bays and storm sudden commencements in high latitudes, *Geophysics*, **13**, 62, 1961.
- Watanabe, T., Oguti, T., Hayashi, K., Tsuruda, K., and R. E. Horita, Magnetic pulsations and auroral displays during the expansion phase of a substorm 18 september 1976, *J. Geomag. Geoelectr.*, **30**, 199, 1978.
- Westcott, E. M., Stolarik, J. D., and J. P. Heppner, Electric fields in the vicinity of auroral forms from motion of Barium vapor releases, *J. Geophys. Res.*, **74**, 3469, 1969.
- Wiens, R. G., and G. Rostoker, Characteristics of the development of the westward electrojet during the expansive phase of magnetospheric substorms, *J. Geophys. Res.*, **80**, 2109, 1975.

## Appendix A. Instrumentation and Pre-processing

### 1. Analog instruments

When recording micropulsations, one must ensure that the frequency band of all the units can accomodate the frequency range of the micropulsations (See Table A1).

Instruments	Frequency Band
Induction Magnetometer	$\sim 2\text{Hz}$
Tape recorder	0~ 17Hz
Tape playback	0~ 17Hz

**Table A1.**

One should also have knowledge of the response characteristics of all the units (See Table A2).

Stations	Induc.Mag	Amplifier	Gain	Tape Recorder
S End	$70\mu\text{V}/\gamma/\text{Hz}$	OP-7	$4.3 \times 10^4$	1
L Ronge	$70\mu\text{V}/\gamma/\text{Hz}$	ANCOM	$2.0 \times 10^5$ (High) $4.0 \times 10^4$ (Low)	25/14
C Lake	$70\mu\text{V}/\gamma/\text{Hz}$	ANCOM	$2.0 \times 10^5$ (High) $4.0 \times 10^4$ (Low)	1
P Site	$70\mu\text{V}/\gamma/\text{Hz}$	ANCOM	$2.0 \times 10^5$ (High) $4.0 \times 10^4$ (Low)	1

**Table A2.**

Note that, when recording, the polarity of the three components of the magnetic field was reversed at La Ronge; the polarity of the N-S component was reversed at Park Site.

## 2. Digitization

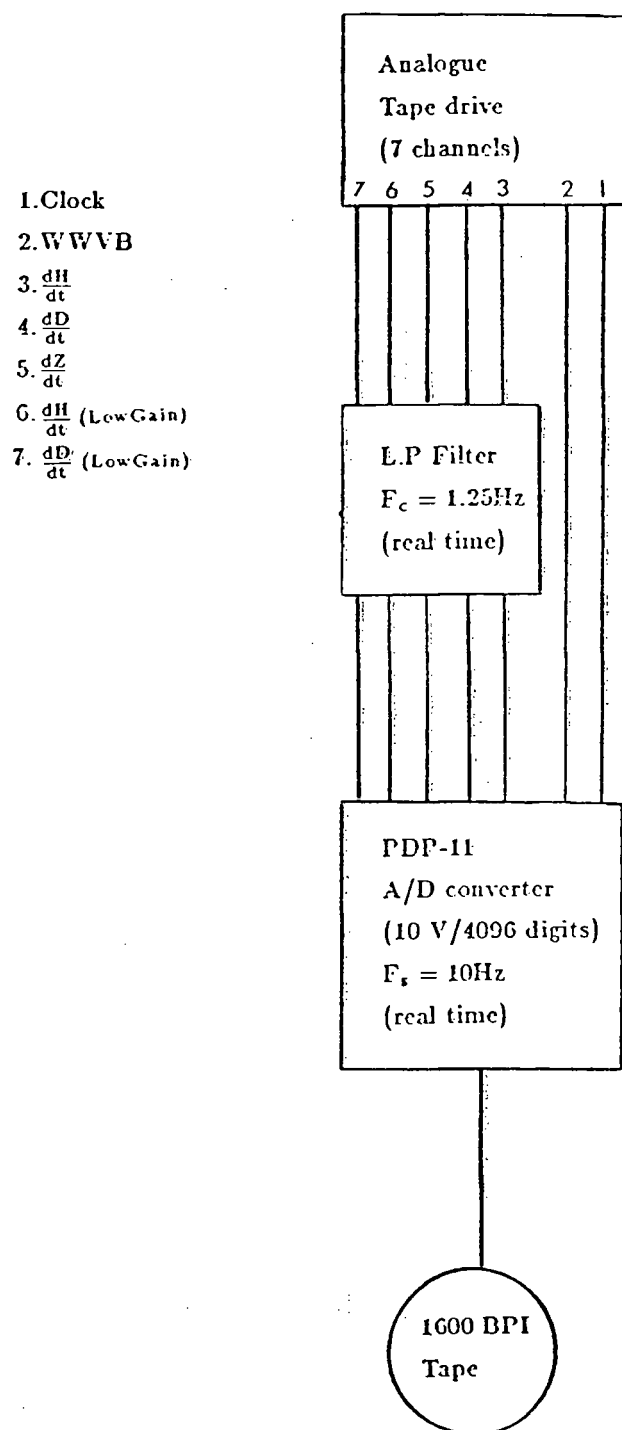


Figure A1. Block diagram of analog-to-digital conversion system.

### 3. Digital pre-processing

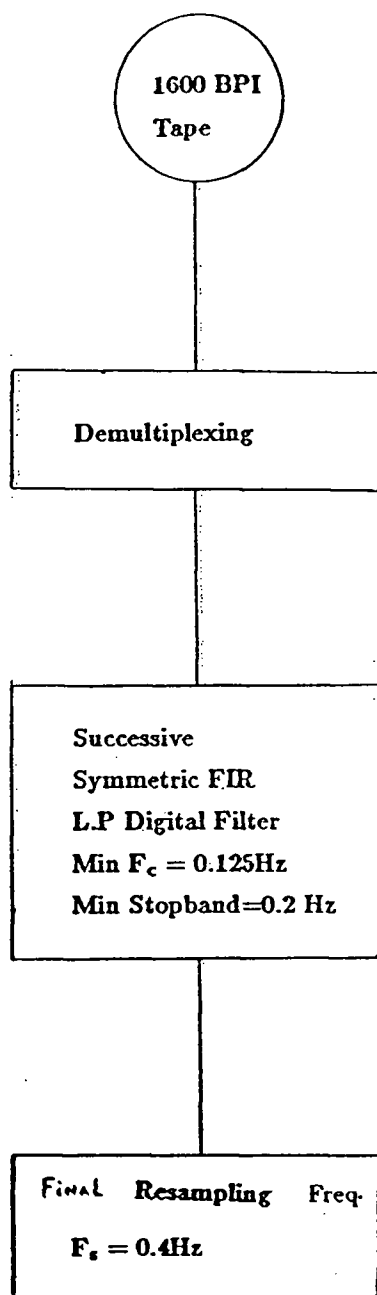


Figure A2. Block diagram of digital pre-processing

#### 4. Conversion to units of gammas

The sensitivity of the University of Tokyo coil is  $70 \mu\text{V}/\gamma/\text{Hz}$ , which means that a signal of amplitude  $1 \gamma$  and frequency of  $1 \text{ Hz}$  will induce an electromotive force of  $70 \mu\text{V}$ .

We can start with a simple equation to describe the time variations of the magnetic field:

$$b = b_o \sin(2\pi ft) \quad (\text{A.1})$$

where  $f$  is the frequency of oscillation and  $b_o$  the amplitude of the disturbance.

The magnetic flux  $\Phi_b$  going through the coil is given by:

$$\Phi_b = bA \quad (\text{A.2})$$

where  $b$  is the magnetic disturbance and  $A$  is the total area of the coil. The induced electromotive force (emf) is given by:

$$\frac{d\Phi_b}{dt} = A \frac{db}{dt} \quad (\text{A.3})$$

Substituting (A.1) into (A.3), we get:

$$\frac{d\Phi_b}{dt} = 2\pi f b_o A \cos 2\pi ft \quad (\text{A.4})$$

The area  $A$  of the coil can easily be calculated:

$$2\pi f b_o A = 70\mu V / \gamma / \text{Hz}$$

$$\begin{aligned} A &= \frac{70 \times 10^{-6}}{2\pi \times 10^{-9}} m^2 \\ &= 11 \times 10^3 m^2 \end{aligned} \tag{A.5}$$

The emf is fed to a high impedance amplifier so that the output voltage of the induction magnetometer becomes:

$$\begin{aligned} V(t) &= \frac{d\Phi_b}{dt} \times G \\ &= A \frac{db}{dt} \times G \end{aligned} \tag{A.6}$$

where  $G$  is the gain. After digitization, all the stations were scaled to the same degree of amplification:

$$\begin{aligned} G &= \frac{7.5K\Omega}{7.5K\Omega + 5K\Omega} \times 40,000 \\ &= 24,000 \end{aligned} \tag{A.7}$$

where  $7.5K\Omega$  and  $5K\Omega$  are the d.c resistance of the head sensor and the input impedance of the amplifier.

Rearranging (A.6) and using the PDP-11 A/D conversion factor (10V/4096 digits) , we obtain in units of gammas:

$$\frac{10V}{4096} \times \frac{GA}{1V} \times \frac{db}{dt} \times 10^{-9} = \frac{2.6\gamma/s}{4096 \text{ digits}} \tag{A.8}$$

## 5.Integration

We can rearrange (A.6), as follows:

$$\frac{db}{dt} = \frac{V(t)}{GA} \quad (A.9)$$

and integrate (A.9):

$$b(t) - b(0) = \frac{1}{GA} \int_0^t V(t) dt \quad (A.10)$$

In a digital form, this integral becomes:

$$b(n\Delta t) = \frac{1}{GA} [V(0) + V(\Delta t_o) + V(2\Delta t_o) + \cdots V(n\Delta t_o)] \times \Delta t_o \quad (A.11)$$

where  $\Delta t_o = 2.5$  sec is the digitizing interval.

Using the PDP-11 A/D conversion factor, we obtain in units of gammas:

$$\begin{aligned} b_t &= \frac{10^9 \Delta t_o}{GA} \times 10V \\ &= 93\gamma \end{aligned} \quad (A.12)$$

This gives for our digital output the following conversion factor:

$$93\gamma \iff 4096 \text{ digits}$$

$$1\gamma \iff 44 \text{ digits} \quad (A.13)$$



## Appendix B. Digital Filters

### 1. Polarization filter or detection of polarized waveforms

As discussed in Chapter 2, Pi2 micropulsations are contaminated by substorm noise and their respective energy lie in the same frequency band. Can we attempt to differentiate between these two sources?

Assuming that micropulsations are quasi-monochromatic plane waves and that the substorm oscillations are randomly polarized, one can design a filter which will detect the polarized waveforms only. The calculations are done in the frequency domain, using the spectral matrix which is formed from the power and the cross power spectra of the H and D components.

The spectral matrix of the original data can be considered as the sum of polarized and unpolarized powers. This superposition principle is largely used in optics (Born and Wolf, 1975, p. 550); if it is valid for the electric field, it is also valid for the magnetic field:

$$J = P + U$$

$$\begin{pmatrix} J_x J_x^* & J_x J_y^* \\ J_y J_x^* & J_y J_y^* \end{pmatrix} = \begin{pmatrix} P_x P_x^* & P_x P_y^* \\ P_y P_x^* & P_y P_y^* \end{pmatrix} + \begin{pmatrix} U_x U_x^* & 0 \\ 0 & U_y U_y^* \end{pmatrix} \quad (B.1)$$

where P is the spectral matrix of the polarized waveforms and U that of the unpolarized waveforms, \* represents the complex conjugate. For pure white noise,  $U_x U_x^* = U_y U_y^* = U U^*$  and the cross-power spectra of the unpolarized signals is 0. From (B.1), one can deduce the following relations:

$$J_x J_x^* = P_x P_x^* + U U^* \quad (B.2)$$

$$J_y J_x^* = P_y P_x^* \quad (B.3)$$

$$J_x J_y^* = P_x P_y^* \quad (B.4)$$

$$J_y J_y^* = P_y P_y^* + U U^* \quad (B.5)$$

The degree of polarization is defined by:

$$R = \frac{I_P}{I_J} \quad (B.6)$$

where  $I$  is the intensity, or the trace of the matrices  $P$  and  $J$  respectively.

$I_P$  has to be expressed in terms of the elements of the matrix  $J$  (formed from the original data):

$$I_P = J_x J_x^* + J_y J_y^* - 2U U^* \quad (B.7)$$

Using equations (B.2) to (B.5) and the fact that the determinant of  $P$  is 0 (this can be easily verified) , we can also express  $U$  in terms of  $J$ .

$$P_x P_x^* P_y P_y^* - P_y P_x^* P_x P_y^* = 0 \quad (B.8)$$

$$(J_x J_x^* - U U^*)(J_y J_y^* - U U^*) - J_y J_x^* J_x J_y^* = 0 \quad (B.9)$$

$$J_x J_x^* J_y J_y^* - J_x J_x^* U U^* - J_y J_y^* U U^* - (U U^*)^2 - J_y J_x^* J_x J_y^* = 0 \quad (B.10)$$

$$(U U^*)^2 - \text{Tr}(J) U U^* + \det J = 0 \quad (B.11)$$

where  $\text{Tr}(J)$  is the trace of the matrix. Solving the quadratic in  $UU^*$ , we get:

$$UU^* = \frac{1}{2}\text{Tr}(J) \pm \frac{1}{2} \left[ \text{Tr}^2(J) - 4 \det J \right]^{1/2} \quad (B.12)$$

Taking the positive square root gives unacceptable negative values for  $P_x P_x^*$  and  $P_y P_y^*$ , therefore, the negative root is selected.

Combining equations (B.6), (B.7) and (B.12) gives the following result:

$$R^2 = \frac{\text{Tr}^2(J) - 4 \det J}{\text{Tr}^2(J)} \quad (B.13)$$

$$R = \left[ 1 - \frac{4 \det J}{\text{Tr}^2(J)} \right]^{1/2} \quad (B.14)$$

is the degree of polarization ( $0 \leq R \leq 1$ ). For quasi-monochromatic waves, the  $\det J$  is 0 and  $R$  is 1. Completely unpolarized wave fields have a spectral matrix which is just a multiple of the identity matrix:

$$U = I \begin{pmatrix} 1 & 0 \\ 0 & 1 \end{pmatrix} \quad (B.15)$$

with  $\det U = I^2$ ,  $\text{Tr}(U) = 2I$ , and therefore  $4 \det U = \text{Tr}^2(U)$  and  $R=0$ .

The filter is then simply designed as shown in Fig.B1. The selectivity can be increased by raising  $R$  to some power  $g$ . Increasing the power  $g$  results in a filtered output with a sinusoidal character.

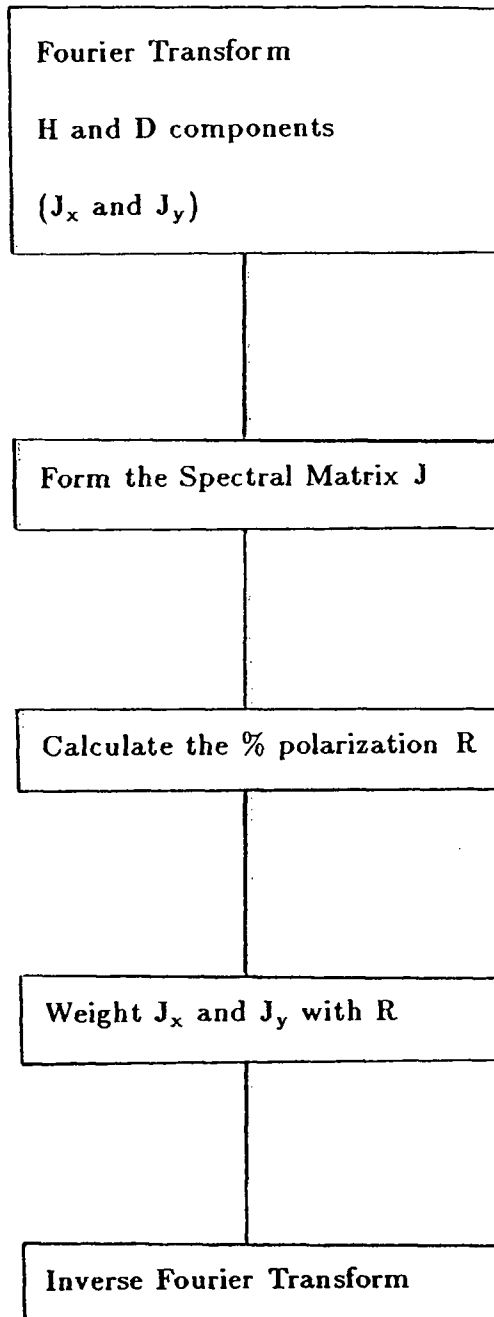


**Figure B.1.** Block diagram of a simple polarization filter.

Whether this technique can be applied to differentiate between the Pi2 features and the general substorm features is discussed in Chapter 2. For further investigations on this technique, see Samson (1973).

## 2. Digital integrator

A simple analysis of an RC network shows that its circuit can be used as an integrator and a low pass filter.

In this subsection, we carry out the analysis of the analog circuit (See Figure B2) to understand why and how one can use an equivalent digital technique to filter the Pi2 micropulsation directly from the time derivative of the magnetic field. In Figure B2, the first Op-Amp act as an integrator, the second one as an inverter. From this simple circuit analysis, one can write the four following equations:

$$I_1 + I_2 = \frac{V_i(t)}{R_s} \quad (B'.1)$$

$$V_o(t) = -R_f I_1 \quad (B'.2)$$

$$V_o(t) = -\frac{q}{C_f} \quad (B'.3)$$

$$\frac{dq}{dt} = I_2 \quad (B'.4)$$

Combining these equations, we get:

$$-\frac{V_o(t)}{R_f} - C_f \frac{dV_o}{dt} = \frac{V_i(t)}{R_s} \quad (B'.5)$$

$$-R_f C_f \frac{dV_o}{dt} - V_o(t) = \frac{R_f}{R_s} V_i(t) \quad (B'.6)$$

The second Op-Amp acts as an inverter, it changes the sign of  $V_o$ :

$$R_f C_f \frac{dV_o}{dt} + V_o(t) = \frac{R_f}{R_s} V_i(t) \quad (B'.7)$$

$$\frac{dV_o}{dt} + \frac{1}{\tau} V_o(t) = \frac{R_f}{R_s \tau} V_i(t) \quad (B'.8)$$

where  $\tau = R_f C_f$  is the time constant of the circuit.

It is easy to show that, under the conditions that the period  $T$  (of  $V_o$ ) is much shorter than the time scale  $\tau$ :

$$T \ll \tau$$

the circuit acts as an integrator. In the case of Pi2, a time scale of 10 minutes and a period of 1 minute or less will satisfy the condition. For periods greater than 1 minute, the integrator will not act with as much reliability.

The general solution for  $V_o(t)$  is easily obtained:

$$\begin{aligned} V_o(t) &= e^{-t/\tau} \left[ \int e^{t/\tau} \frac{R_f}{R_s \tau} V_i(t) dt + C \right] \\ &= C e^{-t/\tau} + e^{-t/\tau} \int e^{t/\tau} \frac{R_f}{R_s \tau} V_i(t) dt \\ &= C e^{-t/\tau} + e^{-t/\tau} \int e^{t/\tau} V_i'(t) dt \end{aligned} \quad (B'.9)$$

where  $V_i'(t) = \frac{R_f}{\tau R_s} V_i(t)$ .

The first term of the solution represents the trend which is not of interest to us and can be set to zero.

It is easy to evaluate digitally this equation:

$$\begin{aligned}
 V_{o1}(\Delta t) &= e^{-\Delta t/\tau} (V'_i(\Delta t) e^{\Delta t/\tau}) \\
 V_{o2}(2\Delta t) &= e^{-2\Delta t/\tau} (V'_i(\Delta t) e^{\Delta t/\tau} + V'_i(2\Delta t) e^{2\Delta t/\tau}) \\
 &\vdots \\
 V_{on}(n\Delta t) &= e^{-n\Delta t/\tau} (V'_i(\Delta t) e^{\Delta t/\tau} + \dots + V'_i(n\Delta t) e^{n\Delta t/\tau}) \quad (B'.10)
 \end{aligned}$$

where  $\Delta t$  is the discrete time interval (2.5 sec) and  $n$ , the number of data points. For Pi2, we choose the integration time constant to be 10 minutes, the digitization interval  $\Delta t$  is 2.5 sec. The result of the application of this technique is discussed in Chapter 2.

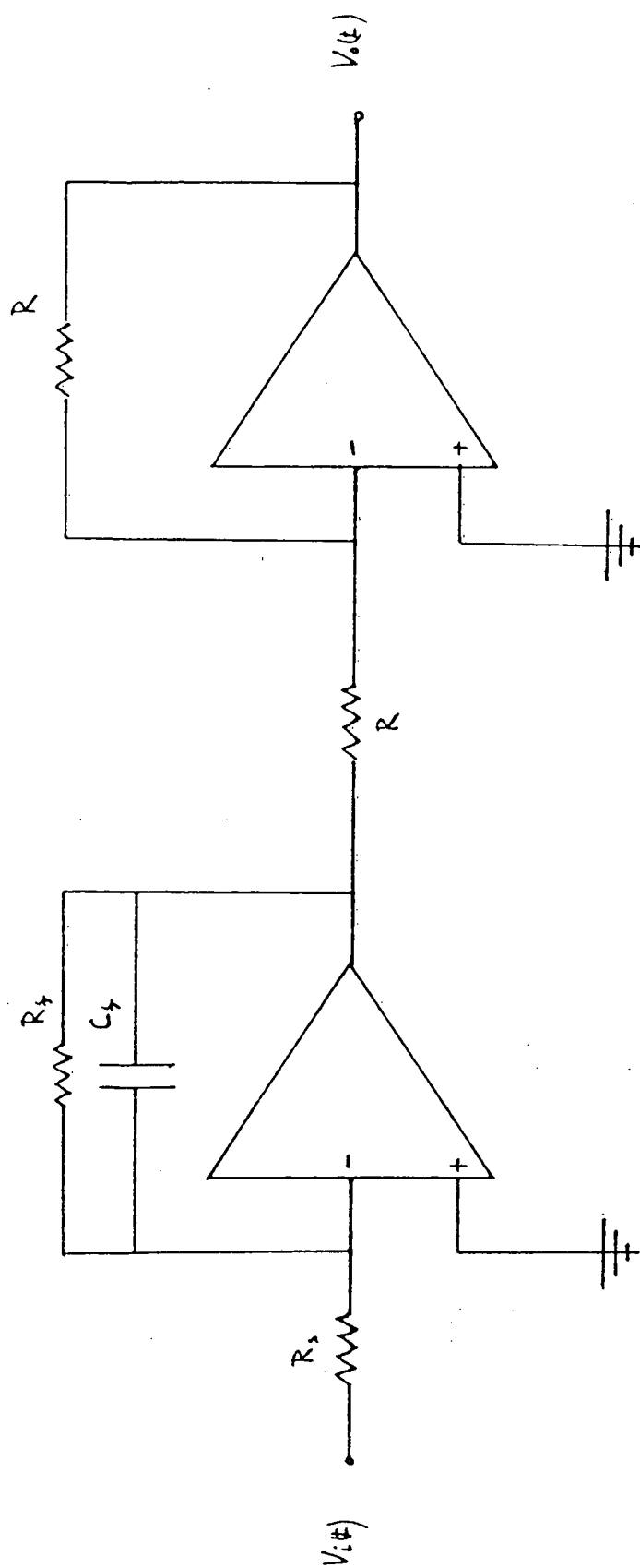


Figure 8.2 Integrator Circuit.



## Appendix C. Current Loop Model

Consider a circular current loop lying at ionospheric height,  $110 \text{ km}$  above the ground. The loop of radius  $a$  (chosen to be  $50 \text{ Km}$  in this model), lies in the X-Y plane as shown in Figure C.1 and carries a current  $I$ .

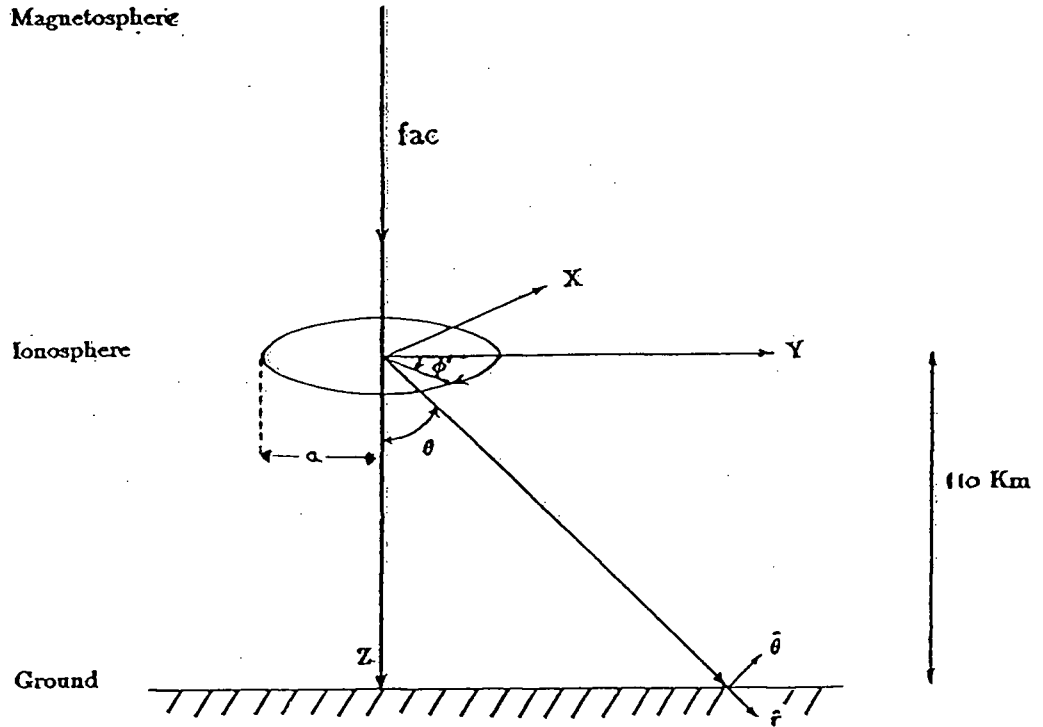


Figure C.1.

The vector potential, as derived by Jackson, is given by:

$$A_{\phi}(r, \theta) = \int_0^{2\pi} \frac{\cos \phi' d\phi'}{(a^2 + r^2 - 2ar \sin \theta \cos \phi')^{\frac{1}{2}}} \quad (\text{C.1})$$

This integral can be expressed in terms of the complete elliptical integrals K and E (see mathematical Tables):

$$A_{\phi}(r, \theta) = \frac{4Ia}{c\sqrt{a^2 + r^2 + 2ar \sin \theta}} \left\{ \frac{(2 - k^2)K(k) - 2E(k)}{k^2} \right\} \quad (C.2)$$

where the argument of the elliptical integrals is:

$$k^2 = \frac{4ar \sin \theta}{a^2 + r^2 + 2ar \sin \theta}$$

The three components of the magnetic induction B are:

$$\begin{aligned} B_r &= \frac{1}{r \sin \theta} \frac{\partial}{\partial \theta} (\sin \theta A_{\phi}) \\ B_{\theta} &= -\frac{1}{r} \frac{\partial}{\partial r} (r A_{\phi}) \\ B_{\phi} &= 0 \end{aligned} \quad (C.3)$$

Far away from the loop, the field is dipolar in character ( $\frac{r}{a} \gg 1$ ). However, in our ionospheric model, the approximation cannot be made ( $\frac{r}{a}$  at  $\theta = 0$  is 2.2). Therefore, one has to solve the elliptical integrals numerically to compute  $B_r$  and  $B_{\theta}$ .

First, converting cgs to mks units ( $\mu_o = \frac{4\pi}{c^2}$ ):

$$A_{\phi} = \frac{\mu_o 4Ia}{4\pi\sqrt{a^2 + r^2 + 2ar \sin \theta}} \left\{ \frac{(2 - k^2)K(k) - 2E(k)}{k^2} \right\} \quad (C.4)$$

$$\text{Let } F_1(r, \theta) = \frac{\mu_o 4Ia}{4\pi\sqrt{a^2 + r^2 + 2ar \sin \theta}}$$

$$\text{Let } F_2(r, \theta) = \frac{(2 - k^2)(K(k) - 2E(k))}{k^2}$$

1. The radial component of the magnetic field is computed as follows:

$$\begin{aligned}
B_r &= \frac{1}{r \sin \theta} \frac{\partial}{\partial \theta} (\sin \theta A_\phi) \\
&= \frac{1}{r \sin \theta} \frac{\partial}{\partial \theta} (F_1(r, \theta) F_2(r, \theta) \sin \theta) \\
&= \frac{1}{r \sin \theta} \left\{ F_2(r, \theta) \frac{\partial}{\partial \theta} (\sin \theta F_1(r, \theta)) + \sin \theta F_1(r, \theta) \frac{\partial}{\partial \theta} F_2(r, \theta) \right\}
\end{aligned} \tag{C.5}$$

Let us call the first term  $B_{r1}$  and the second term  $B_{r2}$

$$\begin{aligned}
B_{r1} &= \frac{1}{r \sin \theta} \left\{ F_2(r, \theta) \frac{\partial}{\partial \theta} (\sin \theta F_1(r, \theta)) \right\} \\
&= \frac{F_2(r, \theta)}{r \sin \theta} \left\{ \cos \theta F_1(r, \theta) + \sin \theta \frac{\partial F_1(r, \theta)}{\partial \theta} \right\} \\
&= \frac{\mu_o 4 I a}{4 \pi r} F_2(r, \theta) \cot \theta \left\{ \frac{a^2 + r^2 + ar \sin \theta}{(a^2 + r^2 + 2ar \sin \theta)^{3/2}} \right\} \\
B_{r2} &= \frac{F_1(r, \theta)}{r} \frac{\partial}{\partial \theta} (F_2(r, \theta))
\end{aligned} \tag{C.6}$$

$\frac{\partial F_2(r, \theta)}{\partial \theta}$  is evaluated numerically using finite differences:  $\frac{\partial}{\partial \theta} F_2(r, \theta) \sim \frac{F_2(\theta + \Delta \theta) - F_2(\theta - \Delta \theta)}{2 \Delta \theta}$

The total radial component is:

$$B_r = B_{r1} + B_{r2} \tag{C.7}$$

2. The tangential component of the magnetic field can be computed as follows:

$$\begin{aligned}
B_\theta &= -\frac{1}{r} \frac{\partial}{\partial r} (r A_\phi) \\
&= -\frac{1}{r} \frac{\partial}{\partial r} (r F_1(r, \theta) F_2(r, \theta)) \\
&= -\frac{F_2(r, \theta)}{r} \frac{\partial}{\partial r} (r F_1(r, \theta)) - F_1(r, \theta) \frac{\partial}{\partial r} F_2(r, \theta).
\end{aligned} \tag{C.8}$$

Let us call the first term  $B_{\theta 1}$  and the second term  $B_{\theta 2}$

$$\begin{aligned}
B_{\theta 1} &= -\frac{F_2(r, \theta)}{r} \frac{\partial}{\partial r} (r F_1(r, \theta)) \\
&= -\frac{F_2(r, \theta)}{r} \left\{ F_1(r, \theta) + r \frac{\partial}{\partial r} F_1(r, \theta) \right\} \\
&= -\frac{\mu_0 4 I a F_2(r, \theta)}{4 \pi r} \left\{ \frac{a^2 + a r \sin \theta}{(a^2 + r^2 + 2 a r \sin \theta)^{3/2}} \right\} \\
B_{\theta 2} &= -F_1(r, \theta) \frac{\partial}{\partial r} (F_2(r, \theta))
\end{aligned} \tag{C.9}$$

$\frac{\partial F_2(r, \theta)}{\partial r}$  is evaluated numerically using finite differences:  $\frac{\partial}{\partial r} F_2(r, \theta) \sim \frac{F_2(r+\Delta r) - F_2(r-\Delta r)}{2\Delta r}$

The total tangential component is:

$$B_{\theta} = B_{\theta 1} + B_{\theta 2} \tag{C.10}$$

The local earth's conductivity affects the magnetic field induction in the Z direction, therefore only the horizontal components are considered:

$$B_H = B_{\theta} \cos \theta + B_r \sin \theta \tag{C.11}$$

Finally, transforming from polar coordinates to cartesian coordinates, at any longitude Y, we have:

$$B_y = (B_{\theta} \cos \theta + B_r \sin \theta) \cos \phi \tag{C.12}$$

where  $\phi = \tan^{-1} x/y$

Similarly, at any latitude X, we have:

$$B_x = (B_\theta \cos \theta + B_r \sin \theta) \sin \phi \quad (C.13)$$

The result of this computation is shown in Figure 21 for a d.c. current of  $3 \times 10^5$  A flowing in a counterclockwise direction.

## Appendix D. Summary of principal theories proposed in the literature

Possible generation mechanisms of Pi2 pulsations proposed in the literature can be categorized into transient response mechanisms and instability mechanisms. They can be briefly summarized as follows:

Instability mechanisms interpret the observed Pi2 pulsations as MHD waves generated by instabilities. The nature of the predicted wave spectrum depends upon growth rates of the processes involved. Growth rates of MHD waves have been studied by several workers under various conditions. These include enhanced temperature gradient near the inner edge of the plasma sheet (Coroniti and Kennel, 1970), beam-plasma interaction in the near-earth plasma sheet (Chang and Lanzerotti, 1975), enhanced pressure anisotropy resulting from enhanced field-aligned plasma flow along the plasma sheet (Kan and Heacock, 1976), ionospheric response due to phase shifts between enhanced ionospheric current and number density (Sato, 1978; Miura and Sato, 1980), and the deceleration of magnetospheric convection due to ionospheric loading (Kan *et al.*, 1982).

Transient-response mechanisms interpret the observed Pi2 pulsations as large-amplitude Alfvén waves launched by a sudden change in the magnetospheric convection and/or magnetospheric configuration (Stuart, 1974; Maltsev *et al.*, 1974; Saito *et al.*, 1976; Olson and Rostoker, 1977; Rostoker and Samson, 1981). The launched Alfvén waves are subsequently damped by the ionosphere during reflection (Newton *et al.*, 1978). Certain aspects of the transient response in the magnetosphere-ionosphere coupling have been discussed by Maltsev *et al.* (1974, 1977), Mallinckrodt and Carlson (1978), Rostoker and Lam (1972), Nishida (1979), Goertz and Boswell (1979), Sato and Iijima (1979), and Heacock and Chao (1980).

# Appendix E. KP and AE Indices for August 08 1983

AUGUST 1983

Day		Kp Three-Hourly Indices								Sum
		1	2	3	4	5	6	7	8	
1	Q6	1-	2-	2	1-	1+	1-	1+	2+	11-
2	D3	4+	4	5+	3+	5+	4-	4+	4-	34
3		4-	3-	1+	2+	3+	3	4+	4-	24+
4	Q7	2	2+	1+	1	1	1-	1+	2-	11+
5	Q2	1-	0+	0+	0	0+	0+	1-	1+	4
6	Q8	1	2	0+	1-	2	2	2+	2-	12
7		1	1-	2	2-	2	2+	4+	6	20
8	D1	7+	8-	6+	4+	2+	2+	1+	3-	34+
9		5-	3	2-	2-	2	2	1+	1	17+
10	Q4	1-	2+	1	2-	2-	1	0+	1+	10
11	Q9	2	2-	1-	1+	2-	2-	3-	1+	13
12		3-	4+	4-	3	4	4-	5	4+	31-
13		4	3+	4+	5	4	2	3-	4+	30-
14		3	2-	2-	1	2	3-	3	2+	17+
15		3	2	1	3-	2+	3+	2-	3-	19-
16	Q3	1+	0	0	0+	2-	1+	2+	2	9
17	Q10	2+	2	1+	2-	1+	1	1+	2+	13+
18	Q1	1-	0+	0	0+	0+	0+	0	1-	3-
19		0	0+	0+	2	3+	4	2+	2+	15-
20		1	3-	2-	2-	2	3-	4	3-	18+
21		4+	3	3+	5-	3+	4+	4-	4	31-
22		2-	2-	2	3	3-	3-	5	3-	21+
23	D4	3	6	5-	4	4	3+	5-	3-	32+
24		3+	4+	4	4+	3+	3+	4-	3+	30-
25	D2	6	4	5+	4	4	3+	5-	3	34+
26		5-	5-	3	3+	3	4+	5	2-	30-
27	Q5	2+	0+	0+	1-	2+	2-	1+	1-	10-
28		3-	2	1+	2+	2+	1+	3-	2-	16+
29		3-	2+	1+	2+	3	3+	4	5-	24-
30		4+	4	4-	2+	3-	3	3-	3+	26
31	D5	5	4-	4	3+	3-	5-	4+	4+	32

Mean

		AE Index ( Hourly mean values, unit nT )																August 1983								Mean
Date		0	1	2	3	4	5	6	7	8	9	10	11	12	13	14	15	16	17	18	19	20	21	22	23	
D	1	63	64	107	216	201	170	237	238	186	133	124	113	144	259	170	101	143	159	103	115	167	142	272	332	165
	2	386	658	584	480	307	294	758	730	399	133	141	217	624	849	596	309	201	306	534	989	565	258	357	479	465
	3	489	296	131	79	241	80	93	67	84	87	77	155	280	306	299	339	326	259	602	471	208	166	490	371	250
	4	202	263	334	346	235	131	115	175	165	122	60	115	136	179	123	141	125	70	47	68	157	302	205	203	167
Q	5	108	77	60	42	51	44	49	43	70	59	56	42	44	50	44	33	32	33	40	46	49	48	40	46	50
D	6	41	50	55	44	47	66	36	31	40	52	54	56	52	73	109	133	189	290	143	160	313	237	89	95	102
	7	67	78	134	110	62	68	73	74	86	80	69	81	135	107	168	97	117	102	238	331	374	767	645	685	198
	8	870	1164	810	974	1282	506	336	574	504	717	683	270	90	84	84	81	91	72	65	51	52	62	181	251	411
	9	487	636	599	199	111	92	63	46	55	55	52	50	71	128	83	65	84	110	40	72	73	64	58	52	139
Q	10	49	58	54	170	385	386	283	137	85	135	154	258	163	163	140	130	109	76	57	53	43	51	49	77	136
	11	111	209	164	95	117	117	70	46	54	59	131	182	388	278	76	62	66	91	250	315	263	197	69	82	145
	12	257	191	249	377	650	533	469	570	682	571	560	715	599	433	587	774	766	692	579	506	362	375	356	528	516
	13	610	330	116	315	563	579	252	490	726	488	590	699	706	155	79	65	65	234	372	464	300	597	345	168	388
	14	189	464	236	81	95	270	202	159	149	109	63	80	97	223	224	133	206	318	309	270	322	235	92	100	193
	15	159	490	342	234	117	155	102	93	60	140	328	451	160	62	134	314	532	467	97	65	103	238	229	112	216
Q	16	109	169	108	34	37	39	53	63	62	54	66	84	97	154	246	321	390	274	420	261	225	221	318	339	173
Q	17	443	444	370	258	267	275	119	78	87	119	204	119	84	67	74	73	53	46	50	63	62	81	161	77	153
	18	62	59	56	68	41	37	39	43	66	90	77	67	85	91	71	43	45	48	45	42	55	59	53	55	58
	19	44	41	41	38	44	58	49	43	47	52	58	86	121	297	528	694	564	394	156	100	73	161	297	146	172
	20	60	71	110	410	444	229	166	157	143	95	196	267	490	251	237	190	211	422	387	480	472	434	456	479	286
D	21	466	468	560	669	585	587	397	549	707	776	464	664	727	583	570	649	693	553	501	413	266	208	560	303	538
	22	186	159	87	67	89	156	271	295	143	153	301	243	340	206	146	115	282	448	448	660	729	153	117	141	247
	23	157	298	347	680	966	790	291	463	632	485	536	503	443	377	249	195	385	646	594	587	412	247	193	269	448
	24	501	457	419	410	576	306	361	524	603	424	764	809	528	554	281	427	416	217	205	329	508	723	605	533	478
D	25	644	838	313	250	503	257	308	526	833	417	859	755	410	551	370	121	395	456	759	353	156	169	242	414	454
Q	26	318	521	435	269	378	639	305	164	329	704	796	699	400	332	327	727	477	98	106	356	309	119	125	128	377
	27	204	261	74	47	43	34	32	30	38	45	51	67	171	277	300	216	393	183	67	78	117	84	70	133	126
	28	260	196	160	198	212	120	243	382	416	385	231	203	86	55	114	103	64	97	132	236	248	67	71	72	181
	29	241	415	525	388	292	161	87	120	147	223	246	184	287	230	230	198	181	366	411	442	283	380	614	253	288
D	30	350	442	204	290	298	465	412	358	279	277	115	254	152	103	249	340	292	202	192	94	300	361	502	327	286
	31	393	379	691	500	316	347	531	246	287	314	200	186	215	264	259	222	883	533	370	216	670	463	275	476	385
Mean		275	330	273	268	308	257	219	242	263	243	267	279	268	249	231	239	283	266	268	280	265	247	262	249	264
5Q Mean		106	124	70	72	111	108	91	63	64	76	80	103	112	147	160	148	193	122	125	96	97	92	106	130	108
5D Mean		490	667	549	576	674	438	444	507	531	413	483	386	356	425	311	185	391	402	464	439	371	239	249	377	432